Title

Diversity and functional specialization of oyster immune cells uncovered by integrative single cell level investigations

Authors

Sébastien de La Forest Divonne[1], Juliette Pouzadoux[1], Océane Romatif[1], Caroline Montagnani[1], Guillaume Mitta[2], Delphine Destoumieux-Garzon[1], Benjamin Gourbal[3], Guillaume M. Charrière[1#], Emmanuel Vignal[1#*]

Affiliations

[1] IHPE, Univ Montpellier, CNRS, Ifremer, Univ Perpignan Via Domitia, Montpellier, France

[2] Ifremer, IRD, Institut Louis-Malardé, Univ Polynésie française, UMR 241 SECOPOL, 98179 Taravao, Tahiti - Polynésie française, France

[3] IHPE, Univ Montpellier, CNRS, Ifremer, Univ Perpignan Via Domitia, Perpignan, France

EV and GC co-supervised the work.

[*] corresponding author: emmanuel.vignal@umontpellier.fr

Abstract

Mollusks are a major component of animal biodiversity and play a critical role in ecosystems and global food security. The Pacific oyster, *Crassostrea (Magallana) gigas*, is the most farmed bivalve mollusk in the world and is becoming a model species for invertebrate biology. Despite the extensive research on hemocytes, the immune cells of bivalves, their characterization remains elusive. Here we were able to extensively characterize the diverse hemocytes and identified at least seven functionally distinct cell types and three hematopoietic lineages. A combination of single-cell RNA sequencing, quantitative cytology, cell sorting, functional assays and pseudo-time analyses was used to deliver a comprehensive view of the

distinct hemocyte types. This integrative analysis enabled us to reconcile molecular and cellular data and identify distinct cell types performing specialized immune functions, such as phagocytosis, reactive oxygen species production, copper accumulation, and expression of antimicrobial peptides. This study emphasized the need for more in depth studies of cellular immunity in mollusks and non-model invertebrates and set the ground for further comparative immunology studies at the cellular level.

Introduction

Mollusca is the second largest invertebrate phylum, after Arthropoda, and the largest marine phylum, comprising approximately 23 % of all known marine organisms (*1*). Among them, bivalves exhibit a high diversity and a rich evolutionary history (*2*). The Pacific oyster *Crassostrea (Magallana) gigas* (*C. gigas* - Thunberg, 1793) (NCBI:txid29159) is a sessile filter-feeding bivalve that thrives in a variety of stressful environments ranging from intertidal to deep-sea conditions (*3*). It is a key species for the aquaculture industry worldwide (*4*). Several infectious diseases affect *C. gigas* at different life stages, which impacts its production. Given the significant socio-economic value of this species, there has been an increased focus on understanding and mitigating these diseases (*5*). The causes of these mortalities can involve a variety of pathogens, including viruses, bacteria and parasites that can be responsible for the mortality events affecting *C. gigas* (*6*). One of the most extensively researched infectious diseases is POMS (Pacific Oyster Mortality Syndrome), a polymicrobial disease responsible for mass mortalities of juvenile oysters (*7*). The disease is triggered by the OsHV-1 μVar herpesvirus, which alters the immune defenses of oysters, allowing the colonization of opportunistic bacteria, including *Vibrio*, that cause hemocyte lysis and bacteremia, ultimately leading to animal death (*7*). Other bacterial pathogens have also been identified as a contributing factor in mass mortalities of adult Pacific oysters in several countries. The most notable is *Vibrio aestuarianus* which affects adult oysters in Europe (*8*, *9*). To date, the majority of oyster pathogens or opportunistic pathogens that have been

55 characterized in detail have been found to subvert hemocyte defenses for their own benefit.
56 These include the OsHV-1 µVar herpesvirus (*10*) and virulent *Vibrio* strains of the species
57 *Vibrio crassostreae* and *Vibrio tasmaniensis* (*11*), *Vibrio aestuarianus* and *Vibrio harveyi* (*12*),
58 highlighting the critical role of hemocytes in oyster immunity. The development of immune-
59 based prophylactic treatments, such as immune-priming and immune-shaping, represents a
60 promising avenue for enhancing the natural defenses of oysters against pathogens and
61 increasing their survival rate. Nevertheless, the advancement of such therapies is still
62 constrained by a dearth of knowledge regarding the underlying molecular and cellular
63 mechanisms (*13*, *14*).
64 The study of hemocytes has a long history, dating back to the 1970s (for review see (*15*)).
65 Hemocytes are cellular effectors of the immune system. They engage in phagocytosis to
66 engulf and destroy potential pathogens, neutralizing parasites by encapsulation, or preventing
67 pathogen dissemination by cell aggregation and the release of extracellular DNA traps (*16*).
68 Furthermore, they engage in the humoral response by releasing cytokines, antimicrobial
69 peptides, and reactive oxygen species (ROS), which enable them to combat pathogens (*17*). In
70 addition to their role in oyster immunity, hemocytes have been implicated in numerous
71 physiological processes, including shell repair (*18*), wound healing, nutrient transport, and
72 environmental contaminant removal (*19*). Despite this acquired knowledge, hemocytes remain
73 an under-characterized population of circulating immune cells. The lack of a unified
74 classification and of molecular and functional genetic tools hinders our understanding of
75 lineage ontogeny and functional specialization. Several studies have proposed different
76 classifications of hemocytes in the *Ostreidae* family, with 3 to 4 hemocyte types reported (*15*).
77 These classifications are primarily based on either microscopic or flow cytometry analyses. In
78 *C. gigas*, three primary hemocyte cell types have been classically identified : blast,
79 hyalinocyte, and granulocyte cells. While the immune response of *C. gigas* has been
80 extensively studied using classical transcriptomics at the whole animal, tissue, or circulating
81 hemocyte levels, these approaches have failed to consider the diversity of hemocyte cell types

82 and lineages that underpin these responses (*20*). However, it is still imperative to accurately
83 describe the diversity of these cells, understand their ontogeny, and delineate cell lineages to
84 comprehend their specific roles. The advent of single-cell RNA sequencing (scRNA-seq)
85 techniques has enabled the monitoring of global gene expression at the single-cell level with
86 thousands of individual cells in a single experiment. This provides a unique opportunity to
87 overcome these limitations and deepen our understanding of hemocyte diversity and function
88 in bivalves. Recently scRNA-seq was used to provide a first molecular description of a
89 hemocyte population in the oyster *Crassostrea hongkongensis* (*21*). However, in the absence
90 of morphological and/or functional characterization studies, the authors could not deduce the
91 hemocyte cell types to be matched to the transcriptomic profiles generated by scRNA-seq.
92 While numerous transcriptomic analyses have been conducted on *C. gigas* hemocytes, none
93 have adopted a single-cell approach. In this study, we present an integrative analysis of the
94 diversity of *C. gigas* hemocytes at the single-cell level. To this end, we combined scRNA-seq
95 from a pathogen-free adult oyster combined with cytological, cell fractionation and functional
96 assays. This approach allowed us to create a comprehensive transcriptomic, cytological and
97 functional atlas of hemocyte cell types. Our scRNA-seq analyses identified 7 distinct
98 transcriptomic populations and functional annotation revealed distinct populations with
99 specific functions, including phagocytosis, oxidative burst, energetic metabolism, enhanced
100 transcription, translation and cell division. Quantitative cytology enabled the identification of
101 7 morphologically distinct hemocyte cell types, which allowed us to reconcile molecular and
102 cytological data. Density gradients were used to separate hemocyte cell types and qPCR or
103 functional assay analyses were performed to validate cell type-specific markers. By employing
104 this integrated approach, we could identify 1 type of hyalinocyte, 2 types of blasts and 4 types
105 of granular cells. Furthermore, we identified cell types that perform antimicrobial functions
106 through phagocytosis, ROS production, copper accumulation, and expression of antimicrobial
107 peptides. Finally, trajectory analysis of scRNA-seq data combined with functional analysis
108 revealed distinct differentiation pathways that may control hemocyte ontology and

109 differentiation processes. Based on these findings, we propose a more comprehensive and up-
110 to-date classification of *C. gigas* hemocytes, with a more accurate description of the different
111 cell types, their potential ontology and a precise description of their sub-functionalization.
112

113 **Results**

114 **Single-cell RNA sequencing reveals 7 distinct transcriptomic clusters of circulating**
115 **immune cells in oysters.**

116 Oysters are known to exhibit a high degree of individual genetic polymorphism, including
117 Copy Number Variation (CNV) and Presence Absence Variation (PAV) (*22*). To prevent
118 misinterpretation of the single-cell transcriptomic data, and to characterize the hemocyte cell
119 types and their heterogeneity, we sampled hemocytes from a unique pathogen-free animal
120 (Ifremer Standardized Animal, 18-month-old) and applied single-cell drop-seq technology to
121 3,000 single hemocytes **(Fig. 1A)**. The scRNA-seq library was generated and sequenced,
122 resulting in 127,959,215 high-quality filtered reads available for single-cell analysis (ENA
123 project accession number PRJEB74031). Primary bioinformatics analysis was performed
124 using the STAR solo aligner software (*23*) against the *C. gigas* genome (Genbank reference
125 GCA_902806645.1) from the Roslin Institute (*24*). Of the 127,959,215 reads, 97 % showed a
126 valid barcode and 89.2 % were successfully mapped to the genome with a saturation of 75.6
127 %. A total of 2,937 cells were profiled, yielding a median of 1,578 genes and 4,412 unique
128 molecular identifiers (UMIs) per cell among the 23,841 total genes detected, with a
129 sequencing saturation of 75.6 % **(Supp. Table 1)**. Secondary bioinformatic data processing
130 was conducted using the Seurat R package (version 4.3.0) (*25*). The data set was filtered to
131 remove data corresponding to empty droplets or cell doublets. Cells with a gene number
132 between 750 and 4,000 and less than 5 % mitochondrial genes were retained. After quality
133 control processing, 120 cells corresponding to empty droplets and cell doublets were removed,
134 and 2,817 cells were processed for data normalization. Finally, we performed linear
135 dimensional reduction and clustering on the 3,000 most variable genes from 2,817 cells

136 **(Supp. Fig. S1)**. Dimension reduction and clustering led to identifying 7 transcriptomic

137 clusters, within which hemocytes were distributed. These 7 different clusters represented 27.6,

138 23.1, 17.8, 16.9, 7, 4.6 and 3 % of the total cells **(Fig. 1B)**. For each transcriptomic cluster, a

139 pattern of over- and under-represented transcripts in each cell was identified **(Fig. 1C)**.

140 Average Log2FC values and percentage of expression in each cluster relative to all other

141 clusters were calculated for the ten most differentially expressed genes **(Fig. 1D and Table 1).**

142 Clear transcriptomic cell clusters were detected as well as specific gene markers for each

143 cluster **(Supp. Data 1)**. Only the transcriptomic signature of cluster 4 was less contrasting

144 than that of the other clusters **(Fig. 1D)**.

145

146 **A**

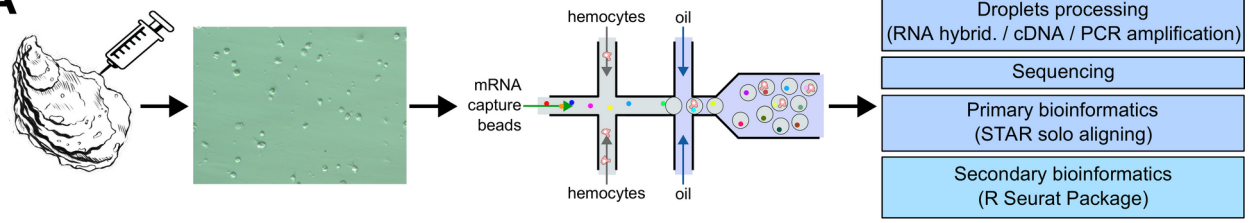

B

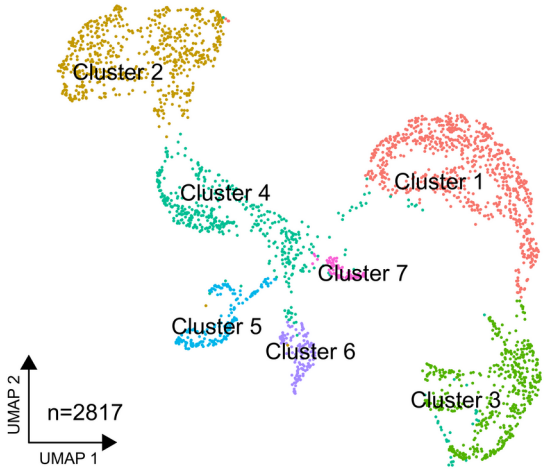

Number of cells	779	651	501	475	196	131	84
Percent of total	27.6	23.1	17.8	16.9	7	4.6	3
Number of DEGs	988	859	1027	953	1027	952	1319

C

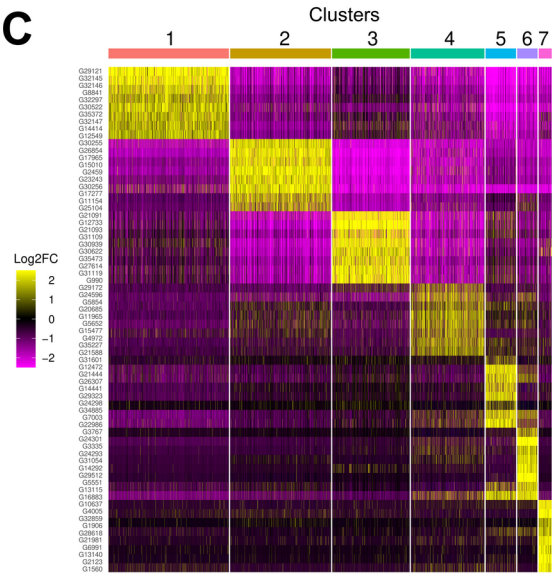

D

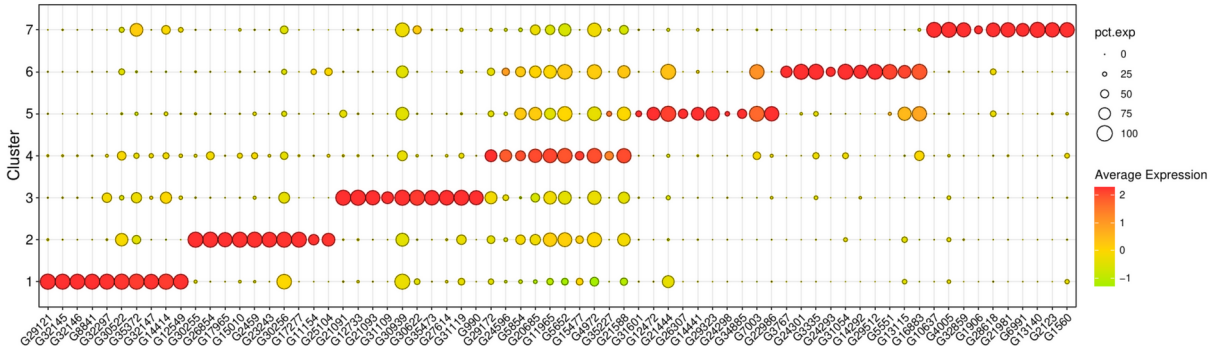

147 **Fig. 1. scRNA-seq analysis of C. gigas circulating hemocytes reveals 7 transcriptomic cell**

148 **clusters (A)** Schematic of the scRNA-seq 10X Genomics Chromium microfluidic technology

149 and bioinformatics processing workflow used. Dissociated hemocytes were collected from a

150 pathogen-free oyster and encapsulated in droplets for processing. After sequencing, the data

151 were processed bioinformatically. **(B)** Uniform Manifold Approximation and Projection

152 (UMAP) plot for dimensional reduction of the data set and summary of cells and the number

153 of Differentially Expressed Genes (DEGs) in each cluster. The table shows the characteristics

154 (number of cells, percentage of total cells and number of Differentially Expressed Genes in

155 each cluster) of the seven clusters identified. **(C)** Heatmap showing the top 10 overexpressed

156 genes in each cell per cluster as determined by FindAllMarkers() function in Seurat,

157 corresponding to clusters in UMAP plots from **Fig. 1B**, ranked by log2FC. **(D)** Dot plot

158 representing the ten most enriched DEGs per cluster based on average expression

159 (avg_log2FC). The color gradient of the dot represents the expression level, while the size

160 represents the percentage of cells expressing each gene per cluster.

161

Gene	log2FC	Pct 1	Pct 2	Description
				Cluster 1
G29121	4.31	1	0.099	L-galactono-gamma-lactone oxidase
G32145	4.18	0.992	0.079	Angiopoietin-1 receptor
G32146	3.90	0.985	0.063	Angiopoietin-1 receptor
G8841	3.13	0.988	0.049	C-type lectin domain-containing protein
G32297	2.88	0.99	0.232	PNPLA domain-containing protein
G30522	2.76	1	0.515	Cytochrome P450 2D28
G35372	2.69	1	0.483	60S ribosomal protein L26
G32147	2.45	0.969	0.131	Angiopoietin-1 receptor
G14414	2.45	1	0.343	DUF4773 domain-containing protein
G12549	2.38	0.974	0.132	Glutaredoxin domain-containing protein
				Cluster 2
G30255	5.31	1	0.15	Metalloproteinase inhibitor 3
G26854	4.24	1	0.16	Stanniocalcin
G17965	4.21	0.94	0.04	Complement C1q-like protein 2
G15010	3.99	0.99	0.17	Kyphoscoliosis peptidase
G2459	3.82	1	0.21	*Uncharacterized protein*
G23243	3.51	0.98	0.07	Fibronectin type-III domain-containing protein
G30256	3.23	1	0.69	NTR domain-containing protein
G17277	3.21	0.99	0.04	Putative modulator of levamisole receptor-1
G11154	3.16	0.68	0.05	Collagen alpha-1(XII) chain
G25104	3.1	0.84	0.08	C1q domain-containing protein
				Cluster 3
G21091	5.51	0.99	0.13	X-box binding protein-like protein
G12733	5.42	1	0.12	Galectin
G21093	5.17	0.94	0.05	IoIG
G31109	4.36	0.77	0.03	Cystatin domain-containing protein
G30939	4.25	1	0.86	Peptide ABC transporter permease
G30622	3.95	1	0.21	BHLH domain-containing protein
G35473	3.86	0.96	0.04	*Uncharacterized protein*
G27614	3.78	0.96	0.13	G Protein Receptor F1-2 domain-containing protein
G31119	3.77	0.99	0.42	Arrestin C domain-containing protein
G990	3.6	0.93	0.03	LITAF domain-containing protein
				Cluster 4
G29172	3.09	0.78	0.49	G Protein Receptor F1-2 domain-containing protein
G24596	2.37	0.78	0.25	High mobility group protein DSP1
G5854	1.8	0.64	0.38	N-acetyltransferase domain-containing protein
G20685	1.59	0.88	0.53	Ribosomal protein L22
G11965	1.57	0.92	0.7	Ribosome L4 associated C domain-containing protein
G5652	1.54	0.97	0.75	60S ribosomal protein L30
G15477	1.52	0.55	0.3	Metalloendopeptidase
G4972	1.49	0.96	0.8	60S ribosomal protein L12
G35227	1.46	0.55	0.06	ML domain-containing protein
G21588	1.42	0.94	0.69	60S ribosomal protein L13

Gene	log2FC	Pct 1	Pct 2	Description
				Cluster 5
G31601	5.24	0.38	0.06	Polyribonucleotide nucleotidyltransferase
G12472	3.99	0.85	0.03	Galectin
G21444	3.58	1	0.41	*Uncharacterized protein*
G26307	3.42	0.6	0.02	*Uncharacterized protein*
G14441	3.35	0.84	0.08	CUBN
G29323	3.21	0.9	0.01	GTPase IMAP family member 4
G24298	3.18	0.29	0.05	Putative Transmembrane protease serine 9
G34885	3.13	0.59	0.01	Gliding motility-associated C-terminal domain-containing protein
G7003	2.55	0.99	0.16	ETS-related transcription factor Elf-4
G22986	2.37	0.94	0.1	Metalloendopeptidase
				Cluster 6
G3767	6.45	0.74	0.02	Natterin-1
G24301	6.16	0.99	0.02	Aspartate-semialdehyde dehydrogenase
G3335	5.19	1	0.16	*ncRNA*
G24293	4.57	0.59	0.01	*Uncharacterized protein*
G31054	3.56	1	0.13	GATA-binding factor 3
G14292	3.29	0.87	0.03	Membrane-associated guanylate kinase inverted 3
G29512	3.2	0.99	0	Caveolin
G5551	2.93	0.97	0.02	Neuronal acetylcholine receptor subunit alpha-6
G13115	2.73	0.83	0.26	*ncRNA*
G16883	2.62	1	0.2	Allograft inflammatory factor
				Cluster 7
G10637	4.21	0.99	0.03	BZIP domain-containing protein
G4005	4.07	0.99	0.21	Ras-related protein Rab-20
G32859	3.9	0.93	0.04	G Protein Receptor F1-2 domain-containing protein
G1906	3.82	0.5	0.02	Glutathione peroxidase
G28618	3.53	0.91	0.09	Sporozoite and liver stage asparagine-rich protein
G21981	3.5	0.94	0.05	*ncRNA*
G6991	3.4	0.85	0.01	Rho-GAP domain-containing protein
G13140	3.12	1	0.03	DBH-like monooxygenase protein 1
G2123	3.05	0.94	0.02	SPRY domain-containing SOCS box protein 3
G1560	3.02	0.95	0.17	Glutathione peroxidase

163 **Table 1. Top 10 overexpressed genes identified in each transcriptomic cluster.** The first
164 column indicates the gene number according to the annotation. 'log2FC' represents the log2
165 fold change of the gene in the cluster compared to all other cells. 'Pct1' is the percentage of
166 cells expressing the gene in the cluster and 'Pct2' is the fraction of cells expressing the gene in
167 all other clusters. The description is the annotation of the expressed gene.
168

169 **KEGG pathways and GO-terms analyses reveal functional diversity in *C. gigas***
170 **hemocytes.**
171

172 The ScRNA-seq data demonstrated that specific functions are carried out by the hemocyte cell
173 types that comprise the seven transcriptomic clusters. A preliminary overview of the functions
174 over-represented in each cluster was obtained through a KEGG pathway analysis on the
175 overrepresented transcripts (Log2FC > 0.25) using the *C. gigas* annotation provided by the
176 DAVID consortium (*26*), thereby identifying pathways specifically enriched in each cluster.
177 Cluster 1 demonstrated enrichment in viral processing and endocytosis **(Figure 2A and**
178 **Supplemental Table S2)**. Additionally, it demonstrated enrichment in pyruvate metabolism,
179 glycolysis/gluconeogenesis and the pentose phosphate pathways. Clusters 1 and 3 exhibited a
180 distinctive enrichment in carbohydrate metabolism and endocytosis. In particular, cluster 3
181 exhibited enriched transcripts associated with glycolysis/gluconeogenesis and TCA cycle
182 activities. Cluster 4 was enriched in protein synthesis, including transcription (spliceosome,
183 ribosome, nucleocytoplasmic transport and mRNA surveillance pathway) folding, sorting and
184 degradation of protein pathways. Clusters 2, 5 and 6 exhibited a shared signature of
185 enrichment in ribosome-related genes. Cluster 2 demonstrated a specific enrichment in motor
186 protein-coding genes responsible for cell motility and xenobiotic metabolism. Remarkably,
187 clusters 1, 3, 4 and 5 exhibited enriched oxidative phosphorylation transcripts, whereas the
188 transcripts of cluster 7 were enriched in vesicular trafficking and endo-lysosomal pathways
189 (endocytosis, endosome, phagosome, lysosome, auto and mitophagy).

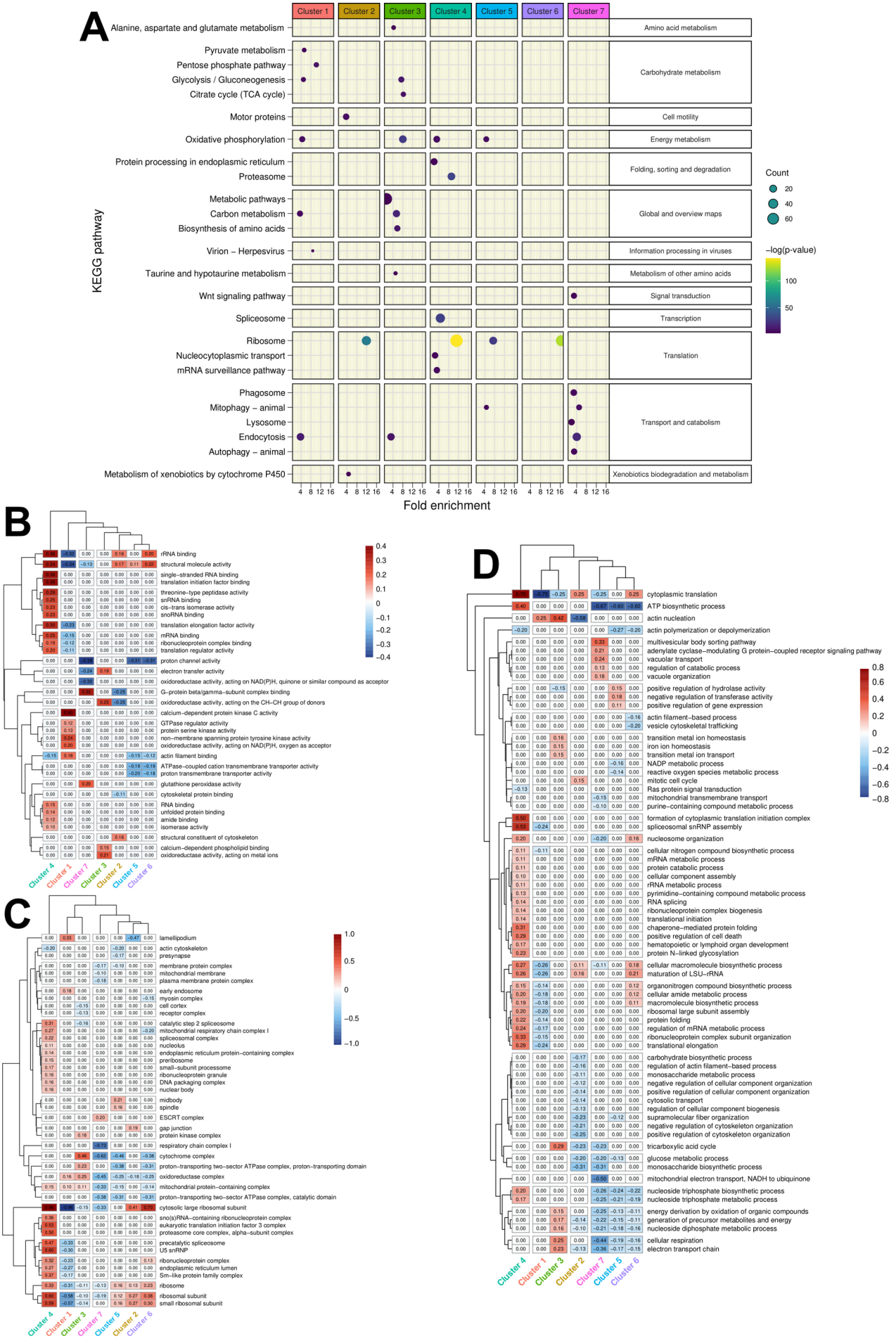
A
Cluster 1
Cluster 2
Cluster 3
Cluster 4
Cluster 5
Cluster 6
Cluster 7
KEGG pathway
Alanine, aspartate and glutamate metabolism
Pyruvate metabolism
Pentose phosphate pathway
Glycolysis / Gluconeogenesis
Citrate cycle (TCA cycle)
Motor proteins
Oxidative phosphorylation
Protein processing in endoplasmic reticulum
Proteasome
Metabolic pathways
Carbon metabolism
Biosynthesis of amino acids
Virion – Herpesvirus
Taurine and hypotaurine metabolism
Wnt signaling pathway
Spliceosome
Ribosome
Nucleocytoplasmic transport
mRNA surveillance pathway
Phagosome
Mitophagy – animal
Lysosome
Endocytosis
Autophagy – animal
Metabolism of xenobiotics by cytochrome P450
Amino acid metabolism
Carbohydrate metabolism
Cell motility
Energy metabolism
Folding, sorting and degradation
Global and overview maps
Information processing in viruses
Metabolism of other amino acids
Signal transduction
Transcription
Translation
Transport and catabolism
Xenobiotics biodegradation and metabolism
4 8 12 16
Fold enrichment
Count
20
40
60
−log(p-value)
100
50
B
rRNA binding
structural molecule activity
single−stranded RNA binding
translation initiation factor binding
threonine−type peptidase activity
snRNA binding
cis−trans isomerase activity
snoRNA binding
translation elongation factor activity
mRNA binding
ribonucleoprotein complex binding
translation regulator activity
proton channel activity
electron transfer activity
oxidoreductase activity, acting on NAD(P)H, quinone or similar compound as acceptor
G−protein beta/gamma−subunit complex binding
oxidoreductase activity, acting on the CH−CH group of donors
calcium−dependent protein kinase C activity
GTPase regulator activity
protein serine kinase activity
non−membrane spanning protein tyrosine kinase activity
oxidoreductase activity, acting on NAD(P)H, oxygen as acceptor
actin filament binding
ATPase−coupled cation transmembrane transporter activity
proton transmembrane transporter activity
glutathione peroxidase activity
cytoskeletal protein binding
RNA binding
unfolded protein binding
amide binding
isomerase activity
structural constituent of cytoskeleton
calcium−dependent phospholipid binding
oxidoreductase activity, acting on metal ions
Cluster 4
Cluster 1
Cluster 7
Cluster 3
Cluster 2
Cluster 5
Cluster 6
C
lamellipodium
actin cytoskeleton
presynapse
membrane protein complex
mitochondrial membrane
plasma membrane protein complex
early endosome
myosin complex
cell cortex
receptor complex
catalytic step 2 spliceosome
mitochondrial respiratory chain complex I
spliceosomal complex
nucleolus
endoplasmic reticulum protein−containing complex
preribosome
small−subunit processome
ribonucleoprotein granule
DNA packaging complex
nuclear body
midbody
spindle
ESCRT complex
gap junction
protein kinase complex
respiratory chain complex I
cytochrome complex
proton−transporting two−sector ATPase complex, proton−transporting domain
oxidoreductase complex
mitochondrial protein−containing complex
proton−transporting two−sector ATPase complex, catalytic domain
cytosolic large ribosomal subunit
sno(s)RNA−containing ribonucleoprotein complex
eukaryotic translation initiation factor 3 complex
proteasome core complex, alpha−subunit complex
precatalytic spliceosome
U5 snRNP
ribonucleoprotein complex
endoplasmic reticulum lumen
Sm−like protein family complex
ribosome
ribosomal subunit
small ribosomal subunit
Cluster 4
Cluster 1
Cluster 3
Cluster 7
Cluster 5
Cluster 2
Cluster 6
D
cytoplasmic translation
ATP biosynthetic process
actin nucleation
actin polymerization or depolymerization
multivesicular body sorting pathway
adenylate cyclase−modulating G protein−coupled receptor signaling pathway
vacuolar transport
regulation of catabolic process
vacuole organization
positive regulation of hydrolase activity
negative regulation of transferase activity
positive regulation of gene expression
actin filament−based process
vesicle cytoskeletal trafficking
transition metal ion homeostasis
iron ion homeostasis
transition metal ion transport
NADP metabolic process
reactive oxygen species metabolic process
mitotic cell cycle
Ras protein signal transduction
mitochondrial transmembrane transport
purine−containing compound metabolic process
formation of cytoplasmic translation initiation complex
spliceosomal snRNP assembly
nucleosome organization
cellular nitrogen compound biosynthetic process
mRNA metabolic process
protein catabolic process
cellular component assembly
rRNA metabolic process
pyrimidine−containing compound metabolic process
RNA splicing
ribonucleoprotein complex biogenesis
translational initiation
chaperone−mediated protein folding
positive regulation of cell death
hematopoietic or lymphoid organ development
protein N−linked glycosylation
cellular macromolecule biosynthetic process
maturation of LSU−rRNA
organonitrogen compound biosynthetic process
cellular amide metabolic process
macromolecule biosynthetic process
ribosomal large subunit assembly
protein folding
regulation of mRNA metabolic process
ribonucleoprotein complex subunit organization
translational elongation
carbohydrate biosynthetic process
regulation of actin filament−based process
monosaccharide metabolic process
negative regulation of cellular component organization
positive regulation of cellular component organization
cytosolic transport
regulation of cellular component biogenesis
supramolecular fiber organization
negative regulation of cytoskeleton organization
positive regulation of cytoskeleton organization
tricarboxylic acid cycle
glucose metabolic process
monosaccharide biosynthetic process
mitochondrial electron transport, NADH to ubiquinone
nucleoside triphosphate biosynthetic process
nucleoside triphosphate metabolic process
energy derivation by oxidation of organic compounds
generation of precursor metabolites and energy
nucleoside diphosphate metabolic process
cellular respiration
electron transport chain
Cluster 4
Cluster 1
Cluster 3
Cluster 2
Cluster 7
Cluster 5
Cluster 6

191 **Fig. 2. KEGG and Gene Ontology analysis of the gene signature in each cluster. (A)** A
192 synthetic representation of the KEGG pathway analysis is shown. Colored columns represent
193 the 7 transcriptomic clusters. Each row is a KEGG pathway, the colored dot represents the -
194 log(p-value) and the dot size represents the number (count) of enriched genes in each pathway
195 category. The fold enrichment is shown on the x-axis. Panels **(B)**, **(C)** and **(D)** show the results
196 of Gene Ontology terms (GO-terms) for Biological Processes (BP), Cellular Components
197 (CC) and Molecular Functions (MF) respectively, obtained with the overexpressed genes of
198 each cluster (Absolute value Log2FC > 0.25 and significant p-value < 0.001) using RBGOA
199 analysis (p-value <= 0.001) for three different ontology universes. Each panel corresponds to
200 one ontology universe, and the analysis highlights over- and under-enriched terms. The
201 number in the heatmap and the scale indicate the proportion of significant positive GO-terms.
202 Positive values indicate over-enrichment and negative values indicate under-enrichment of the
203 respective BP, CC and MF ontologies.
204
205 For a more detailed functional characterization of each transcriptomic cluster, we performed a
206 re-annotation of the *C. gigas* genome using a combination of tools to enhance the GO term
207 richness of the existing annotation prior to functional GO term analysis. To this end, we used
208 the *C. gigas* genome (Genbank reference GCA_902806645.1) and the associated gff3
209 annotation file from the Roslin Institute (*24*). These files were used to extract and process the
210 longest CDSs for GO-term annotation using the Orson pipeline (see Materials and Methods).
211 Of the 30,724 extracted CDSs, 22,462 were annotated (GO-terms and sequence description),
212 yielding an annotation percentage of 73.1 %. Of the 30,724 CDSs, 22,391 were annotated with
213 Molecular Functions (MF), Biological Processes (BP), and Cellular Components (CC) GO-
214 terms (**Supp. Fig. S2 and Supp. Data 2**). Using the GO-term annotation and the Log2FC of
215 genes calculated after scRNA-seq processing in each cluster, GO enrichment analysis was
216 performed by rank-based gene ontology analysis (RBGOA) (*27*). RBGOA analysis was

217 performed on the GO-terms identified in each cluster (**Supp. Data 3**). The results are
218 presented in **Figures 2B, C and D**.
219
220 The scRNA-seq-based analysis identified seven distinct transcriptomic profiles for each cell
221 cluster, thereby shedding light on greater heterogeneity and functional diversity of *C. gigas*
222 hemocytes than previously described. Cluster 1, comprising 27.6 % of cells, is characterized
223 by its morphology and capacity to remodel actin cytoskeleton, as well as oxidoreductase
224 activity. This is evidenced by an enrichment in oxidoreductase activity acting on NAD(P)H
225 and kinase activities BP, actin nucleation MF and lamellipodium and early endosomes CC.
226 Cluster 2, comprising 23.1 % of cells, has an increased translation activity, as indicated by
227 enrichment in BP, MF and CC terms related to rRNA binding, cytoplasmic translation,
228 maturation of LSU-rRNA, and ribosomes respectively. Cluster 3, representing 17.8 % of cells,
229 shows enrichment in cellular oxidation and actin nucleation, as evidenced by an enrichment in
230 BP and MF related to oxidoreductase activities acting on metal ions, electron transfer, cellular
231 oxidation and actin nucleation, and CC related to cytochromes, oxidoreductase complex, and
232 mitochondrial protein-containing complexes. Cluster 4, representing 16.9 % of cells, has
233 transcriptomic signatures reminiscent of spliceosome assembly, rRNA maturation, and ATP
234 biosynthesis (BP related to RNA binding, translation, and proteasome, MF related to
235 spliceosome assembly, rRNA maturation, and ATP biosynthesis, and CC related to nuclear
236 bodies and ribosomes). Cluster 5, comprising 7 % of cells, demonstrates enrichment in
237 structural molecule activity, hydrolase regulation, and gene expression, as evidenced by its
238 BP, MF, and CC related to ribosome, midbody, and spindle localization. Cluster 6, comprising
239 4.6 % of cells, is characterized by a specific nucleosome organization, translation, and
240 biosynthetic processes, with related BP, MF, and CC tied to ribosomes, ribonucleoprotein
241 complex and rRNA binding. Cluster 7, representing a mere 3 % of cells, is characterized by
242 multivesicular body sorting, vacuolar transport, vacuole organization, and G protein-coupled
243 receptor signaling, with related BP, MF, and CC of the ESCRT machinery.

244 **Seven morphologically distinct immune cell types are identified by quantitative cytology**
245 **and transcriptomic markers.**

246 Cytological studies were conducted using MCDH staining to better characterize the diversity
247 of circulating hemocytes in *C. gigas*. Seven distinct hemocyte morphotypes were identified: 3
248 non-granular (acidophilic blasts, basophilic blasts and hyalinocytes) and 4 granular (small
249 granule cells, big granule cells, vesicular cells and macrophage-like) **(Fig. 3 and Supp. Fig.**
250 **S3)**. Hyalinocytes (30 % of total hemocytes) are large cells with an irregular spreading
251 membrane. They contain an azurophilic cytoplasm without granulations and their irregular
252 nucleus varies in size (**Fig. 3A panel H**). Macrophage-like cells (19 % of the hemocytes)
253 present an irregular membrane punctuated by rare pseudopodia with a polylobed nucleus and a
254 basophilic cytoplasm where polychromatic inclusions of various sizes could be observed (**Fig**
255 **3A. panel ML**). Basophilic blasts characterized by a basophil cytoplasm (**Fig. 3A panel BBL**)
256 and acidophilic blasts with acidophil cytoplasm (**Fig. 3A panel ABL**) accounted for 18 % and
257 15 %, respectively, of the total hemocytes. They are rounded cells without granulation, with a
258 uniform and regular dense nucleus and a high nucleo-cytoplasmic ratio. Small granule cells
259 (12 % of total hemocytes) have an irregular membrane punctuated by rare pseudopodia, an
260 acidophilic cytoplasm, and numerous homogeneous purple granules (**Fig. 3A panel SGC**).
261 Big granule cells (4 % of total hemocytes) are rounded cells with a basophilic cytoplasm
262 containing large, slightly dark purple to black vesicles of heterogeneous size (**Fig. 3A panel**
263 **BGC**). Vesicular cells (2 % of total hemocytes) are rounded cells with acidophilic cytoplasm,
264 rich in homogeneous transparent and fluorescent to UV light vesicles with an irregular nucleus
265 (**Fig. 3A panel VC**). Only blasts (BBL, ABL) have a nucleo-cytoplasmic ratio less than 1,
266 whereas the other hemocytes described have a nucleo-cytoplasmic ratio greater than 1.
267 To gain further insight into the functional characterization of these diverse hemocyte
268 morphotypes and to associate them with the transcriptomic clusters identified in the scRNA-
269 seq, we enhanced an existing hemocyte fractionation approach using an isopycnic Percoll
270 density gradient to sort the hemocytes (*28*). Cell sorting was performed using a discontinuous

Percoll gradient with densities ranging from 1.0647 to 1.1049. Seven distinct density fractions were established (**Fig. 3B**) and the hemocyte composition was then characterized by cytological analysis of each fraction (**Fig. 3A;** see also **Supp. Fig. S4** for statistical significance). The uneven distribution of hemocyte morphotypes along the density gradient enabled a relative separation of the different cell populations (**Supp. Fig S4**). In summary, hyalinocytes were significantly enriched in the first fraction, while macrophage-like cells were significantly enriched in fraction 3 and fraction 4. Acidophilic blasts were significantly enriched in fraction 2. Basophilic blasts were significantly enriched in fractions 2 and 3. Vesicular cells were enriched in fraction 5, big granule cells were enriched in fraction 4 and small granule cells in fractions 6 and 7 (**Fig. 3C and Supp. Fig. S4**).

A

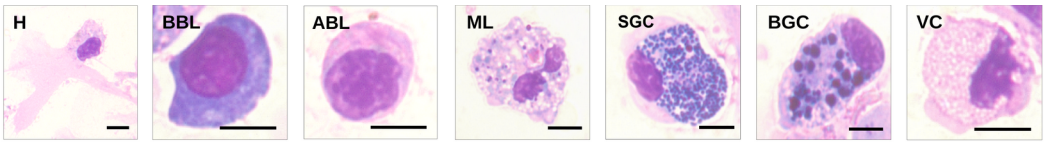

Cell types	Hyalinocyte (H)	Basophilic Blast-Like (BBL)	Acidophilic Blast-Like (ABL)	Macrophage Like (ML)	Small Granule Cell (SGC)	Big Granule Cell (BGC)	Vesicular Cell (VC)
Pourcentage[a]	29.6 ± 8.74%	17.7 ± 6.34 %	15.4 ± 5.38 %	18.6 ± 7.09 %	12.3 ± 5.50 %	4.10 ± 2.53 %	2.32 ± 1.47 %
Cell Size (µm)	21-31	7-11	6-8	12-17	14-25	10-15	8-13
Nucleus Size (µm)	6-8	4-7	4-5	4-6	5-7	4-6	4-6
Cytoplasm	Acidophilic	Basophilic	Acidophilic	Acidophilic	Acidophilic	Basophilic	Acidophilic
Pseudopods	Long	Unobvious	Unobvious	Rare	Rare	Unobvious	Unobvious
C/N[b] ratio	C/N>>1	C/N<1	C/N<1	C/N>>1	C/N>>1	C/N>1	C/N>1
Granules	-	-	-	Mixed	Basophilic	Basophilic	Transparent
			Size	*0.3-1 µm*	*0.3 µm*	*1 µm*	*0.3 µm*
			Shape	*Round*	*Round*	*Epsiloid*	*Round*
			Particularities	-	-	*Brown*	*Fluo. at 240nm*

[a] – Pourcentage of the cell type in total hemolymphe
[b] – Cytoplasm / Nucleus surface ratio

B

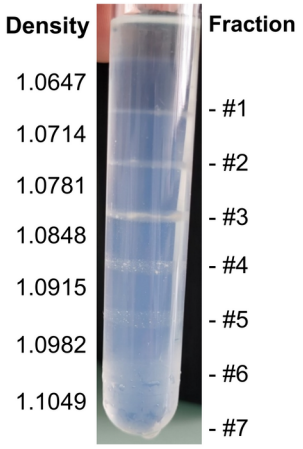

C

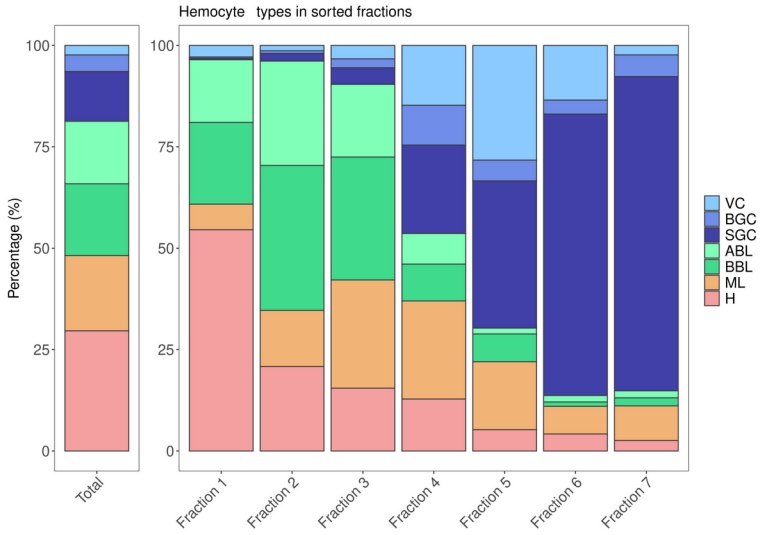

Fig 3. *C. gigas* naive hemocyte formula and Percoll gradient hemolymph fractionation

(A) Morphology, percentages and characteristics of the 7 cell types identified by MCDH staining. **H** : Hyalinocyte, **ML** : Macrophage Like, **BBL** : Basophilic Blast Like cell, **ABL** :

285 Acidophilic Blast Like cell, **SGC** : Small Granule Cell, **BGC** : Big Granule Cell, **VC** :
286 Vesicular Cell. Scale bar : 5 µm. Hyalinocytes (54 %) and blast cells (ABL & BBL) (35 %)
287 were predominant in the first fraction. The second fraction showed an increase in blasts (ABL
288 26 %, BBL 36 %) and a decrease in hyalinocytes (21 %). Fraction 3 had a mixed content with
289 a decrease in hyalinocytes and blasts (15 %), and a majority of blasts and macrophage-like
290 cells. Fraction 4 had an increase in granular cells (SGC 22 %, BGC 10 %, VC 15 %) and a
291 decrease in blasts (ABL 8 %, BBL 9 %). Fraction 5 showed an increase in small granule cells
292 (36 %) and vesicular cells (28 %), and a decrease in big granule cells (5%). Fraction 6 had
293 fewer hyalinocytes, macrophage-like cells, and blast cells compared to small granule cells and
294 vesicular cells. The last fraction consisted mainly of small granule cells (81 %). **(B)** Sorting of
295 hemocytes on a discontinuous Percoll gradient. 7 fractions were identified along the gradient
296 at the top of each density cushion (from d=1.0647 at #1 to d= 1.1049 at #7). **(C)**
297 Representation of the average values (from 5 different fractionation experiments) of the
298 different hemocyte types in the seven percoll gradient fractions compared to the average
299 hemolymph composition of a naive oyster (Total). **VC** : Vesicular Cells, **BGC** : Big Granule
300 Cells, **SGC** : Small Granule Cells, **ABL** : Acidophilic Blast Like cells, **BBL** : Basophilic Blast
301 Like cells, **ML** : Macrophage Like cells and **H** : Hyalinocytes respectively. (**Supp. Fig. S4** for
302 statistics).

303 To identify the transcriptomic cell clusters corresponding to the different hemocyte
304 morphotypes, we used RT-qPCR to detect the expression of different cluster-specific marker
305 genes in the different hemocytes in the Percoll density fractions. The marker genes were
306 selected without any a priori assumptions based solely on their expression levels (Log2FC)
307 and their percentage of expression (Pct1 / Pct2 ratio) in the cluster of interest relative to all
308 other cell clusters (**Table 2).** The expression level of each marker in the seven different
309 clusters confirmed that the 14 selected marker genes were differentially expressed in each
310 scRNA-seq transcriptomic cluster (**Supp. Fig. S5**).

Gene Number	Avg. Log2FC	Pct.1/Pct.2 Ratio	Cluster	Description	Marker Name
G8994	2.05	38.20	1	Laccase-24	LACC24
G8841	3.13	20.16		C-type lectin domain-containing protein	CLEC
G24846	2.31	31.52	2	EGF-like domain-containing protein 8	EGFL
G17277	3.21	23.00		Putative modulator of levamisole receptor-1	LEVAR
G22387	3.16	16.76	3	TGc domain-containing protein	TGC
G21091	5.51	7.69		X-box binding protein-like protein	XBOX
G35227	1.46	9.98	4	ML domain-containing protein	MLDP
G31074	0.94	6.51		High mobility group protein B1	HMGB1
G14441	3.35	11.01	5	Cubilin	CUBN
G12472	3.99	24.91		Galectin	GAL
G29512	3.20	246.25	6	Caveolin	CAV
G3767	6.45	41.11		Natterin-1	NAT1
G13140	3.12	40.00	7	DBH-like monooxygenase protein 1	MOX
G32859	3.90	23.82		G protein receptor F1-2 domain-containing protein	GPROT

312 **Table 2. Table of the 14 marker genes specific to the different transcriptomic clusters.**
313 Gene number, average Log2FC, pct1/pct2 ratio (percentage of cells expressing this transcript
314 in the cluster divided by the percentage of all other cells expressing this transcript) and cluster
315 number are reported. The description is taken from our annotation and the marker name is
316 derived from the description.

317 RT-qPCR expression profiles in the hemocyte fractions obtained from the Percoll density
318 gradient revealed distinct patterns according to the different transcriptomic cluster marker
319 genes (**Fig. 4A**). Cluster 1 markers (LACC24 and CLEC) were overexpressed in fractions 1, 2,
320 3 and underexpressed in the remaining fractions relative to total hemocytes. Cluster 2 markers
321 (EGFL and LEVAR) showed a decreasing pattern of expression from fraction 1 to fraction 7.
322 Cluster 3 markers (TGC and XBOX) showed a significant increase in expression in fractions 4
323 to 7. Cluster 4 markers (MLDP and HMGB1) showed a gradually decreasing expression
324 pattern from fraction 2 to fraction 7. Cluster 5 marker genes (GAL and CUBN) were
325 underexpressed in fractions 4 to 7, but not differentially expressed in fractions 1 to 3
326 compared to total hemocytes. Cluster 6 marker genes (CAV and NAT1) were overexpressed
327 in fraction 3, expressed similarly to total hemocytes in fraction 2, and underexpressed in
328 fractions 1, and 4 to 7. Finally, cluster 7 marker genes (MOX and GPROT) were
329 overexpressed only in fractions 3 to 7. Correlation analysis and statistical validation

330 demonstrated a clear association between hemocyte morphotypes and 14 gene markers (**Fig.**
331 **4B, Fig. 4C and Supp. Table S4**). Cluster 3 marker genes (TGC and XBOX) correlated
332 positively (r = 0.74 & 0.75) and specifically with small granule cells (SGC). Cluster 7 markers
333 (MOX and GPROT) correlated (r = 0.68 and r = 0.56) with vesicular cells (VC). Cluster 2
334 markers (EGFL and LEVAR) correlated positively with hyalinocytes (H) (r=0.85 and r=0.81).
335 No specific markers could be identified for blasts and macrophage-like cells.

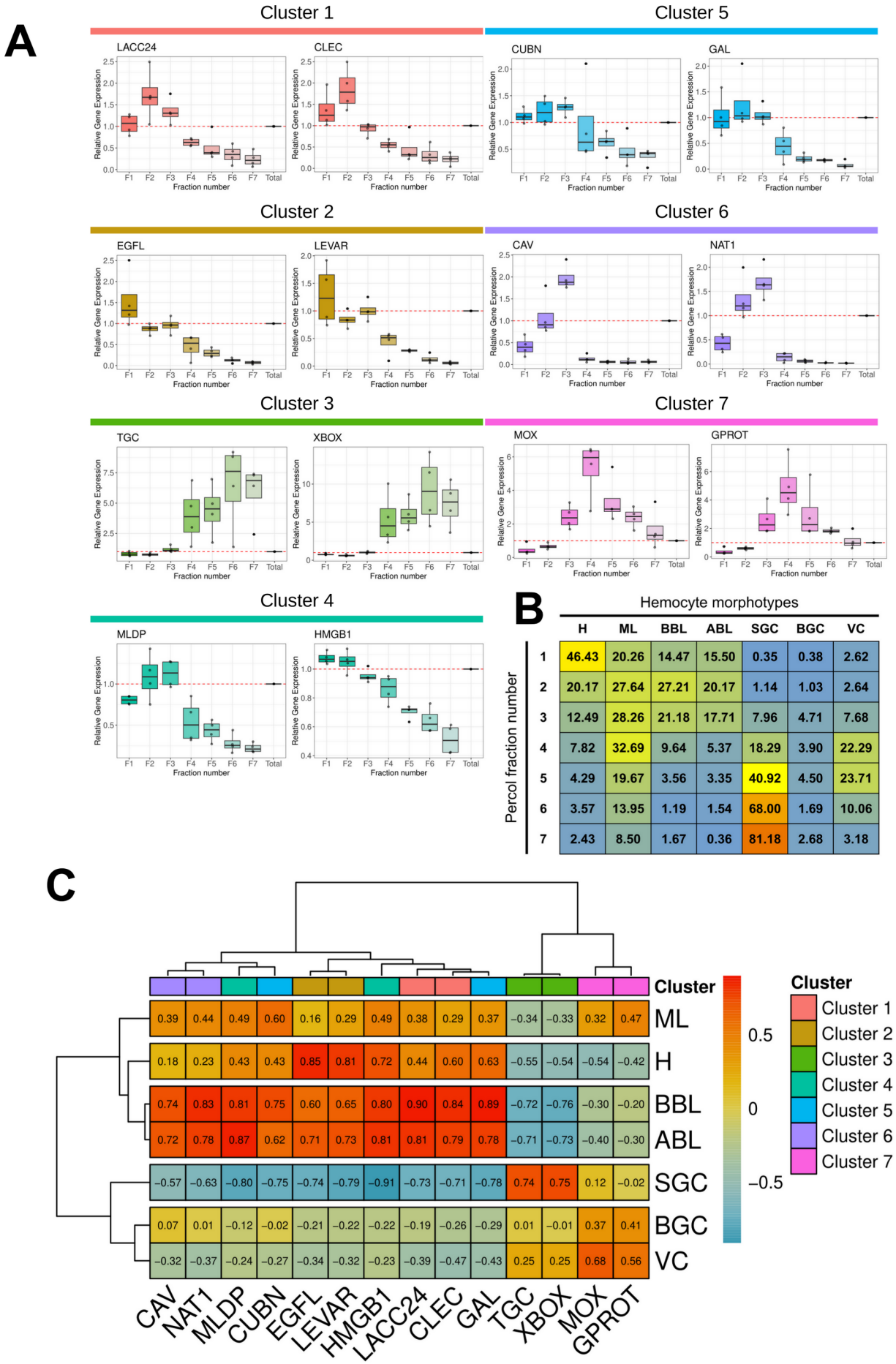

Percol fraction number	H	ML	BBL	ABL	SGC	BGC	VC
1	46.43	20.26	14.47	15.50	0.35	0.38	2.62
2	20.17	27.64	27.21	20.17	1.14	1.03	2.64
3	12.49	28.26	21.18	17.71	7.96	4.71	7.68
4	7.82	32.69	9.64	5.37	18.29	3.90	22.29
5	4.29	19.67	3.56	3.35	40.92	4.50	23.71
6	3.57	13.95	1.19	1.54	68.00	1.69	10.06
7	2.43	8.50	1.67	0.36	81.18	2.68	3.18

	CAV	NAT1	MLDP	CUBN	EGFL	LEVAR	HMGB1	LACC24	CLEC	GAL	TGC	XBOX	MOX	GPROT
ML	0.39	0.44	0.49	0.60	0.16	0.29	0.49	0.38	0.29	0.37	−0.34	−0.33	0.32	0.47
H	0.18	0.23	0.43	0.43	0.85	0.81	0.72	0.44	0.60	0.63	−0.55	−0.54	−0.54	−0.42
BBL	0.74	0.83	0.81	0.75	0.60	0.65	0.80	0.90	0.84	0.89	−0.72	−0.76	−0.30	−0.20
ABL	0.72	0.78	0.87	0.62	0.71	0.73	0.81	0.81	0.79	0.78	−0.71	−0.73	−0.40	−0.30
SGC	−0.57	−0.63	−0.80	−0.75	−0.74	−0.79	−0.91	−0.73	−0.71	−0.78	0.74	0.75	0.12	−0.02
BGC	0.07	0.01	−0.12	−0.02	−0.21	−0.22	−0.22	−0.19	−0.26	−0.29	0.01	−0.01	0.37	0.41
VC	−0.32	−0.37	−0.24	−0.27	−0.34	−0.32	−0.23	−0.39	−0.47	−0.43	0.25	0.25	0.68	0.56

Fig 4. Characterization of molecular markers specific to the different hemocyte morphotypes. (A) Relative expression level of the 14 markers in the various fractions after

339 gradient density sorting. The graphs show the relative expression of genes compared to their
340 expression in total hemocytes in the various fractions (red dotted line). Standard deviations
341 were calculated based on four independent experiments. **(B)** Average percentage of each
342 hemocyte type in the 7 Percoll gradient fractions used to quantify marker gene expression by
343 qPCR. **(C)** Correlation matrix between the relative gene expression of each marker gene in
344 each fraction and the percentage of each hemocyte type in the same fractions. Values and
345 color scale represent the Pearson correlation coefficient (r) ranging from -1 (inverse
346 correlation) to +1 (full correlation). **H** : Hyalinocyte, **ML** : Macrophage Like, **BBL** :
347 Basophilic Blast Like cell, **ABL** : Acidophilic Blast Like cell, **SGC** : Small Granule Cell,
348 **BGC** : Big Granule Cell, **VC** : Vesicular Cell. **LACC24** : Laccase 24, **CLEC** : C-type lectin
349 domain-containing protein, **EGFL** : EGF-like domain-containing protein 8, **LEVAR** :
350 Putative regulator of levamisole receptor-1, **TGC** : TGc domain-containing protein, **XBOX** :
351 X-box binding protein-like protein, **MLDP** : ML domain containing protein, **HMGB1** : High
352 mobility group protein B1, **CUBN** : Cubilin, **GAL** : Galectin, **CAV** : Caveolin, **NAT1** :
353 Natterin-1, **MOX** : DBH-like monooxygenase protein 1, **GPROT** : G protein receptor F1-2
354 domain-containing protein.

355 By employing RT-qPCR, cell sorting on Percoll gradients, and scRNA-seq analysis, we could
356 identify cell types corresponding to three transcriptomic clusters. Cluster 3 corresponds to
357 small granule cells (SGC), cluster 2 to hyalinocytes (H), and cluster 7 to vesicular cells (VC).
358 Cluster 3, cluster 2 and cluster 7 represent 17.8 %, 23 % and 3 % of the total cells analyzed by
359 scRNA-seq, respectively. This is consistent with cytological data, which indicated the
360 presence of 12.5 % +/- 5 % Small Granule Cells, 30 % +/- 9.3 % Hyalinocytes and 2.3 % +/-
361 1.6 % Vesicular Cells (**Fig. 1B and Fig. 3A**). Furthermore, the molecular and cellular
362 functions derived from GO-term and KEGG analyses (**Fig. 2**) were in alignment with the
363 anticipated functions for these three cell types.

364 **Only macrophage-like and small granule cells behave as professional phagocytes.**

365 The hemocytes separated on the Percoll gradient were characterized functionally to gain
366 further insight into their functional specialization. Two hemocyte functions, namely
367 phagocytosis and production of Reactive Oxygen Species (ROS), are known to carry out
368 major cellular antimicrobial activities. Granular cells have been suggested to be the
369 professional phagocytes specialized for these functions (*29*). Phagocytosis and oxidative burst
370 were studied using cell response toward zymosan particles (*30*).

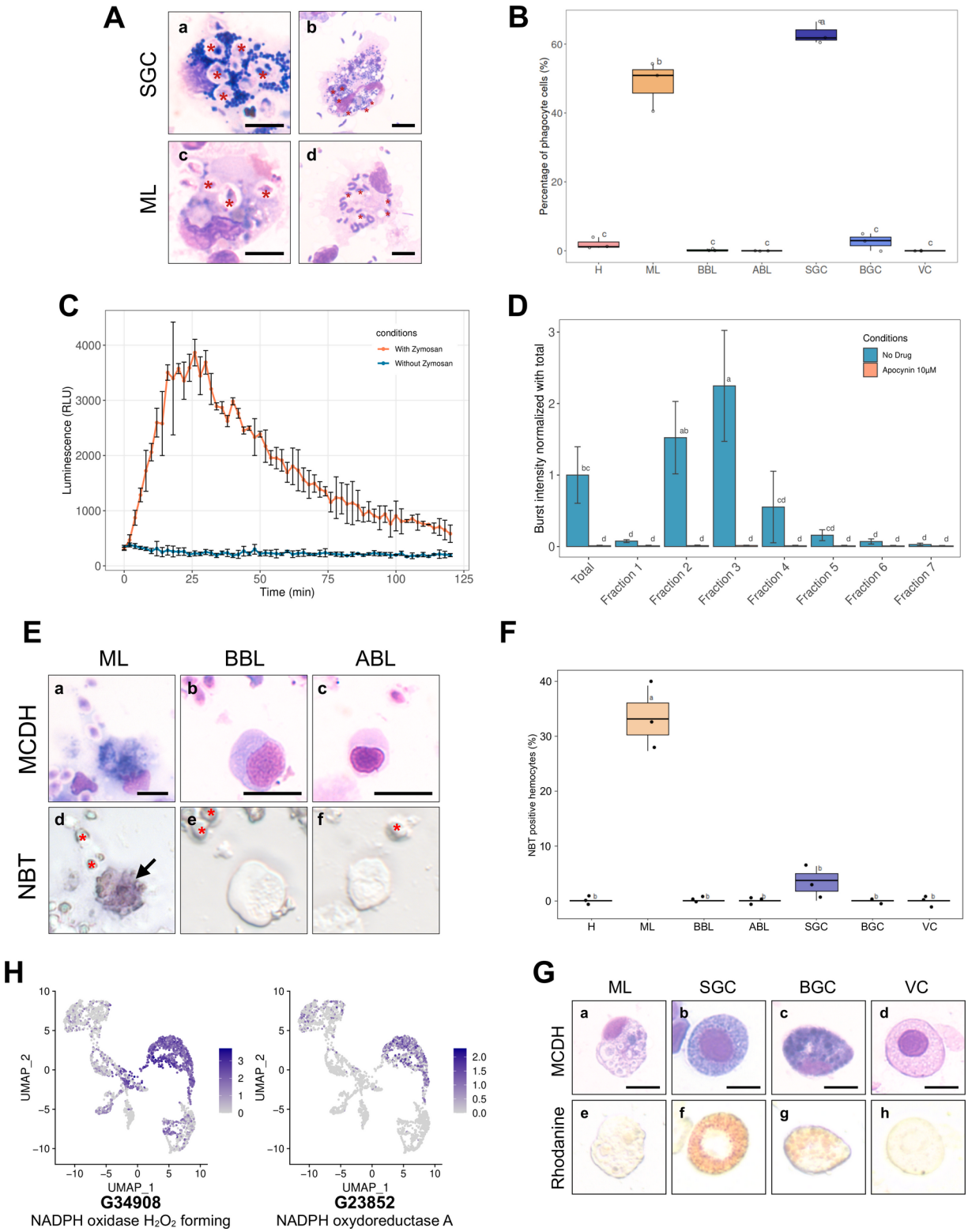

372 **Fig 5. Phagocytosis, Reactive Oxygen Species production capacity and copper storage of**

373 **hemocytes. (A)** Images of small granule cells (**SGC**) and macrophage-like (**ML**) cells with

374 phagocytosed zymosan particles (**panels a & c - red stars**) and *Vibrio tasmaniensis*

375 LMG20012^{T} bacteria (**panels b & d - red stars**) from whole hemolymph sample. Scale bar : 5

376 µm. **(B)** Quantification of the phagocytic activity of zymosan particles by each cell type. The

377 graph shows the result of 3 independent experiments. **(C)** Luminescence recording to detect
378 the production of Reactive Oxygen Species (ROS). In orange, a biphasic curve was obtained
379 on naive oyster hemolymph after zymosan addition at t = 0 min. In blue, the control condition
380 corresponds to hemocytes without zymosan addition. **(D)** Graph showing the intensity of ROS
381 production in each Percoll fraction. Normalized burst intensity was calculated from the
382 luminescence peak obtained from each fraction. In blue, no drug was added to the experiment,
383 in orange, ROS production was impaired by the addition of apocynin. **(E)** NBT
384 (NitroBlueTetrazolium) staining of hemocytes exposed to zymosan particles. Hemocytes
385 morphology after MCDH staining: Macrophage Like **(a**), Basophilic **(b)** and Acidophilic **(c)**
386 Blast cells. NBT staining of the different types of hemocytes **(d-f)**. Red stars show zymosan
387 and bacteria particles. Black arrows indicate Macrophage-Like cells. Scale bar : 10 µm **(F)**
388 Quantification of NBT-positive cells present in the total hemolymph of oysters exposed to
389 zymosan. **(H)** UMAP plots showing cells expressing NADPH oxidase found in the scRNA-
390 seq dataset and their expression level. **(G)** Labeling of intracellular copper stores in *C.gigas*
391 hemocytes. MCDH (upper panels) and rhodanine (lower panels) staining of oyster hemocytes
392 to reveal copper accumulation. Scale bar : 10µm. For panels **(B)**, **(D)** and **(F)** the alphabetic
393 characters displayed above the data points in each plot represent statistically significant
394 differences among the groups, as determined by Tukey's test following ANOVA. Groups
395 denoted by different letters differ significantly at the $p < 0.05$ level of statistical significance.
396 **H** : Hyalinocytes, **ABL** : Acidophilic Blast-Like cells, **BBL** : Basophilic Blast-Like cells,
397 **ML** : Macrophage-Like cells, **SGC** : Small Granule Cells, **VC** : Vesicular Cells and **BGC** :
398 Big Granule Cells.

399 The phagocytic activity of hemocytes was first tested on a sample of total oyster hemolymph.
400 Cells were incubated for 1 hour with either zymosan particles or the bacterial strain *Vibrio*
401 *tasmaniensis* LMG20012^T. Only the small granule cells and the macrophage-like cells
402 exhibited efficient phagocytosis for both zymosan or vibrios, as observed after MCDH
403 staining (**Fig. 5A, Supp. Fig. 6 and Supp. Fig. 7A**). Macrophage-like cells and small granule

404 cells showed a phagocytic activity of 49 % and 55 %, respectively, and a phagocytosis index
405 of 3.5 and 5.2 particles per cell respectively (**Fig. 5B and Supp. Fig. 7B**), as confirmed in 3
406 independent experiments. Very limited phagocytic activity was observed for hyalinocytes (1.7
407 %), basophilic blasts (0.18 %), and big granule cells (2.7 %) with a phagocytosis index of 2, 1,
408 and 2.5 particles per cell, respectively (**Fig. 5B and Supp. Fig. 7B**). These results confirmed
409 that only small granule cells and macrophage-like cells behave as professional phagocytes
410 demonstrating robust phagocytic activity.

411 **Only macrophage-like cells produce Reactive Oxygen Species.**

412 The next step was to assess the capacity of *C. gigas* hemocytes in each Pecoll fraction to
413 produce Reactive Oxygen Species (ROS) upon stimulation by zymosan, utilizing the Luminol
414 oxidation assay. Luminol luminescence peaked 25 minutes after exposure of hemocytes
415 (isolated from total hemolymph) to zymosan, indicating a robust oxidative burst (**Fig. 5C**).
416 The production of ROS was dependent on a NADPH oxidase, as it was completely inhibited
417 by the NADPH oxidase-specific inhibitor apocynin (**Fig. 5C**). To ascertain which hemocyte
418 types were involved in ROS production we tested Percoll density-sorted hemocytes for
419 oxidative burst activity. Fractions 2 and 3 displayed higher oxidative burst activity than the
420 other fractions. The burst intensity of fraction 3 was twice that of total hemocytes, and fraction
421 2 also exhibited significantly increased burst activity. In contrast, fraction 4 showed a
422 significant decrease in oxidative burst, and no activity was observed for fractions 1, 6 and 7
423 (**Fig. 5D**). These results indicate that NADPH-dependent oxidative burst activity is carried out
424 by fractions enriched in macrophage-like (ML) cells and blast-like cells (ABL and BBL).

425 Previous studies have shown that granular cells can produce ROS (*29*). In contrast, we found
426 that small granule cells collected in fraction 7 could not produce ROS through an oxidative
427 burst. To identify which type of hemocyte from blast-like cells and macrophage-like cells
428 produces ROS within a few minutes after exposure to zymosan, ROS production was
429 investigated using NitroBlueTetrazolium (NBT) reduction to stain hemocytes directly.

430 Correlative microscopic analysis using MCDH staining can then be conducted after the NBT
431 reduction reaction. Macrophage-like cells were strongly and significantly stained by NBT
432 reduction (33.2 %) (**Fig. 5E, panels a & d**). In contrast, some small granule cells were lightly
433 stained by NBT reduction (**Fig. 5F**). Blast-like cells, big granule cells, vesicular cells, and
434 hyalinocytes were never NBT stained, confirming that these cell types were not involved in
435 ROS production (**Supp. Fig. S7**). Taken together, these observations demonstrate that small
436 granule cells and macrophage-like cells are the two professional phagocytes among
437 hemocytes. However, only macrophage-like cells are capable of oxidative burst upon exposure
438 to zymosan. In light of these new functional data, we further analyzed the expression level of
439 NADPH-oxidase-related enzymes in the scRNA-seq dataset. The cells in cluster 1
440 predominantly expressed two NADPH oxidase isoforms (gene numbers G34908 and G23852)
441 compared to other clusters (**Fig. 5H**). Furthermore, this cluster expresses macrophage-specific
442 genes such as the angiopoietin receptor (**Table 1**), as well as maturation factors for dual
443 oxidase, an enzyme involved in peroxide formation (**Supp. Fig. S8**). Collectively, these data
444 indicated that cells of transcriptomic cluster 1 corresponded to macrophage-like cells.

445 **Small granule cells and big granule cells accumulate intracellular copper.**

446 The effects of copper on oyster hemocytes have been studied extensively due to its abundance
447 in polluted marine environments (*19*). In addition, several studies have shown that *Vibrio*
448 species pathogenic for *C. gigas* possess copper resistance genes, which are crucial for their
449 survival within hemocytes (*9*). This prompted us to investigate which hemocyte types are
450 involved in copper metabolism. To this end, total hemocytes were isolated from naive oysters
451 and stained with rhodanine to reveal copper storage in cells. Rhodanine staining revealed that
452 33 % +/- 2 % of small granule cells and 30 % +/- 10 % of big granule cells exhibited a specific
453 reddish/brown staining indicative of a high concentration of copper in their granules (**Fig. 5G**
454 **and Supp. Fig. S9**). These results provide functional proof that SGC are specialized in metal
455 homeostasis in addition to phagocytosis, as suggested by the scRNAseq data (Cluster 3).

456 **Antimicrobial peptides are expressed by agranular cells, blasts and hyalinocytes.**

457 Antimicrobial peptides (AMPs) have long been studied for their role in the invertebrate
458 humoral immune response. They are expressed by hemocytes, including those in *C. gigas (31)*.
459 The aim was to ascertain whether different hemocyte cell types expressed distinct AMPs.
460 However, due to the limited sequencing depth, the scRNA-seq analysis was not sensitive
461 enough to reveal AMP expression. This limitation was addressed by investigating AMP
462 expression through RT-qPCR on Percoll density-fractionated hemocytes. The results indicated
463 that Cg-Bigdefs 1-2, Cg-BPI and hemocyte defensin were predominantly expressed by
464 agranular cells, blasts and hyalinocytes (ABL, BBL and H) **(Fig. 6A, B and C)**. The
465 expression of these AMPs was associated with Blasts abundance, while the expression of Cg-
466 BigDefs 1-2 was only associated with hyalinocytes **(Fig. 6D)**. Granular cells (VC, ML, BGC
467 and SGC) did not seem to express any of the analyzed AMPs. These data suggest that some of
468 the agranular cells are specialized in the production of humoral effectors.

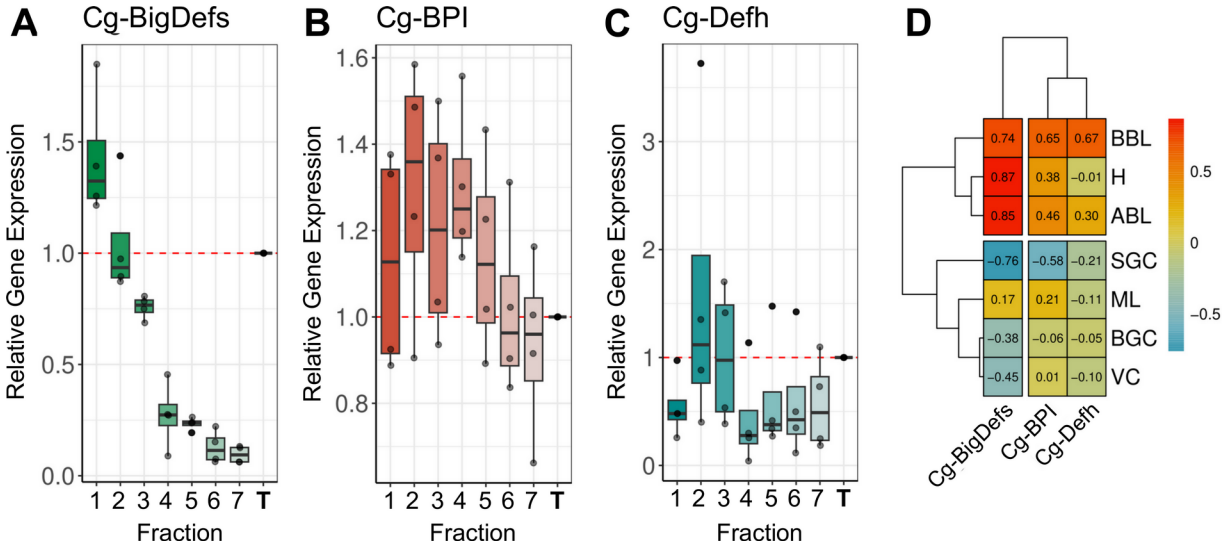

470 **Fig 6. Hemocyte expression profiles of some antimicrobial peptides. (A) (B)** and **(C)**
471 Relative Gene Expression in the 7 Percoll hemocyte fractions of Big-Defensin1 & 2 (Cg-
472 BigDefs), BPI (Cg-BPI) and hemocyte defensin (Cg-Defh), respectively, in comparison to the
473 gene expression level in unfractionated hemolymph. **(D)** Correlation matrix between the
474 relative gene expression of BigDefensin1 & 2, BPI and hemocyte defensin gene in each
475 fraction and the percentage of each hemocyte type in each fraction (**H** : Hyalinocytes, **ABL** :

476 Acidophilic Blast Like, **BBL** : Basophilic Blast Like, **SGC** : Small Granule Cell, **ML** :
477 Macrophage Like, **BGC** : Big Granule Cell, **VC** : Vesicular Cell. Values and color scale
478 represent the Pearson correlation coefficient (r) ranging from -1 (inverse correlation) to +1
479 (full correlation).

480 **Tentative model of hemocyte lineages and differentiation pathways in *C. gigas.***

481 The ontogeny, lineage and differentiation pathways of bivalves remain largely unknown (*32*).
482 However, there are some indications of circulating and proliferating hemocyte progenitors in
483 the hemolymph of *C. gigas* (*33*). GO-terms analysis of the 7 transcriptomic clusters revealed
484 different functional signatures, including the transcriptomic signature of cluster 4, which
485 showed a high expression level of ribosomal proteins (**Supp. Fig. S1J**) . This particularity has
486 been observed in hematopoietic stem cells in vertebrates (*34–36*). Furthermore, scRNA-seq
487 approaches can now be used to deduce differentiation pathways from mRNA splicing variant
488 analysis using bioinformatic tools like Monocle3 (*37*). This revealed an overexpression of
489 genes involved in the splicing, transcription and translation continuum in the same fourth
490 cluster (**Fig. 2**), thereby reinforcing the hypothesis of a pool of quiescent or immature cells
491 that can differentiate upon stimulation.

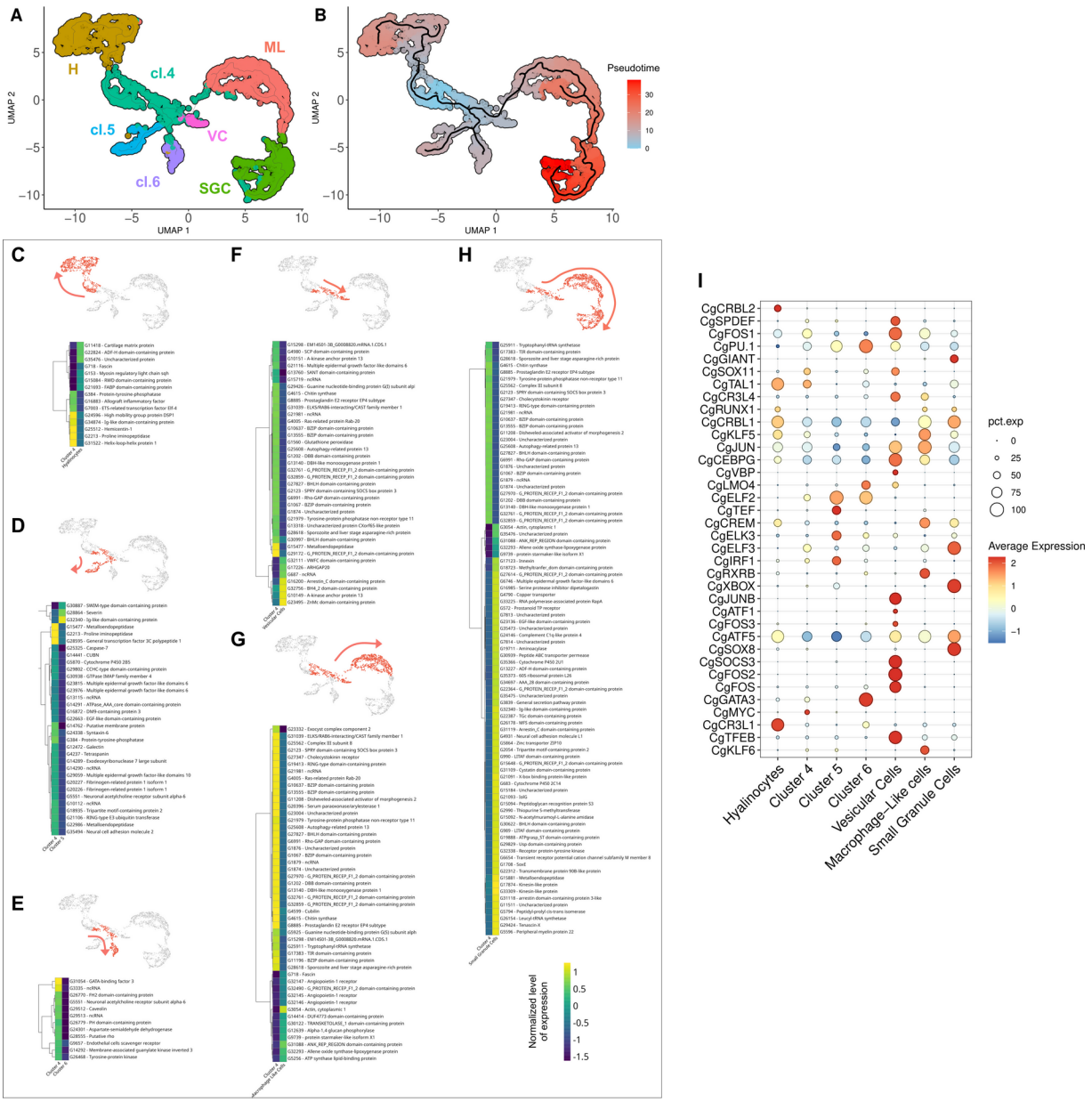

Figure 7. Pseudotime ordering of cells revealed 6 potential differentiation pathways of hemocytes. (A) UMAP plot of scRNA-seq analysis showing the 7 transcriptomic clusters used for pseudotime analysis. 4 clusters were identified cytologically (SGC for small granule cells - cluster 3, H for hyalinocytes - cluster 2, ML for Macrophage Like - cluster 1 and VC for vesicular cells - cluster 7), cl.4, cl.5, and cl.6 represent clusters 4, 5, and 6, respectively. **(B)** Graphical representation (UMAP projection) of the Monocle 3 pseudo-time order of the clustered cells. Cluster 4 (cl.4) was used as the origin for the pseudotime analysis. **(C) (D) (E) (F) (G) and (H)** show the gene expression level of selected marker genes obtained from the monocle3 trajectory analysis at the beginning and end of the modelized differentiation

502 pathways (in red on the UMAP plot) from cluster 4 to hyalinocytes, to cluster 5 cells, to
503 cluster 6 cells, to Vesicular Cells (VC), to Macrophage-Like cells (ML) and to Small Granule
504 Cells (SGC) respectively. The color scale represents the normalized expression level of each
505 gene. **(I)** Dot plot showing the average expression and the percentage of cells expressing
506 identified transcripts encoding for transcription factors in the scRNA-seq dataset. Average
507 expression is expressed in Log2FC.

508 Cluster 4 was chosen to enroot the pseudotime analysis to deduce differentiation pathways and
509 cell lineages using Monocle3. (**Fig. 7A**). By temporally ordering the 2817 cells analyzed by
510 scRNA-seq, 5 cell lineages could be defined (**Fig. 7B**). Differentiation pathway 1 leads to
511 hyalinocytes (H) (**Fig. 7C**). This transition is characterized by the downregulation of 8 genes,
512 two of which are transcription factors (G7003 and G31522). The hyalinocyte cluster was also
513 characterized by the overexpression of genes involved in cell contractility (G22824, G153 and
514 G11418). Differentiation pathway 2 leads to cells of cluster 5 and is characterized by the
515 downregulation of about 30 genes, and 3 genes related to Zn finger protein, actin cleavage and
516 Ig-like domain proteins were specifically overexpressed (G30887, G28864 and G32340) (**Fig.
517 7D**). Differentiation pathway 3 leads to cells of cluster 6 and is characterized by the down-
518 expression of 12 genes, and the upregulation of a GATA family transcription factor (G31054)
519 (**Fig. 7E**). The pathways between clusters 4, 5 and 6 found by Monocle3 analysis were pseudo
520 temporally short and few specific markers were identified, suggesting that they were
521 transcriptionally close. Differentiation pathway 4 leads to vesicular cells (VC) (**Fig. 7F**) where
522 a large number of genes were silenced to give rise to these cells. Seven genes were specifically
523 overexpressed in VC (G32111, G17226, G687, G16200, G32756, G10149 and G23495).
524 Interestingly, 6 genes encoding potential transcription factors were downregulated in this
525 lineage (G30997, G10637, G1067, G13555, G2123 and G27827). Differentiation pathway 5
526 leads to macrophage-like cells (ML), and is characterized by the underexpression of 35 genes
527 and the overexpression of 13 genes. Among the 35 genes, 6 are putative transcription factors
528 (G2123, G10637, G13555, G27827, G1067 and G11196) (**Fig. 7G**). Finally, we can outline a

529 lineage ending in small granule cells (SGC) (**Fig. 7H**). This pathway involved cluster 4
530 (immature cells), VC, ML and SGC and was characterized by the downregulation of 27 genes,
531 including 5 potential transcription factors (G10637, G13555, G27827, G1067 and G2123).
532 SGC showed a distinct transcriptomic signature with 61 overexpressed genes, including 3
533 transcription factors (G1708, G21091 and G30622). Based on these findings, we postulate that
534 immature cluster 4 cells possess pluripotent potential and can give rise to four terminally
535 differentiated cell types : cluster 5 and 6 cells, hyalinocytes and small granule cells, and two
536 other transient hemocyte cell types : vesicular cells and macrophage-like cells. All data from
537 the Monocle3 analyses are available as Supplementary Data (**Supp. Fig. S10**).

538 Differentiation pathway analysis thus revealed the over- or under-expression of various
539 transcription factors in the identified pathways. Given the established role of transcription
540 factors as master regulators of cell differentiation and their utility in delineating cell lineages,
541 we investigated the combinatorial expression patterns of transcription factors among the
542 different transcriptomic cell clusters. Based on GO-terms annotation, 28 different sequences
543 corresponding to transcription factors were isolated from the scRNA-seq dataset. The
544 transcription factor function was confirmed by manual annotation (**Supp. Table S5**) and
545 **Figure 7I** shows the average expression profiles of these factors in the different clusters.
546 **Supplementary Figure S11** illustrates their expression levels in single cells. Two
547 transcription factors, CgATF5 and CgCRBL1, exhibited a contrasting expression profile with
548 an increased average expression in macrophage-like cells, hyalinocytes and small granule cells
549 versus a low expression profile in cells in clusters 4, 5, 6 and vesicular cells. We also
550 identified transcription factors that were specifically expressed in the different transcriptomic
551 clusters : CgSPDEF, CgSOCS3, CgFOS and CgTFEB were specific for vesicular cells,
552 CgSOX8, CgXBOX and CgELF3 were specific for small granule cells, CgCR3L1 and
553 CgTAL1 for hyalinocytes, and CgJUN, CgKLF5, CgKLF6 and CgCREM for macrophage-like
554 cells. Eight additional transcription factors were specifically identified in cluster 6
555 (CgGATA3, CgPU.1 and CgELF2), cluster 5 (CgELF2, CgELK3 and CgIRF1) and cluster 4

556 (CgTAL1 and CgFOS1). These data potentially define four distinct hematopoietic lineages
557 originating from one type of immature blast cells and give rise to hyalinocytes, SGC (via VC
558 and ML), or two distinct differentiated blast-like cells. We also identified a combination of
559 transcription factors specific to lineages and cell types that are potential master regulators of
560 cell fate during hematopoiesis.

561 **Discussion**
562
563 The findings of our study represent a significant advancement in our understanding of the
564 functional diversity and lineages of *C. gigas* hemocytes. Single-cell RNA-seq and cytology
565 were combined to identify seven distinct hemocyte transcriptomic cell clusters and an
566 equivalent number of morphotypes. These include four granular cell types (big granule cells,
567 macrophage-like cells, small granule cells and vesicular cells), two distinct blast-like cells
568 (basophilic and acidophilic blast-like cells), and one agranular epithelial-like cell type
569 (hyalinocytes). A significant challenge was to identify correlations between transcriptomic and
570 cytological data to fully define each cytological cell type. This challenge was overcome by
571 combining multiple approaches, including isopycnic Percoll density gradient fractionation
572 combined with the analysis of transcriptomic markers expression, and functional assays
573 including phagocytosis, oxidative burst, copper accumulation, AMP expression and finally
574 pseudotime analysis of gene expression. These results confirmed the historical classification
575 of the 3 main cell groups : blasts, hyalinocytes, and granular cells (*15*) and deepened our
576 understanding of the functional specificities of poorly characterized cell types. In particular,
577 we identified distinct transcriptional and functional subtypes among blasts and granular cells
578 with complementary immune specialization and lineage relationships between cells.
579

580 One significant outcome of the present study is the identification of cell types involved in
581 antimicrobial activities, including phagocytosis, intracellular copper accumulation, an
582 oxidative burst and antimicrobial peptide production. These cell types have been extensively
583 studied for their role in antibacterial and antiparasitic defenses, as they are found in the large

584 majority of invertebrates (*17*). Nevertheless, there has been considerable debate surrounding
585 the cell types specialized for these critical immune functions in bivalves, particularly oysters.
586 Moreover, the involvement of the different hemocyte subpopulations in immune functions is
587 not yet fully understood.
588
589 Our findings reveal that the macrophage-like (ML) cells and small granule cells (SGC) are the
590 sole hemocyte cell types that function as professional phagocytes, as demonstrated against
591 Zymosan or *Vibrio*. These two distinct cell types could be distinguished functionally. First,
592 two distinct transcriptomic clusters were identified for each cell type (Cluster 1 for ML / BGC
593 and Cluster 3 for SGC). Secondly, only ML induced a measurable oxidative burst. Thirdly,
594 only SGC accumulated intracellular copper in specific granules. The two types of
595 professional phagocytes belong to the same granular cell lineage, as determined by
596 pseudotime analysis. The notion that ML could serve as a precursor for SGC may seem
597 counterintuitive. However, this is not an isolated phenomenon among invertebrate hemocytes.
598 For instance, in *Drosophila* larvae (*38*), some populations of professional phagocytes, the
599 sessile plasmatocytes, give rise to crystal cells or lamellocytes that are morphologically and
600 functionally distinct from plasmatocytes (*39*). Similarly, the existence of multiple professional
601 phagocytes in the oyster is reminiscent of vertebrate macrophages, polynuclear neutrophils
602 and dendritic cells, which possess distinct functional specializations, including efferocytosis
603 (*40*), oxidative burst, NETosis, or antigen presentation (*41*).
604
605 The characterization of professional phagocytes in oysters is of particular importance for a
606 deeper understanding of oyster-*Vibrio* interactions during pathogenesis. Some of the most
607 extensively studied oyster pathogens, including strains of *V. tasmaniensis* and *V. aestuarianus*
608 *francensis,* harbor virulence traits that enable them to disrupt the phagocytic activity of
609 hemocytes during pathogenesis. For instance, *V. tasmaniensis* behaves as a facultative
610 intracellular pathogen with phagocytosis-dependent cytotoxicity (*11*). Additionally, both *V.*

611 *tasmaniensis* and *V. aestuarianus* display resistance to copper toxicity through CopA and
612 CusA/B transporters. This trait is essential for the survival and virulence of these pathogens in
613 oysters (*9*, *42*). Since SGCs have been demonstrated to be professional phagocytes with
614 copper-rich granules, the cellular interactions between SGCs and these vibrios are likely to be
615 critical during the antibacterial host response and pathogenesis. ML are phagocytes that
616 possess a very potent NADPH-oxidase-dependent oxidative burst. The oxidative burst is a
617 rapid and potent antimicrobial response observed in professional phagocytes, such as
618 polynuclear neutrophils in mammals. It is worth noting that NADPH-dependent ETosis has
619 been observed in *C. gigas* in a manner analogous to that observed in human neutrophils (*43*).
620 This cell death is characterized by the projection of DNA extracellular traps that capture and
621 kill some pathogens like *Vibrio* (*43*). Therefore, it is reasonable to hypothesize that ML may
622 also be involved in ETosis.
623
624 The specialized functions of the two other types of granular cells, the BGCs and the VCs,
625 remain unclear. Despite the difficulty in identifying a specific scRNAseq transcriptomic
626 cluster for BGCs, the level of expression of laccase 24 was found to be higher in a particular
627 subcluster among ML (**Supp. Fig. S8**) and pseudo-time analysis highlighted the same
628 subcluster as an alternative differentiation state among ML (**Fig. 7B**). The enrichment of
629 transcripts involved in oxido-reduction pathways, particularly laccase 24, aligns with their
630 potential role in melanization and response to oxidative stress (*44*). While melanin-like
631 deposits have been observed in some cases of infestation by the parasites *Martelia* or B*onamia*
632 in the Sydney rock oyster (*45*), this mechanism is not as robust as that described in arthropods,
633 which perform melanization through a prophenoloxidase activation cascade (*46*, *47*). In many
634 marine invertebrates (*44*), a type of hemocyte known as Brown Cells could be related to the
635 BGCs described here. When observed without any staining (as in **Fig. 5F**), their big granules
636 with a yellow to dark brown content appear to align with the historical description of brown
637 cells that often infiltrate tissues (like gills) in animals exposed to polluted waters (*44*). It has

638 therefore been theorized that these cells are involved in detoxification processes. Our
639 pseudotime analysis indicates that they likely originate from ML, with limited phagocytosis
640 activity and a specialized role in melanization and potentially heavy metal detoxification, as
641 evidenced by rhodanine staining showing copper accumulation in some of their granules (**Fig.**
642 **5G**). Further studies are recommended to clarify the role of BGCs, particularly in the context
643 of parasitic infestation or exposure to toxic stresses. Lastly, VC are granular cells that remain
644 to be functionally characterized. Their transcriptomic profile suggests strong intracellular
645 vesicular trafficking and autophagy activity. However, our functional assays did not reveal
646 any particular immune-related function. Their clear granules appear auto-fluorescent when
647 illuminated with UV light (**Supp. Fig. S11**) but the biochemical nature of the content of these
648 granules remains to be characterized. As they also appear as cell intermediates along the
649 granular cell differentiation pathway in pseudotime analysis, they could represent functionally
650 immature precursors of the other three granular cell types, much like promyelocytes which
651 possess specific azurophilic granules but are functionally immature precursors during
652 granulocyte differentiation in humans. However, the enrichment of autophagy-related
653 transcripts in VC calls for further investigation into a potential role in antiviral immunity, as
654 autophagy has been suggested to play a role in the response to OsHV-1 virus (*48*).
655
656 Hyalinocytes are a homogenous cell type, with only one morphotype matching one
657 transcriptomic cluster. It can be deduced from pseudotime analysis that they originate from a
658 specific and very different differentiation pathway than the granular cells. According to the
659 literature, hyalinocytes are involved in the early stages of inflammation and can infiltrate
660 wounds and interact with foreign particles. In the flat oyster *Ostrea edulis*, they contribute to
661 shell production and wound healing (*49*). In the Sydney rock oyster they play a role in cell
662 aggregation (*50*), while in *C. virginica* (*51*) they contribute to encapsulation, reminiscent of
663 lamellocytes in *Drosophila*. Our results suggest an important role of AMP expression in the
664 immune response. Indeed, *Cg*-BigDefs, which participate in the control of oyster microbiota

665 (*52*), were found to be expressed in both hyalinocytes and blast-like cells. Moreover,
666 hyalinocytes from the oyster *O. edulis* have been shown to express the AMP Myticin C (*53*),
667 which lends further support to this immune function. Among the AMPs, we also found that
668 Cg-BPI and *Cg*-Defh, are more expressed in BBL, ABL than in other cell types. These results
669 are somewhat unexpected, given the prevailing assumption that AMPs are stored in granules
670 of granular cells, rather than agranular cells (*16*). These results highlight the necessity to
671 reassess the role of specific agranular cell types in the active production of humoral immune
672 effectors. Our findings suggest that hyalinocytes and/or the blast-like cells may be a cellular
673 target of the OsHV-1 virus, the causal agent of POMS, which dampens the expression of
674 certain AMPs (*7*), thereby inducing bacterial dysbiosis. It is still unclear whether this is due to
675 a decreased expression of AMPs and/or inhibition of immature blast cell differentiation
676 involved in the renewal of agranular cell types.
677
678 It should be noted that the complexity of blast-like cells could not be fully elucidated in this
679 study, as 3 clusters and only 2 morphotypes were identified. Cell fractionation using Percoll
680 gradient failed to yield pure blast-enriched fractions (ABL and BBL), preventing precise
681 functional characterization. The enrichment in transcripts of the transcription synthesis
682 degradation continuum aligns with the definition of undifferentiated blast-type cells and with
683 the basophilic staining obtained in MCDH for BBL cells, as immature blast cells are
684 characterized by a basophilic cytoplasmic staining in humans. However, our results show that
685 certain blast populations can produce AMPs, suggesting that these cells may also play a role in
686 the production of humoral effectors. Ultimately, it remains unclear whether these circulating
687 immature cells are indeed the stem cells from which all hemocytes originate.

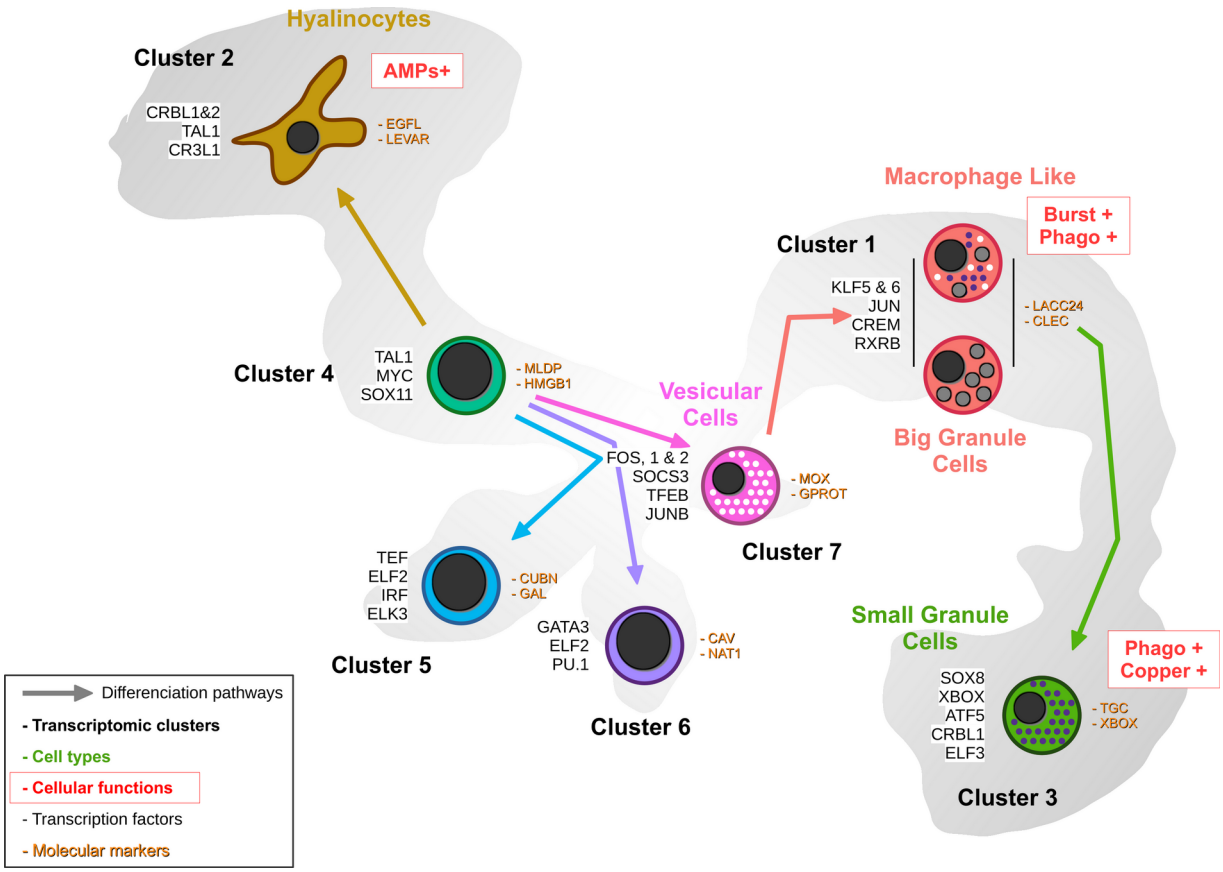

Figure 8. Proposed hemocyte ontology in *Crassostrea gigas* based on the transcriptomic, cytological and functional results obtained. Cells are colored according to the same color code as the transcriptomic clusters. Cluster numbers and cell types are indicated. To the left of the cells are the overexpressed transcription factors and to the right are the identified marker genes in each cluster. Functional characteristics of hyalinocytes, macrophage-like cells and small granule cells are marked in red. (**AMP** : AntiMicrobial Peptide, **Burst** : ROS production, **Phago** : phagocytosis)

In the animal kingdom, the innate immune system relies on specialized cells derived from pluripotent precursors through hematopoiesis. Transcription factors in particular have been found to exhibit a high degree of conservation throughout the animal kingdom, from invertebrates to vertebrates. However, the mechanisms underlying the functional differentiation of bivalves are only partially available or understood (*54*). Recent research has indicated the potential existence of hemocyte progenitors, also known as blast-like cells in several bivalve species. These include clams, mussels, scallops, marine mussels, freshwater mussels, oysters, pearl oysters, and wing shells (*54*). However, various models for

704 hematopoiesis in bivalves have been proposed and extensively debated without a clear
705 consensus or definitive proof. Single-cell RNA sequencing and pseudotime analysis have
706 enabled us to propose a refined model of hematopoiesis at an unprecedented level of detail. In
707 this model, the different types of hemocytes are likely produced through four differentiation
708 pathways that originate from a common progenitor. One pathway results in the formation of
709 agranular hyalinocytes, while another independent pathway gives rise to the granular cells,
710 including VC, ML, BGC, and SGC. Furthermore, two additional differentiation pathways
711 have been identified that may lead to terminally differentiated blast-like cells. The
712 differentiation of mature hemocytes involves the establishment of lineage-specific gene
713 expression profiles, which rely on transcription factors to modulate the expression of their
714 target genes. Our study identified a combination of transcription factors that are differentially
715 expressed during *C. gigas* hematopoiesis and are specific to differentiation stages and cell
716 lineages, including many well-known hematopoietic transcription factors such as GATA, PU-
717 1, TAL1 and SOX factors, which are positioned in this model of *C. gigas* hematopoiesis (*55–*
718 *57*) (**Fig. 8**).
719 This study significantly advances our understanding of bivalve immunity, especially in
720 comparison to arthropods. By introducing a standardized reference hemocytogram for oysters
721 using MCDH staining, defining cell type-specific markers and key transcription factors likely
722 involved in cell fate determination, as well as clarifying the functions of different hemocytes,
723 we have paved the way for future in-depth studies. This will facilitate further studies of the
724 oyster's immune response to various biotic and abiotic stress at the cellular level. Improved
725 comprehension of antiviral and antibacterial responses in bivalves, along with an enhanced
726 understanding of immune priming and immune memory at the cellular level in bivalves, will
727 benefit health and population management practices for sustainable aquaculture production.
728 These findings will also contribute to the broader field of evolutionary immunology by
729 enabling comparative studies and elucidating the diversification of immune cells and
730 immunity-related genes in a protostome.

731

732

733 **Materials and Methods**

734

735 **Conservation of oysters**

736 The work described here was performed using two different sources of oysters of the same
737 species *Crassostrea (Magallana) gigas*. ISA (Ifremer Standardized Oysters - La tremblade -
738 France) oysters for the scRNA-seq experiment and oysters provided by a local supplier
739 (https://www.huitres-bouzigues.com). Animals were washed and kept in 10 L tanks containing
740 seawater and a bubbler to oxygenate and homogenize the water. Water was changed daily and
741 oyster health was monitored. All animals used in this study were 18 months of age.

742 **Hemocyte collection and processing**

743 *Crassostrea gigas* hemocytes were collected from live animals by puncture of the adductor
744 muscle. The oyster shell was incised on the posterior side with forceps. Hemolymph was
745 collected using a 23Gx1" needle mounted on a 5 mL syringe prefilled with 2 mL of ice-cold
746 Alsever modified medium (20.8 g glucose – 8 g trisodium citrate - 22.5 g sodium chloride -
747 0.4 g BSA - pH=7.5). Samples were centrifuged for 4 minutes at 200 g – 4 °C and the
748 supernatant was removed and replaced with 1 mL of fresh Alsever modified medium. Each
749 hemocyte sample was thoroughly checked for quality, counted under a microscope using
750 KOVA (Kova International, USA) slides, and stored on ice prior to processing. For scRNA-
751 seq analysis, resuspended hemocytes were filtered on 30 µm filters, counted, the solution was
752 adjusted to 1.10^6 cells per mL and stored on ice prior to 10X genomic library preparation.

753 ***C. gigas* genome annotation**

754 The *C. gigas* genome (Genbank GCA_905397895.1) (*24*) was used as a reference. Prior to
755 annotation, the longest CDS sequences were extracted from the gff3 file. Annotation was
756 realized using the ORSON script (https://gitlab.ifremer.fr/bioinfo/workflows/orson). ORSON
757 combines cutting-edge tools for annotation processes within a Nextflow pipeline. The ORSON
758 script performs a sequence similarity search with BLAST (*58*) against the Uniprot-Swissprot
759 and Uniprot-trEMBL databases, and functional prediction with InterProScan (*59*) and eggNOG

760 (*60*) orthogroup annotation. Interproscan analysis was performed against Pfam, Prosite, CDD,
761 TIGR, SMART, SuperFamily, PRINTS and Hamap databases. Results were collected and
762 processed using Blast2GO (*61*) for annotation mapping and validation.

763 **Drop Seq-based scRNA-seq library generation**

764 The 10X Genomics protocol, Single Cell 3' Reagent Kits v2 User Guide from the
765 manufacturer (10X Genomics, USA) was followed to prepare gel in emulsion beads (GEM)
766 containing single cells, hydrogel beads, and reverse transcription reagents, perform barcoded
767 cDNA synthesis, and generate sequencing libraries from pooled cDNAs. The concentration of
768 single-cell suspensions was approximately 1000 cells / μL, as estimated by manual counting,
769 and cells were loaded according to the 10X protocol to capture approximately 3000 cells per
770 reaction. Library construction (after GEM digestion) was performed using 10X reagents
771 according to the manufacturer's instructions. Libraries (paired-end reads 75 bp) were
772 sequenced on an Illumina NovaSeq (Illumina, USA) using two sequencing lanes per sample.

773 **scRNA-seq analysis**

774 Reads were aligned to the *C. gigas* reference genome (Genbank GCA_905397895.1) (*27*)
775 using STAR solo software (v 2.7.10) (*23*). Unique molecular identifiers (UMIs) were extracted
776 and counted for each cell, and an expression matrix was generated for further analysis. Single-
777 cell RNA sequencing (scRNA-seq) data analysis was performed using the R programming
778 language (version 4.2.1) (R Core Team, 2018) and the Seurat package (version 4.3.0) (*62*). The
779 data were then pre-processed to remove unwanted sources of variation and to normalize gene
780 expression. Cells with small library sizes and a high proportion of mitochondrial genes were
781 excluded. Data normalization was performed using the SCTransform method. After
782 normalization, highly variable genes were identified using the FindVariableFeatures function
783 and the top variable genes were selected for downstream analyses. Dimensionality reduction
784 was performed using Principal Component Analysis (PCA), followed by Uniform Manifold
785 Approximation and Projection (UMAP) to visualize the data. Cell clustering was performed
786 using the 'FindClusters' function, using the previously identified significant principal

787 components (dims = 6) and a resolution parameter (r = 0.1) to define cluster granularity.
788 Differential expression analysis was performed using the 'FindAllMarkers' function (pct.min
789 = 0.25) to identify genes differentially expressed between clusters, with statistical significance
790 determined using the Wilcoxon rank sum test. Functional enrichment analysis of differentially
791 expressed genes was performed using gene set enrichment analysis (RBGOA) (*27*).

792 **KEGG pathway analysis**

793 KEGG analysis was performed using DAVID Bioinformatics Resources (NIAID/NIH) (*26*).
794 Gene lists of specifically overexpressed genes in each cluster were obtained after scRNA-seq
795 processing (genes with Log2FC > 0.25 and significant p-value < 0.001) and used for KEGG
796 annotation. The *C. gigas* reference genome from the DAVID bioinformatics resource was
797 used for this analysis, with thresholds of 2 for counts and 0.05 for EASE value (p-value).
798 KEGG annotation results were post-processed and presented as a heatmap showing the KEGG
799 pathway, fold enrichment, p-value significance and number of positive terms.

800 **Rank-Based Gene Ontology Analysis**

801 RBGOA first clusters GOs according to their representative genes to identify the most
802 significant GOs, and then ranks the identified biological processes according to their average
803 expression levels (over all representative genes). Finally, biological processes, molecular
804 functions and cellular components significantly enriched in DEGs are identified by a Mann-
805 Whitney rank test with a strict FDR correction. The files generated by the GO-MWU scripts
806 (https://github.com/z0on/GO_MWU) were post-processed to extract the category names and
807 the fraction indicating the number of "good candidates" relative to the total number of genes
808 belonging to that category. The "good candidates" were the genes that exceeded an arbitrary
809 'absValue' cutoff (defined as 0.001) in their significance measure. The results were presented
810 as a heatmap.

811 **Percoll Density Gradient Separation of Hemocytes**

812 A concentration series of Percoll (Cytiva, Sweden) diluted in Alsever modified medium was
813 prepared as follows: 10, 20, 30, 40, 50, 60 and 70 % (vol/vol). Discontinuous density gradients

814 (from 10 % Percoll with a density of 1.0647 to 70 % Percoll with d=1.1049) were made using
815 1.5 mL of each concentration and loaded with 1 mL of the hemocyte suspension
816 corresponding to approximately 2.10^7 cells. Centrifugation was performed (30 min, 800 g, 4
817 °C) in a swinging bucket on a Beckman Coulter JS-13.1 rotor (Beckman Coulter, USA).
818 Hemocytes concentrated at each density interface were collected separately with a 70 mm long
819 20Gx2.75" needle mounted on a 1 mL syringe. The hemocytes were then washed from the
820 Percoll by adding 10 mL of ice-cold Alsever modified medium, pelleted by centrifugation (10
821 min, 200 g, 4°C) and resuspended in Alsever modified medium or filtered seawater.

822 **Cytological description of the hemocyte populations**

823 200,000 fresh hemocytes were seeded onto a slide using a Cytospin 4 centrifuge (Thermo
824 Scientific, USA). The samples were then stained using the panoptic MCDH (Micro Chromatic
825 Detection for Hematology) (Cellavision, Sweden) staining protocol. This protocol produces
826 purple hues typical of Romanowsky-Giemsa staining results. After staining, the samples were
827 observed using a LEICA DMR (Leica AG, Germany) transmitted light microscope with a 40x
828 magnification objective. Each slide was imaged and the hemocytes were counted and
829 characterized based on their morphology.

830 **Real Time-quantitative Polymerase Chain Reaction (RT-qPCR)**

831 Total RNA was extracted using the RNeasy kit (Qiagen, the Netherlands) and cDNA was
832 synthesized from 1 µg total RNA using the Superscript IV kit (ThermoFisher Scientific, USA)
833 with oligo(dT) primers. RT-PCR was performed on LightCycler© 480 thermocycler using the
834 SYBR Green 1 Master kit (Roche, Switzerland). Primers were used at 200 nM. Primer
835 sequences are listed in **Supplementary Table S3**. Expression was normalized to *Cg-rps6*
836 reference gene. The standard cycling conditions were 95°C pre-incubation for 3 minutes
837 followed by 40 cycles of 95°C for 10 seconds, 60°C for 20 seconds, and 72°C for 25 seconds.
838 Each pair of primers was first tested and validated on a total hemocyte RNA preparation to
839 control melting curves and establish calibration lines.

840 **Oxidative Burst Assay**

841 The production of reactive oxygen species was quantified by luminescence assay. Briefly,
842 hemocytes from hemolymph puncture or Percoll density gradient were washed once with
843 filtered sterile water. 50 µL of hemocytes were plated in triplicate on a 96-well plate (3.10^5
844 cells/cm²). 50 µL of 40 mM luminol (Merck and Co, USA) was added to each well. After 45
845 minutes of incubation at room temperature, the oxidative burst was induced by adding 100 µL
846 of zymosan (Merck and Co, USA) at a multiplicity of infection (MOI) of 50:1. The plate was
847 immediately placed in a Berthold Centro XS3 LB 960 luminescence microplate reader
848 (Berthold GmbH, Germany) to measure luminescence emission every 2 minutes for 2 hours.

849 **Phagocytosis assay**

850 400 µL of filtered, sterile water-washed hemocytes were seeded in a 24-well plate at a
851 concentration of 3.10^5 cells/cm². After 15 minutes, 50 µL of zymosan was added to the
852 fractions at an MOI of 20:1. For LMG20012^T Vibrio, 50 µL of bacteria was added to a total
853 hemolymph at an MOI of 5:1. After 1 hour of contact at room temperature, the cells were
854 resuspended and 200 µL of the suspension was applied to a microscope slide using a Cytospin
855 centrifuge. The slides were then stained with MCDH and observed under a LEICA DMR
856 transmitted light microscope with a 40x magnification objective (Leica AG, Germany) to
857 count phagocytic cells.

858 **NitroBlueTetrazolium (NBT) staining**

859 ROS production was measured using NitroBlue Tetrazolium reduction after zymosan
860 stimulation. Briefly, 1 mL (1.10^6 cells) of hemocyte solution was mixed with 50 µL of filtered
861 NBT solution (15 mg/mL in water). Zymosan was added at a 4:1 MOI and the mixture was
862 incubated at room temperature for 10 minutes on a rocking shaker. Then, 50 µL of each
863 sample was plated onto glass coverslips and observed under a transmitted light microscope
864 LEICA DMR with a 40x magnification objective (Leica AG, Germany) to count NBT-positive
865 cells. The positions of positive NBT cells were recorded prior to MCDH staining to identify
866 hemocyte types.

867 **Rhodanine copper staining of hemocytes**

868 The storage of copper by hemocytes was examined by Rhodanine staining. Briefly, 1.10^5
869 hemocytes were plated on Superfrost slides using a cytospin and circled with a hydrophobic
870 pen to retain the staining solution. The Copper Stain Kit (SkyTek, USA) was used to stain the
871 hemocytes. As described by the kit manufacturer, one drop of Rhodanine solution was added
872 to 9 drops of acetate to form the working solution. Five drops were placed on the cytospin
873 cells and a 5 mL Eppendorf tube with the cap removed was placed over the cells to prevent
874 evaporation of the working solution. The slide and the balanced Eppendorf tube were placed
875 in a beaker of boiling distilled water for 20 minutes. The slide was then washed with 5 drops
876 of acetate and 3 drops of hematoxylin were placed on the slide for 1 minute at room
877 temperature. The slides were then washed a final time with acetate and observed under a
878 LEICA DMR transmitted light microscope with a 40x magnification objective (Leica AG,
879 Germany) to count rhodanine-positive cells. The positions of rhodanine-positive cells were
880 recorded prior to MCDH staining to identify hemocyte types.

881 **Pseudotemporal ordering of cells with Monocle3**

882 Cells from the *C. gigas* dataset were analyzed using Monocle3 (https://github.com/cole-
883 trapnell-lab/monocle3) (*37*). The Monocle3 analysis was performed on the Seurat object
884 following the aforementioned processing steps. Clustering information (features, genes,
885 partitions, clusters and UMAP coordinates) was transferred to a CDS object. The cell
886 trajectory was calculated using the *learn_graph* function. The *choose_graph_segments*
887 function was used to select three lineages. The gene expression along pseudotime data was
888 extracted from the result. Then, the data were used to plot genes along pseudotime in three
889 lineages using ggplot2 v3.4.4 R package and the heatmap was generated using the pheatmap
890 v1.0.12 R package.

891 **Statistical Analysis**

892 To evaluate differences between samples, a statistical analysis was performed using (version
893 4.2.1) (R Core Team, 2018) and appropriate packages. All data were examined for normality,
894 and statistical tests were selected accordingly. One-way analysis of variance (ANOVA) was

895 used for normally distributed data. Seven different hemolymph samples were used for
896 cytological analysis. Oysters were provided by our local supplier) and approximately 300
897 hemocytes were counted per sample. Seven independent experiments were performed for
898 Percoll density gradient separation. A Tukey test was used to evaluate the statistical difference
899 between the proportions of hemocyte types. The phagocytic capacity of hemocytes was tested
900 in three independent experiments and statistical differences were evaluated using the Tukey
901 test for both the phagocytic capacity between hemocyte types and the number of particles per
902 phagocyte. Finally, oxidative burst capacity was tested 3 times on Percoll-separated
903 hemocytes. The Tukey test was also used to assess statistical differences between conditions.
904 The null hypothesis was rejected at a significance level of $p = 0.05$.

905
906
907 **References**
908

1. Y. M. Bar-On, R. Phillips, R. Milo, The biomass distribution on Earth. *Proceedings of the National Academy of Sciences* **115**, 6506–6511 (2018).

2. B. Leicester Bayne, *Biology of Oysters* (Academic Press, 1st Edition., 2017)vol. 41.

3. G. Zhang, L. Li, J. Meng, H. Qi, T. Qu, F. Xu, L. Zhang, Molecular Basis for Adaptation of Oysters to Stressful Marine Intertidal Environments. *Annu. Rev. Anim. Biosci.* **4**, 357–381 (2016).

4. FAO, Global aquaculture production. Fisheries and aquaculture division (2023).

5. F. Pernet, C. Lupo, C. Bacher, R. J. Whittington, Infectious diseases in oyster aquaculture require a new integrated approach. *Philosophical Transactions of the Royal Society B: Biological Sciences* **371**, 20150213 (2016).

6. A. Alfjorden, M. Areskog, D. Bruno, R. Carnegie, D. Cheslett, S. Feist, S. Ford, S. Jones, A. Lillehaug, L. Madsen, T. Renault, N. Ruane, P. Vennerstrom, New Trends in Important Diseases Affecting the Culture of Fish and Molluscs in the ICES Area 2002– 2015. *ICES cooperative research report*, doi: 10.17895/ices.pub.2800 (2017).

7. J. de Lorgeril, A. Lucasson, B. Petton, E. Toulza, C. Montagnani, C. Clerissi, J. Vidal-Dupiol, C. Chaparro, R. Galinier, J.-M. Escoubas, P. Haffner, L. Dégremont, G. M. Charrière, M. Lafont, A. Delort, A. Vergnes, M. Chiarello, N. Faury, T. Rubio, M. A. Leroy, A. Pérignon, D. Régler, B. Morga, M. Alunno-Bruscia, P. Boudry, F. Le Roux, D. Destoumieux-Garzón, Y. Gueguen, G. Mitta, Immune-suppression by OsHV-1 viral infection causes fatal bacteraemia in Pacific oysters. *Nat Commun* **9**, 4215 (2018).

8. N. M. Coyle, C. O'Toole, J. C. L. Thomas, D. Ryder, E. J. Feil, M. Geary, T. P. Bean, A. W. Joseph, A. Waine, D. Cheslett, D. W. Verner-Jeffreys, Vibrio aestuarianus clade A and clade B isolates are associated with Pacific oyster (Magallana gigas) disease outbreaks across Ireland. *Microbial Genomics* **9**, 001078 (2023).

9. A. Mesnil, M. Jacquot, C. Garcia, D. Tourbiez, L. Canier, A. Bidois, L. Dégremont, D. Cheslett, M. Geary, A. Vetri, A. Roque, D. Furones, A. Garden, P. Orozova, I. Arzul, M. Sicard, G. M. Charrière, D. Destoumieux-Garzón, M.-A. Travers, Emergence and clonal expansion of Vibrio aestuarianus lineages pathogenic for oysters in Europe. *Molecular Ecology* **32**, 2869–2883 (2023).

10. D. Oyanedel, A. Lagorce, M. Bruto, P. Haffner, A. Morot, Y. Labreuche, Y. Dorant, S. de La Forest Divonne, F. Delavat, N. Inguimbert, C. Montagnani, B. Morga, E. Toulza, C. Chaparro, J.-M. Escoubas, Y. Gueguen, J. Vidal-Dupiol, J. de Lorgeril, B. Petton, L. Degremont, D. Tourbiez, L.-L. Pimparé, M. Leroy, O. Romatif, J. Pouzadoux, G. Mitta, F. Le Roux, G. M. Charrière, M.-A. Travers, D. Destoumieux-Garzón, Cooperation and cheating orchestrate Vibrio assemblages and polymicrobial synergy in oysters infected with OsHV-1 virus. *Proceedings of the National Academy of Sciences* **120**, e2305195120 (2023).

11. T. Rubio, D. Oyanedel, Y. Labreuche, E. Toulza, X. Luo, M. Bruto, C. Chaparro, M. Torres, J. de Lorgeril, P. Haffner, J. Vidal-Dupiol, A. Lagorce, B. Petton, G. Mitta, A. Jacq, F. Le Roux, G. M. Charrière, D. Destoumieux-Garzón, Species-specific mechanisms of cytotoxicity toward immune cells determine the successful outcome of Vibrio infections. *Proceedings of the National Academy of Sciences* **116**, 14238–14247 (2019).

12. Y. Labreuche, F. Le Roux, J. Henry, C. Zatylny, A. Huvet, C. Lambert, P. Soudant, D. Mazel, J.-L. Nicolas, Vibrio aestuarianus zinc metalloprotease causes lethality in the Pacific oyster Crassostrea gigas and impairs the host cellular immune defenses. *Fish Shellfish Immunol* **29**, 753–758 (2010).

13. M. Lafont, A. Vergnes, J. Vidal-Dupiol, J. de Lorgeril, Y. Gueguen, P. Haffner, B. Petton, C. Chaparro, C. Barrachina, D. Destoumieux-Garzon, G. Mitta, B. Gourbal, C. Montagnani, A Sustained Immune Response Supports Long-Term Antiviral Immune Priming in the Pacific Oyster, Crassostrea gigas. *mBio* **11**, 10.1128/mbio.02777-19 (2020).

14. M. Fallet, C. Montagnani, B. Petton, L. Dantan, J. de Lorgeril, S. Comarmond, C. Chaparro, E. Toulza, S. Boitard, J.-M. Escoubas, A. Vergnes, J. Le Grand, I. Bulla, Y. Gueguen, J. Vidal-Dupiol, C. Grunau, G. Mitta, C. Cosseau, Early life microbial exposures shape the Crassostrea gigas immune system for lifelong and intergenerational disease protection. *Microbiome* **10**, 85 (2022).

15. N. R. de la Ballina, F. Maresca, A. Cao, A. Villalba, Bivalve Haemocyte Subpopulations: A Review. *Front. Immunol.* **13**, 826255 (2022).

16. E. Bachère, R. D. Rosa, P. Schmitt, A. C. Poirier, N. Merou, G. M. Charrière, D. Destoumieux-Garzón, The new insights into the oyster antimicrobial defense: Cellular, molecular and genetic view. *Fish & Shellfish Immunology* **46**, 50–64 (2015).

17. J.-M. Escoubas, B. Gourbal, D. Duval, T. J. Green, G. M. Charrière, D. Destoumieux-Garzón, C. Montagnani, "Immunity in Molluscs" in *Encyclopedia of Immunobiology*, M. J. H. Ratcliffe, Ed. (Academic Press, Oxford, 2016; https://www.sciencedirect.com/science/article/pii/B9780123742797120041), pp. 417–436.

18. A. S. Mount, A. P. Wheeler, R. P. Paradkar, D. Snider, Hemocyte-Mediated Shell Mineralization in the Eastern Oyster. *Science* **304**, 297–300 (2004).

19. W. S. S. Fischer, "Environmental influence on bivalve hemocyte function" in *Am Fish Soc Symp* (1988)vol. 18, pp. 225–237.

20. T. V. Nguyen, A. C. Alfaro, F. Merien, Omics approaches to investigate host–pathogen interactions in mass mortality outbreaks of Crassostrea gigas. *Reviews in Aquaculture* **11**, 1308–1324 (2019).

21. J. Meng, G. Zhang, W.-X. Wang, Functional heterogeneity of immune defenses in molluscan oysters Crassostrea hongkongensis revealed by high-throughput single-cell transcriptome. *Fish & Shellfish Immunology* **120**, 202–213 (2022).

22. R. D. Rosa, P. Alonso, A. Santini, A. Vergnes, E. Bachère, High polymorphism in big defensin gene expression reveals presence–absence gene variability (PAV) in the oyster Crassostrea gigas. *Developmental & Comparative Immunology* **49**, 231–238 (2015).

23. B. Kaminow, D. Yunusov, A. Dobin, STARsolo: accurate, fast and versatile mapping/quantification of single-cell and single-nucleus RNA-seq data. bioRxiv [Preprint] (2021). https://doi.org/10.1101/2021.05.05.442755.

24. C. Peñaloza, A. P. Gutierrez, L. Eöry, S. Wang, X. Guo, A. L. Archibald, T. P. Bean, R. D. Houston, A chromosome-level genome assembly for the Pacific oyster Crassostrea gigas. *GigaScience* **10** (2021).

25. R. Satija, J. A. Farrell, D. Gennert, A. F. Schier, A. Regev, Spatial reconstruction of single-cell gene expression data. *Nat Biotechnol* **33**, 495–502 (2015).

26. B. T. Sherman, M. Hao, J. Qiu, X. Jiao, M. W. Baseler, H. C. Lane, T. Imamichi, W. Chang, DAVID: a web server for functional enrichment analysis and functional annotation of gene lists (2021 update). *Nucleic Acids Research* **50**, W216–W221 (2022).

27. R. M. Wright, G. V. Aglyamova, E. Meyer, M. V. Matz, Gene expression associated with white syndromes in a reef building coral, Acropora hyacinthus. *BMC Genomics* **16**, 371 (2015).

28. E. Bachère, D. Chagot, H. Grizel, Separation of Crassostrea gigas hemocytes by density gradient centrifugation and counterflow centrifugal elutriation. *Developmental & Comparative Immunology* **12**, 549–559 (1988).

29. W. Wang, M. Li, L. Wang, H. Chen, Z. Liu, Z. Jia, L. Qiu, L. Song, The granulocytes are the main immunocompetent hemocytes in Crassostrea gigas. *Developmental & Comparative Immunology* **67**, 221–228 (2017).

30. C. Lambert, P. Soudant, G. Choquet, C. Paillard, Measurement of Crassostrea gigas hemocyte oxidative metabolism by flow cytometry and the inhibiting capacity of pathogenic vibrios. *Fish & Shellfish Immunology* **15**, 225–240 (2003).

31. P. Schmitt, R. Rosa, M. Duperthuy, J. de Lorgeril, E. Bachère, D. Destoumieux-Garzon, The Antimicrobial Defense of the Pacific Oyster, Crassostrea gigas. How Diversity may Compensate for Scarcity in the Regulation of Resident/Pathogenic Microflora. *Frontiers in Microbiology* **3** (2012).

32. G. Vogt, Hidden Treasures in Stem Cells of Indeterminately Growing Bilaterian Invertebrates. *Stem Cell Rev and Rep* **8**, 305–317 (2012).

33. M. Jemaà, N. Morin, P. Cavelier, J. Cau, J.-M. Strub, C. Delsert, Adult somatic progenitor cells and hematopoiesis in oyster. *Journal of Experimental Biology*, jeb.106575 (2014).

34. S. P. Fahl, M. Wang, Y. Zhang, A.-C. E. Duc, D. L. Wiest, Regulatory Roles of Rpl22 in Hematopoiesis: An Old Dog with New Tricks. *Crit Rev Immunol* **35**, 379–400 (2015).

35. M. Rehn, A. Wenzel, A.-K. Frank, M. B. Schuster, S. Pundhir, N. Jørgensen, K. Vitting-Seerup, Y. Ge, J. Jendholm, M. Michaut, E. M. Schoof, T. L. Jensen, N. Rapin, R. T. Sapio, K. L. Andersen, A. H. Lund, M. Solimena, M. Holzenberger, D. G. Pestov, B. T. Porse, PTBP1 promotes hematopoietic stem cell maintenance and red blood cell development by ensuring sufficient availability of ribosomal constituents. *Cell Reports* **39**, 110793 (2022).

36. E. I. Athanasiadis, J. G. Botthof, H. Andres, L. Ferreira, P. Lio, A. Cvejic, Single-cell RNA-sequencing uncovers transcriptional states and fate decisions in haematopoiesis. *Nat Commun* **8**, 2045 (2017).

37. J. Cao, M. Spielmann, X. Qiu, X. Huang, D. M. Ibrahim, A. J. Hill, F. Zhang, S. Mundlos, L. Christiansen, F. J. Steemers, C. Trapnell, J. Shendure, The single-cell transcriptional landscape of mammalian organogenesis. *Nature* **566**, 496–502 (2019).

38. D. Hultmark, I. Andó, Hematopoietic plasticity mapped in Drosophila and other insects. *eLife* **11**, e78906 (2022).

39. U. Banerjee, J. R. Girard, L. M. Goins, C. M. Spratford, Drosophila as a Genetic Model for Hematopoiesis. *Genetics* **211**, 367–417 (2019).

40. E. Boada-Romero, J. Martinez, B. L. Heckmann, D. R. Green, The clearance of dead cells by efferocytosis. *Nat Rev Mol Cell Biol* **21**, 398–414 (2020).

41. D. C. Dale, L. Boxer, W. C. Liles, The phagocytes: neutrophils and monocytes. *Blood* **112**, 935–945 (2008).

42. A. S. Vanhove, T. P. Rubio, A. N. Nguyen, A. Lemire, D. Roche, J. Nicod, A. Vergnes, A. C. Poirier, E. Disconzi, E. Bachère, F. Le Roux, A. Jacq, G. M. Charrière, D. Destoumieux-Garzón, Copper homeostasis

at the host vibrio interface: lessons from intracellular vibrio transcriptomics. *Environmental Microbiology* **18**, 875–888 (2016).

43. A. C. Poirier, P. Schmitt, R. D. Rosa, A. S. Vanhove, S. Kieffer-Jaquinod, T. P. Rubio, G. M. Charrière, D. Destoumieux-Garzón, Antimicrobial Histones and DNA Traps in Invertebrate Immunity. *Journal of Biological Chemistry* **289**, 24821–24831 (2014).

44. G. Zaroogian, P. Yevich, Cytology and biochemistry of brown cells in *Crassostrea virginica* collected at clean and contaminated stations. *Environmental Pollution* **79**, 191–197 (1993).

45. B. Allam, D. Raftos, Immune responses to infectious diseases in bivalves. *Journal of Invertebrate Pathology* **131**, 121–136 (2015).

46. J. Nakhleh, L. El Moussawi, M. A. Osta, "Chapter Three - The Melanization Response in Insect Immunity" in *Advances in Insect Physiology*, P. Ligoxygakis, Ed. (Academic Press, 2017)vol. 52 of *Insect Immunity*, pp. 83–109.

47. P. Amparyup, W. Charoensapsri, A. Tassanakajon, Prophenoloxidase system and its role in shrimp immune responses against major pathogens. *Fish & Shellfish Immunology* **34**, 990–1001 (2013).

48. S. Picot, N. Faury, C. Pelletier, I. Arzul, B. Chollet, L. Dégremont, T. Renault, B. Morga, Monitoring Autophagy at Cellular and Molecular Level in Crassostrea gigas During an Experimental Ostreid Herpesvirus 1 (OsHV-1) Infection. *Front. Cell. Infect. Microbiol.* **12** (2022).

49. N. R. de la Ballina, A. Villalba, A. Cao, Differences in proteomic profile between two haemocyte types, granulocytes and hyalinocytes, of the flat oyster *Ostrea edulis*. *Fish & Shellfish Immunology* **100**, 456–466 (2020).

50. S. Aladaileh, S. V. Nair, D. Birch, D. A. Raftos, Sydney rock oyster (*Saccostrea glomerata*) hemocytes: Morphology and function. *Journal of Invertebrate Pathology* **96**, 48–63 (2007).

51. E. Rifkin, T. C. Cheng, H. R. Hohl, An electron-microscope study of the constituents of encapsulating cysts in the American oyster, *Crassostrea virginica*, formed in response to *Tylocephalum* metacestodes. *Journal of Invertebrate Pathology* **14**, 211–226 (1969).

52. N. De San Nicolas, A. Asokan, R. D. Rosa, S. N. Voisin, M.-A. Travers, G. Rocha, L. Dantan, Y. Dorant, G. Mitta, B. Petton, G. M. Charrière, J.-M. Escoubas, V. Boulo, J. Pouzadoux, H. Meudal, K. Loth, V. Aucagne, A. F. Delmas, P. Bulet, C. Montagnani, D. Destoumieux-Garzón, Functional Diversification of Oyster Big Defensins Generates Antimicrobial Specificity and Synergy against Members of the Microbiota. *Marine Drugs* **20**, 745 (2022).

53. N. R. de la Ballina, A. Villalba, A. Cao, Shotgun analysis to identify differences in protein expression between granulocytes and hyalinocytes of the European flat oyster Ostrea edulis. *Fish Shellfish Immunol* **119**, 678–691 (2021).

54. E. A. Pila, J. T. Sullivan, X. Z. Wu, J. Fang, S. P. Rudko, M. A. Gordy, P. C. Hanington, Haematopoiesis in molluscs: A review of haemocyte development and function in gastropods, cephalopods and bivalves. *Developmental & Comparative Immunology* **58**, 119–128 (2016).

55. M. de Bruijn, E. Dzierzak, Runx transcription factors in the development and function of the definitive hematopoietic system. *Blood* **129**, 2061–2069 (2017).

56. E. W. Scott, M. C. Simon, J. Anastasi, H. Singh, Requirement of transcription factor PU.1 in the development of multiple hematopoietic lineages. *Science* **265**, 1573–1577 (1994).

57. I. Bergiers, T. Andrews, Ö. Vargel Bölükbaşı, A. Buness, E. Janosz, N. Lopez-Anguita, K. Ganter, K. Kosim, C. Celen, G. Itır Perçin, P. Collier, B. Baying, V. Benes, M. Hemberg, C. Lancrin, Single-cell transcriptomics reveals a new dynamical function of transcription factors during embryonic hematopoiesis. *eLife* **7**, e29312 (2018).

58. S. F. Altschul, W. Gish, W. Miller, E. W. Myers, D. J. Lipman, Basic local alignment search tool. *Journal of Molecular Biology* **215**, 403–410 (1990).

59. P. Jones, D. Binns, H.-Y. Chang, M. Fraser, W. Li, C. McAnulla, H. McWilliam, J. Maslen, A. Mitchell, G. Nuka, S. Pesseat, A. F. Quinn, A. Sangrador-Vegas, M. Scheremetjew, S.-Y. Yong, R. Lopez, S. Hunter, InterProScan 5: genome-scale protein function classification. *Bioinformatics* **30**, 1236–1240 (2014).

60. C. P. Cantalapiedra, A. Hernández-Plaza, I. Letunic, P. Bork, J. Huerta-Cepas, eggNOG-mapper v2: Functional Annotation, Orthology Assignments, and Domain Prediction at the Metagenomic Scale. *Molecular Biology and Evolution* **38**, 5825–5829 (2021).

61. S. Götz, J. M. García-Gómez, J. Terol, T. D. Williams, S. H. Nagaraj, M. J. Nueda, M. Robles, M. Talón, J. Dopazo, A. Conesa, High-throughput functional annotation and data mining with the Blast2GO suite. *Nucleic Acids Research* **36**, 3420–3435 (2008).

62. Y. Hao, S. Hao, E. Andersen-Nissen, W. M. Mauck, S. Zheng, A. Butler, M. J. Lee, A. J. Wilk, C. Darby, M. Zager, P. Hoffman, M. Stoeckius, E. Papalexi, E. P. Mimitou, J. Jain, A. Srivastava, T. Stuart, L. M. Fleming, B. Yeung, A. J. Rogers, J. M. McElrath, C. A. Blish, R. Gottardo, P. Smibert, R. Satija, Integrated analysis of multimodal single-cell data. *Cell* **184**, 3573-3587.e29 (2021).

Acknowledgments

We are grateful to the staff of the Ifremer platform of "La Tremblade" for technical support in animal housing. scRNA-seq data generated and used in this work were produced through the MGX platform (University of Montpellier, CNRS ,INSERM). We thank the bioinformatic service of Ifremer (SEBIMER) for their help in bioinformatics and the qPCR platform GenSeq (University of Montpellier). We would like to thank Viviane Boulo and Danielle Mello for their enriching discussions, as well as all the members of the 2MAP laboratory team for the fruitful discussions throughout this project.

Ethics

This work did not require ethical approval from a human subject or animal welfare committee.

Funding

This work was funded by the Agence Nationale de la Recherche (MOSAR-DEF, ANR-19-CE18-0025; DECICOMP, ANR-19-CE20-0004 and TRANSCAN ANR-18-CE35-0009), the University of Montpellier, iSite MUSE and the "GT-Huître" initiative from Ifremer. This study falls within the framework of the "Laboratoires d'Excellence (LABEX)" Tulip (ANR-10-LABX-41). Sébastien De La Forest Divonne was awarded a PhD grant from the Region

Occitanie (HemoFight project) and the University of Perpignan Via Domitia graduate school ED305.

Author contributions

Conceptualization: G.M., D.D.-G., B.G., G.M.C. and E.V.

Methodology: S.d.L.F.D., J.P., G.M., D.D.-G., B.G., G.M.C. and E.V.

Investigation: S.d.L.F.D., J.P., G.M.C. and E.V.

Supervision: G.M.C. and E.V.

Writing (original draft): S.d.L.F.D. and E.V.

Writing (review and editing): all authors.

Competing interests

The authors declare that they have no competing interests.

Declaration of AI use

We have not used AI-assisted technologies in creating this article.

Data and materials availability

All data needed to evaluate the conclusions in the paper are present in the paper and/or the Supplementary Materials. Raw reads are available at ENA under the project accession number PRJEB74031.

Supplementary Materials for

Diversity and functional specialization of oyster immune cells uncovered by integrative single cell level investigations

Sébastien de la Forest Divonne *et al.*

*Corresponding author. Email:emmanuel.vignal@umontpellier.fr

This PDF file includes:

Data S1 to S3
Tables S1 to S5
Figs. S1 to S12

Data S1. Single-cell RNA-seq analysis result file. CSV file containing the scRNA-seq analysis results with cluster number (<cluster>), gene number (<gene>), chromosome reference where the gene is located (<chromosome>), average expression level (<avg_log2FC>), percentage in the cluster (<pct1>) and in other clusters (<pct2>), pct1 / pct2 ratio (<pct. ratio>), adjusted p-val and p-val values (<p-val> and <p_val_adj>), and gene description (<description>).

Data S2. Annotation file of CDS extracted from the *Crassostrea gigas* genome file. CSV file containing the annotation results collected and processed using Blast2GO for annotation mapping and validation.

Data S3. Compilation file for RBGOA results. CSV file containing concatenated results of all RBGOA tests used to draw gene ontology analysis heatmaps with cluster number (<cluster_number>), GO term universe (<goterm_universe>), number of good gene candidates (<number_of_good_candidates>), total number of genes in this GOTerm category (<total_number_of_genes_of_this_category>), GO term name (<goterm_name>), adjusted p-value (<pval-adj>) and GO term name variation (<variation>).

Number of Reads	127,959,215
Reads With Valid Barcodes	97.03 %
Sequencing Saturation	75.63 %
Q30 Bases in CB+UMI	96.14 %
Q30 Bases in RNA read	93.62 %
Reads Mapped to Genome: Unique+Multiple	89.22 %
Reads Mapped to Genome: Unique	82.01 %
Reads Mapped to Gene: Unique+Multiple Gene	72.26 %
Reads Mapped to Gene: Unique Gene	72.26 %
Estimated Number of Cells	2937
Unique Reads in Cells Mapped to Gene	67,950,796
Fraction of Unique Reads in Cells	73.48 %
Mean Reads per Cell	23,136
Median Reads per Cell	18,145
UMIs in Cells	16,306,374
Mean UMI per Cell	5552
Median UMI per Cell	4412
Mean Gene per Cell	1578
Median Gene per Cell	1434
Total Gene Detected	23,841

Table S1. STARsolo summary metrics report. Metrics dashboard obtained after the STARsolo step, describing the quality of the sequencing and the various characteristics of the cells detected after aligning the reads to the *C. gigas* genome from the Roslin Institute.

Cluster	KEGG Prefix	KEGG Number	KEGG Pathway	Fold Enrichment	P-value (<0.05)	Genes
1	crg	04144	Endocytosis	3.75	1.77E-06	G32465, G28245, G29411, G28554, G23342,G27546, G4677, G4248, G23299, G4679 G25017, G27834, G23833, G20650, G1765,G2151, G15227, G11863, G17437
1	crg	00030	Pentose phosphate pathway	10.19	4.25E-05	G30122, G34645, G20982, G31268, G25073 G11958, G17273
1	crg	00190	Oxidative phosphorylation	4.45	3.29E-04	G20983, G16716, COX2, COX1, ND1 CYTB, G2226, G3525, G3658, ND5
1	crg	01200	Carbon metabolism	3.54	1.77E-03	G30122, G18442, G34645, G20982, G31268 G16805, G25073, G11958, G17273, G7839
1	crg	00010	Glycolysis / Gluconeogenesis	4.94	6.58E-03	G34645, G20982, G11958, G23780, G7839 G13028
1	crg	00620	Pyruvate metabolism	5.26	1.38E-02	G18442, G22426, G22427, G23780 G7839
1	crg	03266	Virion - Herpesvirus	8.74	4.39E-02	G22034, G32778 G32842
2	crg	03010	Ribosome	11.87	5.45E-27	G5571, G25192, G5077, G3494, G33210,G26985, G26901, G23358, G1703, G1900 G1543, G2172, G12279, G5185, G26391,G10525, G4452, G11817, G25420, G2853 G4635, G3304, G25620, G5649, G3526,G740, G24712, G26976, G25626, G15236 G34618, G34615, G18702
2	crg	04814	Motor proteins	3.64	3.62E-04	G32475, G24506, G4572, G3088, G1531 G15286, G1299, G153, G22991, G1471 G10110, G1470
2	crg	00980	Metabolism of xenobiotics by cytochrome P450	4.61	2.17E-02	G5106, G26659, G18623, G18624 G14458
3	crg	00190	Oxidative phosphorylation	8.03	1.47E-12	G31970, G3073, G5034, G3298, G5653,G27276, G25266, G650, G331, G23645 G1779, G16296, G23701, G13193, G27816,G10181, G15131, G21371, G2133, G34736
3	crg	01200	Carbon metabolism	5.42	4.82E-08	G26194, G5034, G4037, G3500, G20764,G16296, G23701, G14096, G22912, G15171 G27816, G21794, G19054, G15078, G16455,G34649, G9692
3	crg	00010	Glycolysis / Gluconeogenesis	7.41	5.01E-06	G26194, G14096, G22912, G21794, G19054 G15078, G4037, G3500, G34649, G12763
3	crg	01230	Biosynthesis of amino acids	5.77	1.41E-05	G26194, G14096, G22912, G21794, G4037,G25300, G34649, G7042, G25304, G9692 G20764
3	crg	04144	Endocytosis	3.2	3.22E-05	G10612, G34830, G4232, G31680, G28015,G28554, G2650, G35288, G23530, G22892 G3216, G2800, G22524, G25627, G21676,G20683, G1765, G11863
3	crg	00020	Citrate cycle (TCA cycle)	8.23	1.48E-04	G16296, G23701, G5034, G15171, G27816 G19054, G16455
3	crg	01100	Metabolic pathways	1.27	1.48E-02	G13605, G5034, G3012, G3298, G650,G331, G22961, G5758, G14096, G27816 G13000, G2033, G4037, G3500, G34394,G23387, G25763, G20764, G1779, G23701 G13193, G21533, G15171, G19054, G15131,G1375, G21371, G12861, G9692, G3073 G8883, G31970, G30520, G25177, G27276,G5653, G16296, G2133, G16455, G34649 G7042, G9342, G26194, G23482, G6556,G23164, G5106, G25300, G25266, G25304 G23645, G25904, G22912, G21794, G15078,G10181, G22919, G16488, G34736, G12763 G2280
3	crg	00250	Alanine, aspartate and glutamate metabolism	4.26	2.79E-02	G23164, G25300, G25763, G25304 G20764
3	crg	00430	Taurine and hypotaurine metabolism	5.05	4.23E-02	G23482, G34394, G25763 G9342
4	crg	03010	Ribosome	11.18	2.38E-62	G32202, G25192, G4582, G5077, G3494,G33210, G33255, G5115, G5555, G11948 G31071, G23694, G4502, G732, G1703,G1900, G21588, G18212, G1543, G28190 G12279, G13687, G28274, G10525, G7023,G27586, G3387, G11817, G26894, G4635 G3304, G2853, G24036, G5649, G24712,G26976, G1172, G12546, G27592, G11965 G5571, G4085, G5375, G5652, G23471,G32582, G26985, G26901, G23358, G18432 G16773, G21360, G10473, G2172, G35349,G5185, G26391, G4452, G4972, G3885 G25420, G25620, G3526, G740, G2636,G25626, G16242, G15236, G34618, G1350 G34615, G18702
4	crg	03050	Proteasome	9.09	3.16E-14	G11447, G11879, G9178, G28086, G6441,G27078, G6503, G27105, G4954, G21626 G1667, G22517, G11085, G13469, G32646,G1140, G29381, G12565, G30766, G34613
4	crg	03040	Spliceosome	4.6	1.62E-13	G30069, G23072, G3035, G27237, G4644,G67, G3357, G28826, G21225, G22448 G21463, G20152, G31757, G12256, G16599,G2099, G16114, G11265, G19821, G5284 G4177, G23063, G3388, G35242, G23100,G2896, G5803, G21555, G22119, G18742 G13575, G14401, G10466
4	crg	00190	Oxidative phosphorylation	3.14	3.88E-04	G31970, G3077, G3298, G26024, G34551,G11926, G27610, G650, G2799, G17080 G1779, G1500, ND3, G31998
4	crg	03015	mRNA surveillance pathway	3.18	1.10E-03	G21555, G1768, G21245, G23072, G3035,G1892, G27237, G22452, G12561, G11265 G19821, G15119
4	crg	03013	Nucleocytoplasmic transport	2.44	9.12E-03	G21555, G1768, G23072, G4818, G3035,G2485, G31807, G27237, G12561, G11265 G19821, G27008
4	crg	04141	Protein processing in endoplasmic reticulum	2.06	1.28E-02	G11932, G29430, G10911, G22082, G26491,G29962, G2451, G2694, G6732, G4985 G20713, G204, G20332, G2609, G10994
5	crg	03010	Ribosome	7.41	1.68E-12	G27592, G32202, G5185, G5375, G33210,G27586, G11948, G26985, G3885, G26894 G3304, G2853, G18212, G18432, G16773,G1543, G16242, G21360, G13687, G2172 G12279
5	crg	00190	Oxidative phosphorylation	4.59	6.31E-04	G3430, COX2, COX1, ND1, CYTB ND3, ND2, ND5, ND4
5	crg	04137	Mitophagy - animal	4.65	8.54E-03	G30487, G25784, G29415, G3710, G22696 G12500
6	crg	03010	Ribosome	16.48	2.26E-55	G32202, G25192, G4582, G3494, G5115,G5555, G11948, G4502, G732, G1703 G21588, G18212, G1543, G28190, G12279,G13687, G10525, G7023, G27586, G3387 G11817, G26894, G4635, G3304, G2853,G24036, G5649, G24712, G26976, G27592 G5571, G4085, G5652, G26985, G26901,G23358, G18432, G16773, G21360, G10473 G2172, G5185, G26391, G3885, G25420,G25620, G740, G2636, G25626, G16242 G15236, G34618, G34615, G18702
7	crg	04144	Endocytosis	4.04	4.91E-09	G10612, G23299, G27538, G22524, G12273,G16951, G2151, G3185, G6211, G13317 G2450, G31680, G4232, G28015, G2650,G35288, G23342, G20567, G17254, G18762 G19412, G21991, G1774, G1993, G30759
7	crg	04137	Mitophagy - animal	4.99	3.50E-04	G18587, G25784, G11088, G2334, G30759 G3710, G27737, G30997, G12500
7	crg	04145	Phagosome	2.82	1.88E-03	G3185, G22181, G3430, G28015, G24310,G17795, G14056, G2026, G1780, G30759 G32778, G32842, G90
7	crg	04140	Autophagy - animal	2.97	3.47E-03	G20344, G5397, G25608, G25784, G11385,G2024, G11088, G30759, G10907, G21965 G12500
7	crg	04310	Wnt signaling pathway	2.9	6.82E-03	G24405, G23180, G11208, G35235, G16231 G2024, G14136, G2334, G1780, G2797
7	crg	04142	Lysosome	1.92	4.51E-02	G11645, G5397, G22181, G3430, G2026,G27524, G18705, G26324, G16202, G2976 G27526, G23337

Table S2. Table presenting the result of KEGG analysis performed using DAVID Bioinformatics Resources. GO term enrichment analysis was conducted on specifically overexpressed genes in each cluster obtained after scRNA-seq processing (genes with Log2FC > 0.25 and significant p-value < 0.001) to highlight the most relevant GO terms associated with a given gene list. The visualization of the different pathways can be obtained from the KEGG website using the KEGG prefix and KEGG number (https://www.genome.jp/kegg/pathway.html)

Target	Primer name	Sequence
Laccase 24	LACC24-F	CCT-TGA-TTC-TTC-TTG-CCA-TCC-G
	LACC24-R	AAA-GCT-TGC-GAT-CTT-TGG-CAA
C-type lectin domain-containing protein	CLEC-F	ATC-GGC-TTC-TAC-ATG-GAC-TGA-C
	CLEC-R	GTG-TCT-AAA-GCT-GCG-CCG-AT
Putative modulator of levamisole receptor-1	LEVAR-F	GTG-ACA-GAC-TTC-CCT-CAC-CCT
	LEVAR-R	GCA-CTG-AGT-CGA-GTC-GTA-TGT
EGF-like domain-containing protein 8	EGFL-F	GAG-TGT-TTG-ACA-GGA-CGA-AGC
	EGFL-R	CAT-CAT-CGT-TTC-CAA-CTG-AGG-C
X-Box binding protein-like domain	XBOX-F	GGG-TCA-ACA-GTG-CTA-GGC-AAT
	XBOX-R	GTA-AGC-CAC-CAT-CCC-TAC-CAC
Transglutaminase-like domain containing protein	TGC-F	CTA-CAA-GCT-GGA-CAC-CAC-CAA
	TGC-R	GCA-TTG-ACC-AGT-GAC-ACA-GTC
MD-2-related lipid-recognition domain containing protein	MLDP-F	CTT-GGA-CCT-CGT-TAT-CTT-CGC
	MLDP-R	CTC-CCT-CTG-GTC-CAC-AAA-CAA
High mobility group protein B1	HMGB1	GCC-CAC-GCT-GAA-CTA-TAC-AAG
	HMGB1	CAC-CTT-GTA-GTC-CCT-GAG-TGG
Galectin	GAL-F	CCA-CAG-TAT-CAA-CGA-CCC-TCC
	GAL-R	TCA-CTA-CCG-TCA-TAG-GGA-CCG
Cubilin	CUBN-F	TAA-GTT-CAC-TCT-GGC-CCA-AGG
	CUBN-R	GCT-CAT-GAT-CGT-AGT-GGT-GCT
Natterin-1	NAT1-F	CCG-TAC-GAT-GGT-GAG-GAG-AAA
	NAT1-R	CCG-TCC-CAC-ATA-CTT-GTC-GTT
Caveolin	CAV-F	TCC-AAA-TGA-CCA-TGA-CCC-AGA
	CAV-R	ACT-CTA-TTC-TTG-GTC-GCC-TGG
G Protein receptor F1-2 domain-containing protein	GPROT-F	CGA-ACG-CCT-GCT-TCT-GAT-ATG
	GPROT-R	TCC-ACA-TCG-AAT-GCT-CTG-TCT
DBH-like monooxygenase protein 1	MOX-F	CCT-CCG-CAG-CAA-GAA-GAA-GTA
	MOX-R	TTC-TGT-TTC-GTC-CTC-TCC-ACG
Ribosomal protein S6	RPS6-F	CAG-AAG-TGC-CAG-CTG-ACA-GTC
	RPS6-R	AGA-AGC-AAT-CTC-ACA-CGG-AC
Big Defensin 1&2	BigDef1-2-F	TTC-GCC-TGC-TTC-CAT-ACT-GG
	BigDef1-2-R	GTC-ATG-GTC-ACT-CCT-TAT-TC
Hemocyte defensin	HemDef-F	CTA-CCA-GTT-GTT-CAT-ACA-GAG
	HemDef-R	TCT-TGG-TCA-GAT-TCA-GTC-TGG
Bactericidal Permeability Increasing Protein	BPI	GGA-GGC-GGA-AAT-GGA-TTA-CT
	BPI	TGG-TTG-ACA-TCG-TTG-CTG-AC

Table S3. Sequences of primers used in this study. Name of the transcript targeted by the primer pair, name of the primer used in this study and nucleotide sequence of each primer.

Fraction	Cells	Average	Std.Dev.	Std.Error	Min	Max
1	H	46.43	9.47	4.73	37.50	59.63
1	ML	20.26	9.09	4.55	7.34	28.38
1	BBL	14.47	2.29	1.15	12.16	16.50
1	ABL	15.50	4.94	2.47	8.11	18.35
1	G	0.35	0.44	0.22	0.00	0.92
1	BGC	0.38	0.75	0.38	0.00	1.50
1	VC	2.62	1.97	0.98	0.92	5.41

Fraction	Cells	Average	Std.Dev.	Std.Error	Min	Max
2	H	20.17	5.26	2.63	14.10	26.56
2	ML	27.64	4.48	2.24	22.79	33.33
2	BBL	27.21	9.94	4.97	16.22	39.71
2	ABL	20.17	2.36	1.18	16.91	22.52
2	G	1.14	0.79	0.39	0.00	1.80
2	BGC	1.03	1.26	0.63	0.00	2.56
2	VC	2.64	1.56	0.78	0.74	4.50

Fraction	Cells	Average	Std.Dev.	Std.Error	Min	Max
3	H	12.49	3.78	1.89	10.08	18.04
3	ML	28.26	8.90	4.45	17.12	38.66
3	BBL	21.18	3.11	1.55	16.89	24.32
3	ABL	17.71	5.78	2.89	11.86	25.21
3	G	7.96	5.30	2.65	3.09	14.41
3	BGC	4.71	4.16	2.08	0.00	10.14
3	VC	7.68	2.87	1.43	4.20	10.81

Fraction	Cells	Average	Std.Dev.	Std.Error	Min	Max
4	H	7.82	5.97	2.99	2.20	14.29
4	ML	32.69	13.33	6.66	19.34	50.82
4	BBL	9.64	3.40	1.70	4.76	12.30
4	ABL	5.37	0.97	0.48	4.42	6.67
4	G	18.29	10.39	5.19	5.74	30.94
4	BGC	3.90	1.51	0.76	2.20	5.71
4	VC	22.29	8.25	4.12	11.48	30.77

Fraction	Cells	Average	Std.Dev.	Std.Error	Min	Max
5	H	4.29	4.41	2.21	0.76	10.45
5	ML	19.67	12.04	6.02	3.03	30.88
5	BBL	3.56	1.91	0.95	1.49	6.06
5	ABL	3.35	2.12	1.06	0.75	5.88
5	G	40.92	7.31	3.66	33.82	49.24
5	BGC	4.50	2.98	1.49	1.47	8.33
5	VC	23.71	4.48	2.24	17.91	28.79

Fraction	Cells	Average	Std.Dev.	Std.Error	Min	Max
6	H	3.57	3.82	1.91	0.65	9.09
6	ML	13.95	4.91	2.45	7.10	18.18
6	BBL	1.19	1.38	0.69	0.00	2.58
6	ABL	1.54	0.65	0.33	0.65	2.17
6	G	68.00	10.11	5.06	58.70	78.46
6	BGC	1.69	1.99	1.00	0.00	3.87
6	VC	10.06	5.30	2.65	3.08	15.94

Fraction	Cells	Average	Std.Dev.	Std.Error	Min	Max
7	H	2.43	3.04	1.52	0.00	6.31
7	ML	8.50	6.35	3.18	1.93	17.05
7	BBL	1.67	1.51	0.75	0.00	3.38
7	ABL	0.36	0.72	0.36	0.00	1.45
7	G	81.18	8.99	4.49	68.18	88.41
7	BGC	2.68	1.50	0.75	0.90	4.55
7	VC	3.18	2.92	1.46	0.00	6.82

Table S4. Hemocyte composition of the 7 Percoll fractions used for qPCR analysis. For each cell type in each fraction, the table presents the average percentage, standard deviation, standard error, minimum, maximum, and median count values.

			Blast alignment results						*Homo sapiens* Homologs	
Gene Number	Annotation Name	TF Name	Best Hit Blast Name	Specie	Accession number	Bit Score	Percentage Identity	Coverage	Name	Uniprot Number
G29966	Krueppel-like factor 15	CgKLF6	Krueppel-like factor 6	C.gigas	XP_011428991	659.448	100	100	HsKLF8	O95600
G30997	BHLH domain-containing protein	CgTFEB	Transcription factor EC isoform X1	C.gigas	XP_011447558	1089.72	100	100	HsTFEB	P19484
G17147	BZIP domain-containing protein	CgCR3L1	cAMP-responsive element-binding protein 3-like protein 1 isoform 1	H.sapiens	NP_443086	1060.06	100	100	HsCR3L2	Q70SY1
G3043	Transcriptional regulator	CgMYC	Transcriptional regulator Myc-A-like	C.angulata	XP_052688275	548.128	100	100	HsMYC	P01106
G31054	GATA-binding factor 3	CgGATA3	Transcription factor GATA-3 isoform X1	C.gigas	XP_011412780	966.066	100	100	HsGATA2	P23769
G11196	BZIP domain-containing protein	CgFOS	Proto-oncogene c-Fos	C.gigas	XP_011446784	664.84	100	100	HsATF3	P18847
G10637	BZIP domain-containing protein	CgFOS2	Fos-related antigen 2	C.gigas	XP_011439871	271.937	100	100	HsATF4	P18848
G2123	SPRY domain-containing SOCS box protein 3	CgSOCS3	SPRY domain-containing SOCS box protein 3	C.gigas	XP_011413771	488.804	100	100	HsSPSB4	Q96A44
G1708	SoxE	CgSOX8	Transcription factor Sox-8-like	C.gigas	NP_001295801	947.192	99.8	100	HsSOX9	P48436
G3506	BZIP domain-containing protein	CgATF5	cAMP-dependent transcription factor ATF-4	C.gigas	XP_011439092	566.614	85.9	100	HsATF5	Q9Y2D1
G11198	BZIP domain-containing protein	CgFOS3	Fos-related antigen 1	C.gigas	XP_034323853	456.062	100	99.62	none	none
G10636	BZIP domain-containing protein	CgATF1	Basic leucine zipper transcriptional factor ATF-like isoform X1	C.gigas	XP_011439867	270.011	100	99.41	none	none
G13555	BZIP domain-containing protein	CgJUNB	Transcription factor jun-B isoform X1	C.gigas	XP_011440881	224.557	100	99.33	none	none
G21091	X-box binding protein like protein	CgXBOX	X-box binding protein-like protein	C.ariakensis	AEF33390	375.491	80.5	99.12	none	none
G12164	Estrogen receptor	CgRXRB	Estrogen receptor beta	C.gigas	XP_011424805	1395.56	100	98.79	HsRXRA	P19793
G748	Interferon regulatory factor	CgIRF1	Interferon regulatory factor 1 isoform X1	C.gigas	XP_011449592	802.742	100	95.51	HsIRF1	P10914
G5204	ETS-related transcription factor Elf-3	CgELF3	ETS homologous factor isoform X1	C.gigas	XP_034310128	883.248	100	95.25	HsELF3	P78545
G28398	ETS domain-containing protein	CgELK3	ETS domain-containing protein Elk-3 isoform X1	C.gigas	XP_011421195	753.051	100	93.91	HsELK3	P41970
G35512	cAMP-responsive element modulator	CgCREM	cAMP-responsive element modulator isoform X2	C.gigas	XP_011448206	572.778	100	92.79	HsCREB1	P16220
G11013	BZIP domain-containing protein	CgTEF	Thyrotroph embryonic factor-like	C.virginica	XP_022332233	570.466	86.4	85.1	HsTEF	Q10587
G7003	ETS-related transcription factor Elf-4	CgELF2	ETS-related transcription factor Elf-2	C.gigas	XP_011447491	523.857	99.6	84.54	HsELF1	P32519
G27920	LIM domain transcription factor LMO4.1	CgLMO4	LIM domain transcription factor LMO4.1 isoform X2	C.gigas	XP_011443581	319.316	98.2	81.86	HsLMO4	P61968
G10865	BZIP domain-containing protein	CgVBP	Transcription factor VBP	C.gigas	XP_011457057	438.343	100	77.95	HsHLF	Q16534
G35439	BZIP domain-containing protein	CgCEBPG	CCAAT/enhancer-binding protein beta	C.gigas	XP_011452433	442.195	100	75.61	HsCEBPG	P53567
G2334	Proto-oncogene c-Jun	CgJUN	Transcription factor AP-1	C.gigas	XP_034313954	429.098	100	58.31	HsJUN	P05627
G26127	Krueppel-like factor 5	CgKLF5	Krueppel-like factor 5 isoform X1	C.gigas	XP_011421316	905.975	100	57.28	HsKLF7	O75840
G20682	cAMP-responsive element-binding protein-like 2	CgCRBL1	cAMP responsive element binding protein-like, partial	C.gigas	AAU93879	318.546	99.4	56.83	HsCRBL2	O60519
G17294	Runt-related transcription factor 1	CgRUNX1	Runt-related transcription factor 1-like isoform X5	C.angulata	XP_052711215	1085.86	100	56.68	HsRUNX3	Q13761
G10077	BZIP domain-containing protein	CgCR3L4	Clumping factor A isoform X1	C.gigas	XP_011425092	775.393	100	56.11	HsCR3L3	Q68CJ9
G2021	BHLH domain-containing protein	CgTAL1	T-cell acute lymphocytic leukemia protein 1-like isoform X1	C.gigas	XP_011439324	394.045	100	49.23	HsTAL2	Q16559
G2933	Putative transcription factor SOX-14	CgSOX11	Transcription factor Sox-11	C.gigas	XP_011445203	424.091	100	43.97	HsSOX12	O15370
G11358	BZIP domain-containing protein	CgGIANT	Protein giant	C.gigas	XP_011417277	486.108	100	38.41	HsTEF	Q10587
G6354	ETS domain-containing protein	CgPU.1	ETS-related transcription factor Elf-3	C.gigas	XP_034320185	189.119	100	36	HsPU.1	P17947
G10633	BZIP domain-containing protein	CgFOS1	Fos-related antigen 1	C.gigas	XP_019918193	371.719	99.5	31.4	HsFOSL1	P15407
G6394	ETS domain-containing protein	CgSPDEF	SAM pointed domain-containing Ets transcription factor-like isoform X2	C.gigas	XP_052697855	356.681	99.4	30.12	HsSPDEF	O95238
G32716	cAMP-responsive element-binding protein-like 2	CgCRBL2	cAMP-responsive element-binding protein-like 2 isoform X1	C.gigas	XP_034309865	297.745	83.4	26.7	HsCRBL2	O60519

Table S5. Transcription factors identified in the scRNA-seq dataset of *Crassostrea gigas* hemocytes. Transcription factors identified in the scRNA-seq dataset and their homology with human proteins, as indicated by the blast alignment results. Each entry includes the gene identifier, the protein it represents in *C.gigas*, and its human counterpart. The bit score and coverage indicate the strength and extent of the alignment, respectively.

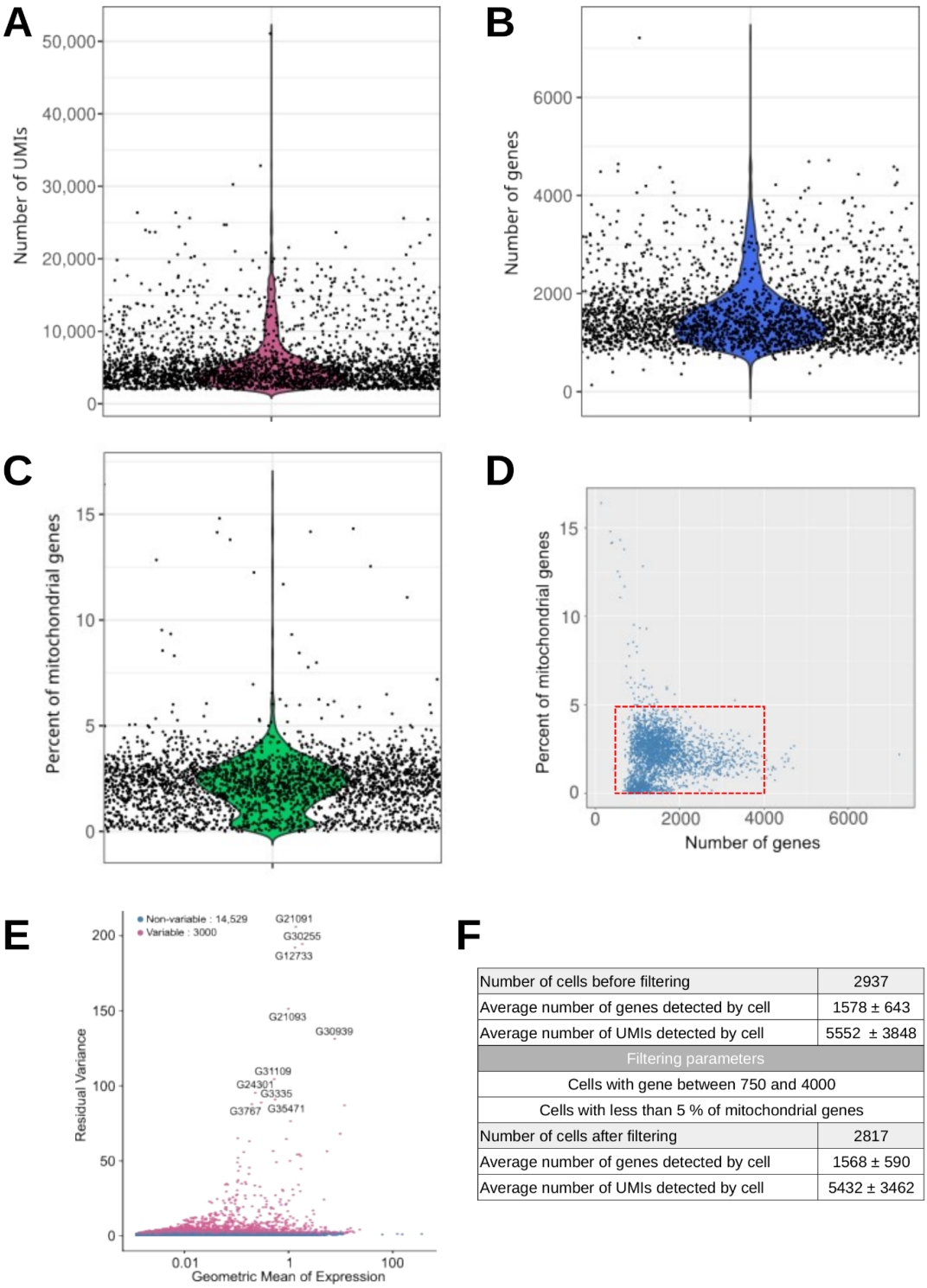

F

Number of cells before filtering	2937
Average number of genes detected by cell	1578 ± 643
Average number of UMIs detected by cell	5552 ± 3848
Filtering parameters	
Cells with gene between 750 and 4000	
Cells with less than 5 % of mitochondrial genes	
Number of cells after filtering	2817
Average number of genes detected by cell	1568 ± 590
Average number of UMIs detected by cell	5432 ± 3462

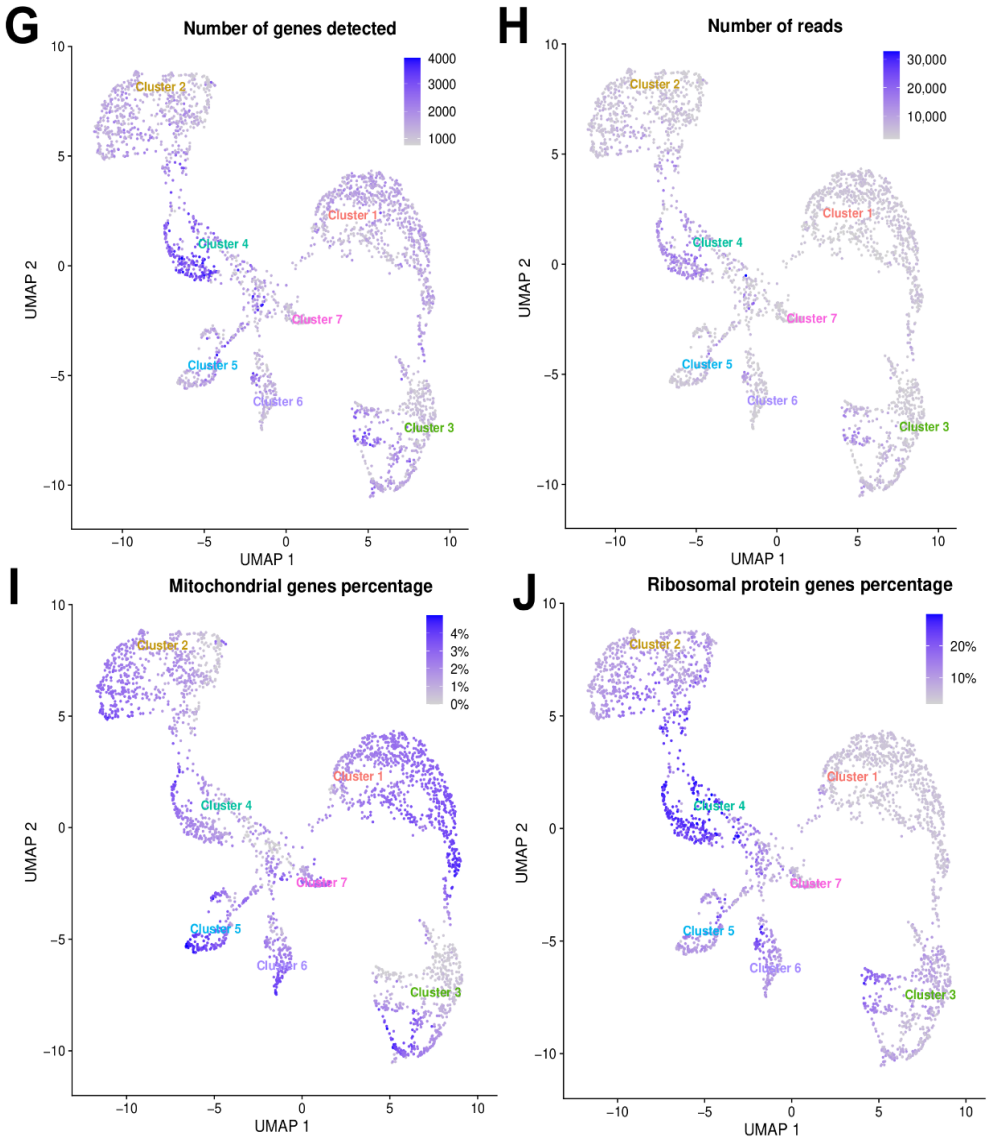

Figure S1. ScRNA-seq quality control metrics. Distribution of **A)** unique molecular identifiers (UMIs), **B)** genes and **C)** percentage of mitochondrial genes detected per cell. Each dot represents one cell. **D)** Plot of the percentage of mitochondrial genes versus the number of genes detected in each cell. The red box represents the cells selected for further analysis (number of genes detected between 750 and 4000 and with a percentage of mitochondrial genes less than 5%) **E)** The *FindVariableFeatures()* function was used to identify features with high cell-to-cell variation in the dataset to highlight the biological signal in the single cell dataset. **F)** Table

summarizing some quality control metrics. The table shows the thresholds to remove poor quality cells (doublets or empty droplets). The number of cells, UMIs and genes before and after filtering are shown. **G)** Uniform Manifold Approximation and Projection (UMAP) plot of the cells with the number of expressed genes. **H)** UMAP plot of the number of reads per cell. **I)** UMAP plot of the percentage of mitochondrial genes in each cell. **J)** UMAP graph of the percentage of ribosomal protein transcripts in each cell.

A

Stage	Number of CDS	% of CDS
Input	30,724	100
Database querying		
Blast annoted	30,511	99.3
Interpro annoted	30,718	99.9
EggNogg annoted	12,630	41.1
Blast2Go		
Mapped	28,570	92.9
Annotated	22,462	73.1

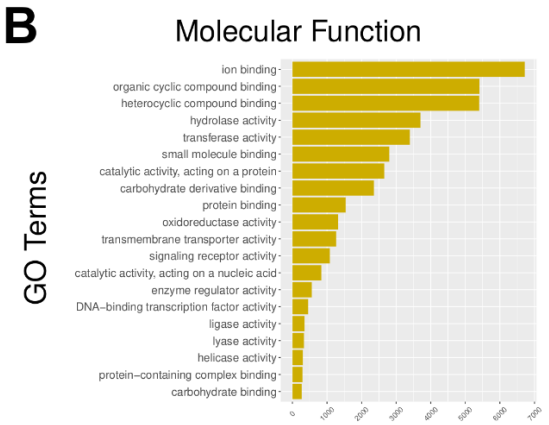

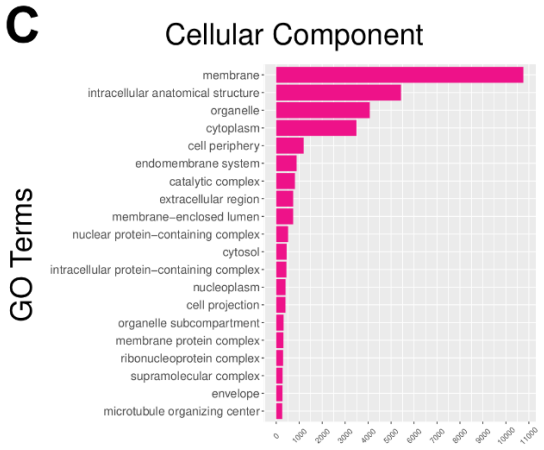

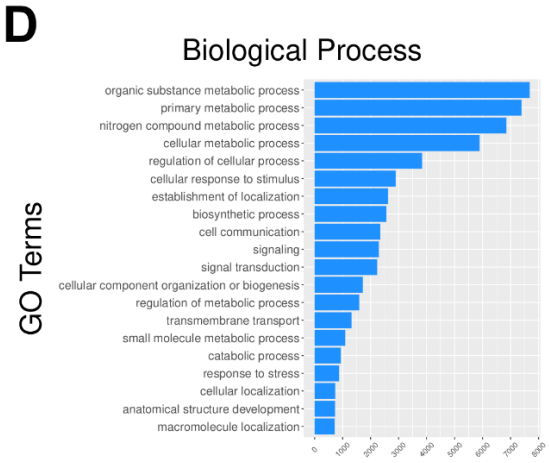

Figure S2. Results of the *C. gigas* genome re-annotation. A) The number and percentage of Coding DNA Sequences (CDS) with valid annotation after each annotation step are shown. A BLAST query was performed against the TrEMBL/Uniprot database and InterproScan annotation against Pfam, PrositeSiteProfiles, CDD, TIGRFAM, PRINTS, SMART, SUPERFAMILY and Hamap databases. Blast and InterProScan results were compiled and processed using Blast2Go. A first mapping step was used to enrich the Blast result with GO-terms, and the annotation step was used to optimize and validate the GO-terms annotations. **B) C)** and **D)** show the distribution of the various categories of GO-terms across the three primary domains of Gene Ontology : Molecular Function, Cellular Component and Biological Process, respectively.

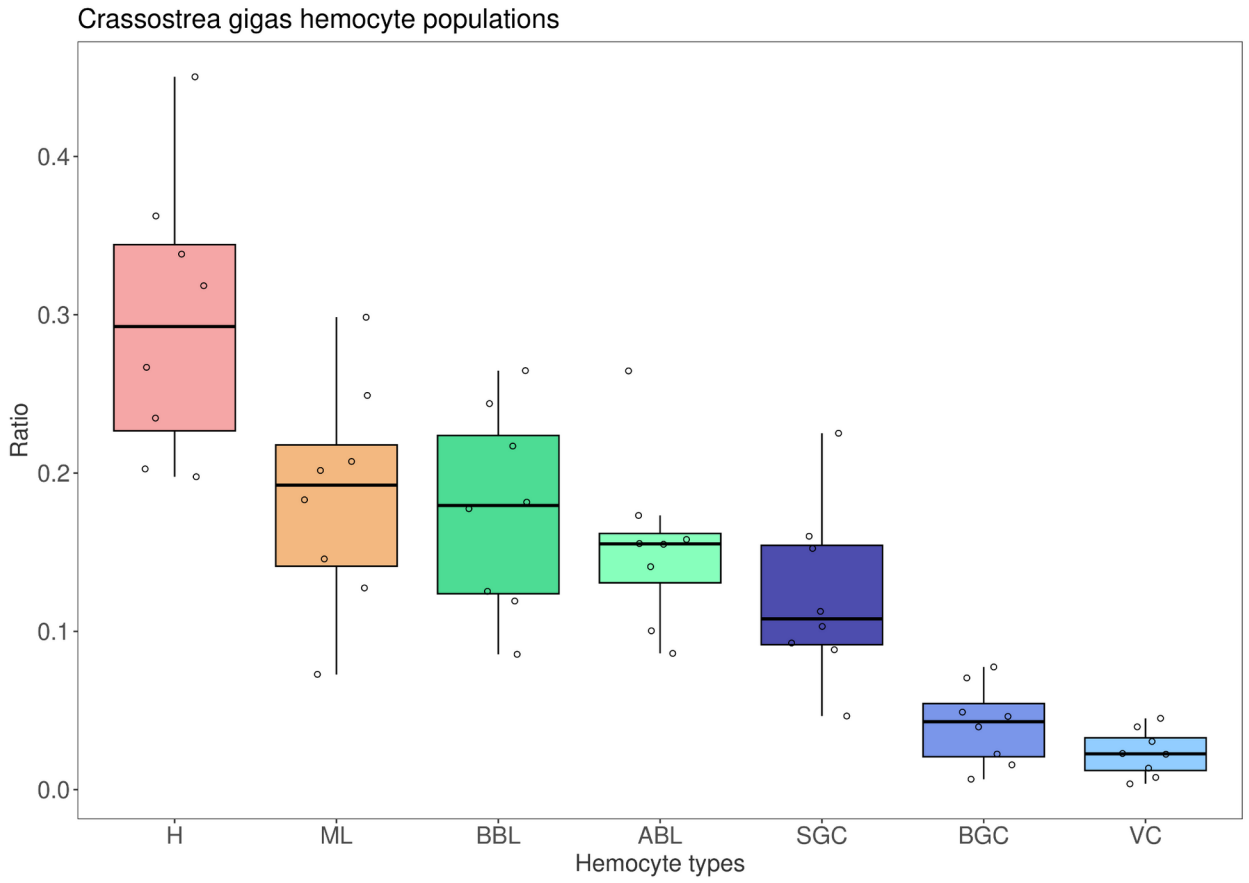

Figure S3. Whisker plot showing the distribution of counts of different hemocyte populations. Hemolymph was collected from eight different oysters and hemocytes were plated on a slide using cytospin centrifugation. The proportion of each hemocyte type in these hemolymphs was calculated after MCDH staining. **H** : Hyalinocytes, **ML** : Macrophage-Like cells, **BBL** : Basophilic Blast-Like cells, **ABL** : Acidophilic Blast-Like cells, **SGC** : Small Granule Cells, **BGC** : Big Granule Cells, and **VC** : Vesicular Cells. The calculation of the proportion of each cell type in these hemolymphs reveals a heterogeneous composition of hemocytes between individuals as well as between cell types.

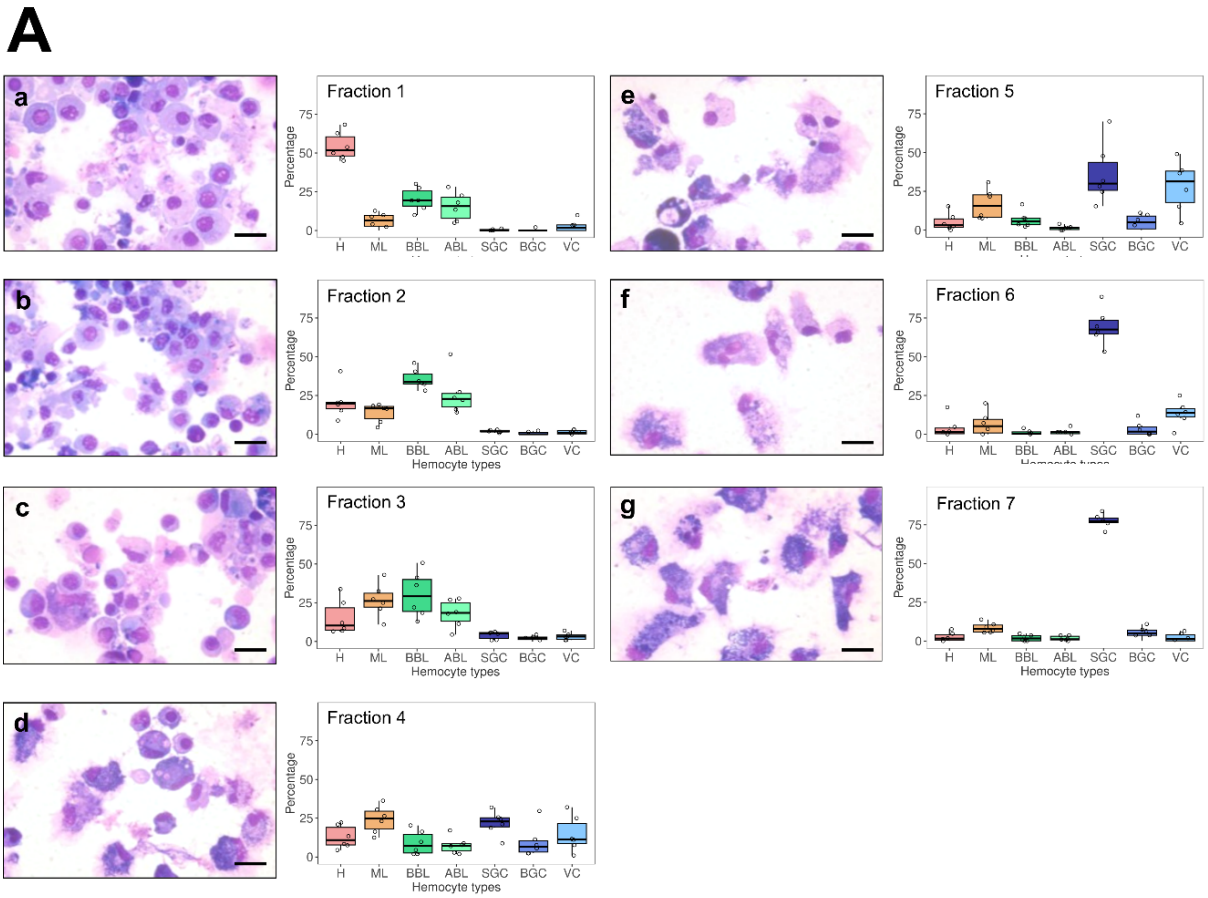
A
a
Fraction 1
b
Fraction 2
c
Fraction 3
d
Fraction 4
e
Fraction 5
f
Fraction 6
g
Fraction 7
Percentage
Hemocyte types
H
ML
BBL
ABL
SGC
BGC
VC

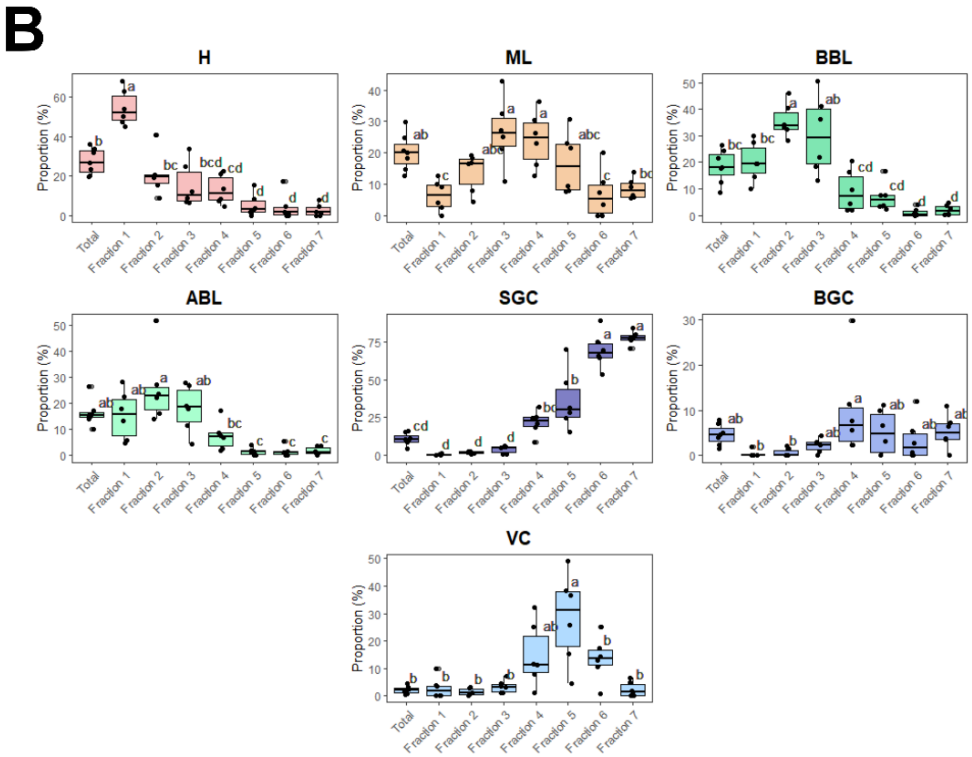
B
H
ML
BBL
ABL
SGC
BGC
VC
Proportion (%)
Total
Fraction 1
Fraction 2
Fraction 3
Fraction 4
Fraction 5
Fraction 6
Fraction 7

Figure S4. Statistical significance of enrichment in different hemocyte types in Percoll gradient fractions. (A) a,b,**c**,**d**,**e**,**f**, and **g** : MCDH staining of cells from the 7 fractions isolated from the percoll gradient in (B). Scale bar : 10 µm. **Fraction 1 to 7 :** Quantification of the different types of hemocytes found in each of the 7 fractions from 5 independent fractionation experiments. **(B)** Statistical significance of enrichment of different hemocyte types in Percoll gradient fractions. Results are from six independent experiments. Statistical significance is indicated by letters, as different letters indicate a significant difference between enrichments of cell types within the Percoll density gradient fractions (ANOVA, Tukey's test, p-value <0.05). Hyalinocytes (**H**) were significantly enriched in the first fraction compared to the other fractions and compared to unsorted hemocytes. However, they were significantly depleted in fractions 4, 5, 6 and 7 compared to unsorted hemocytes. Macrophage-like cells (**ML**) were significantly enriched in fractions 3 and 4 compared to fractions 1, 6 and 7. They were depleted in fraction 1 compared to unsorted hemocytes. Acidophilic blasts (**ABL**) were significantly depleted in fractions 4, 5, 6, and 7 compared to unsorted hemocytes. Basophilic blasts (**BBL**) were significantly enriched in fractions 2 and 3 compared to fractions 4, 5, 6, and 7 and in fraction 1 compared to fractions 6 and 7. Compared to unsorted hemocytes, basophilic blasts (**BBL**) were significantly enriched in fraction 2 and depleted in fractions 6 to 7. Small granule cells (**SGC**) were significantly depleted in fractions 1, 2, and 3 compared to fractions 4, 5, 6, and 7, and also significantly depleted in fractions 4 and 5 compared to fractions 6 and 7. In addition, small granule cells (**SGC**) were significantly enriched in fractions 5, 6, and 7 compared to unsorted hemocytes. The distribution of the big granule cells (**BGC**) showed a significant enrichment in fraction 4, compared to fractions 1 and 2, but no significant changes were observed with unsorted hemocytes. Vesicular cells (**VC**) were enriched in fraction 5 compared to fractions 1, 2,

3, 6, 7 and unsorted hemocytes in fractions 1, 2, and 3 compared to fraction 5 and enriched in fraction 5 compared to fraction 7 and unsorted hemocytes.

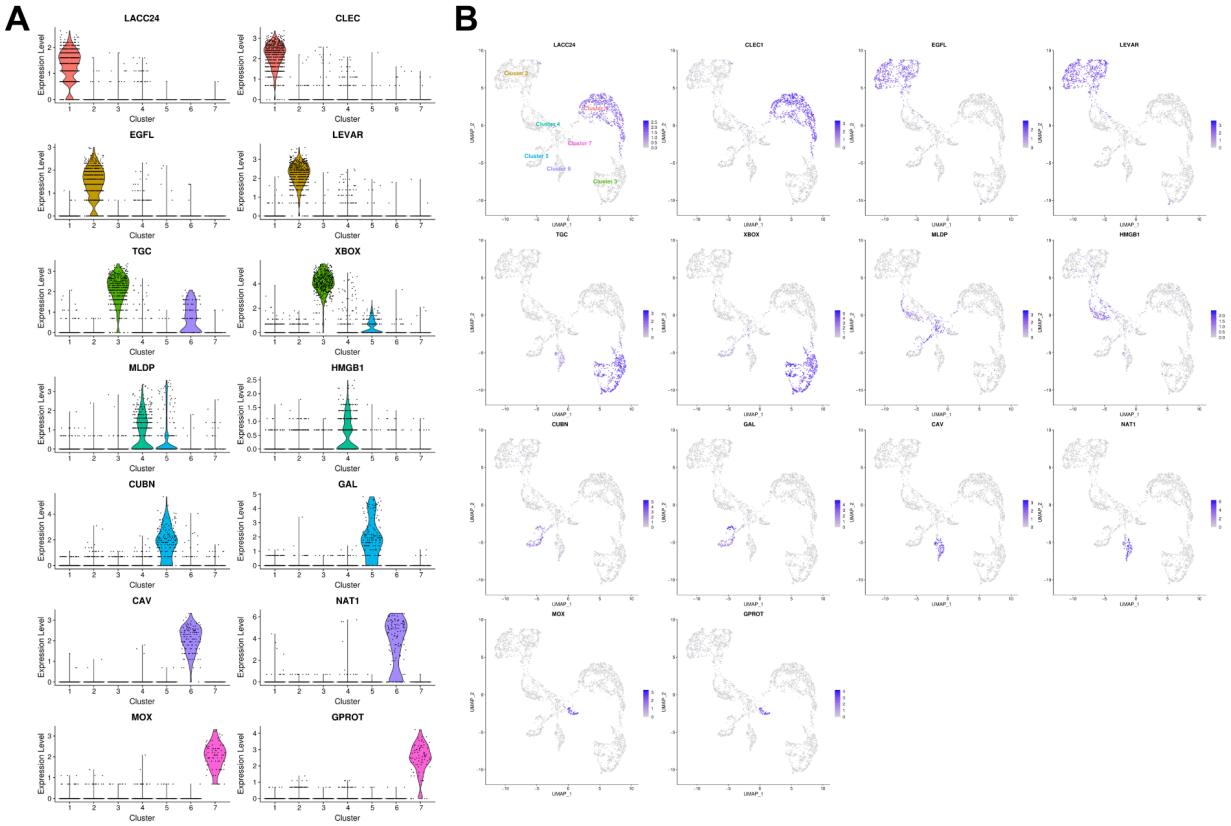

Figure S5. Cluster specificity and expression level of the 14 selected cluster markers A) Violin graph showing the average expression level (Log2FC) of the 14 selected marker transcripts specific to the different scRNA-seq clusters. **B)** Identification of cells expressing the selected markers on the UMAP plot. Positive cells are colored purple according to the Log2FC value. LACC24 and CLEC are specific of cluster 1, EGFL and LEVAR of cluster 2, TGC and XBOX of cluster 3, MLDP and HMGB1 of cluster 4, CUBN and GAL of cluster 5, CAV and NAT1 of cluster 6 and MOX and GPROT of cluster 7. **LACC24** : Laccase 24, **CLEC** : C-type lectin domain-containing protein, **EGFL** : EGF-like domain-containing protein 8, **LEVAR** : Putative regulator of levamisole receptor-1, **TGC** : TGc domain-containing protein, **XBOX** : X-box binding protein-like protein, **MLDP** : ML domain-containing protein, **HMGB1** : High mobility group protein B1, **CUBN** : Cubilin, **GAL** : Galectin, **CAV** : Caveolin, **NAT1** : Natterin-

1, **MOX** : DBH-like monooxygenase protein 1, **GPROT** : G protein receptor F1-2 domain-containing protein.

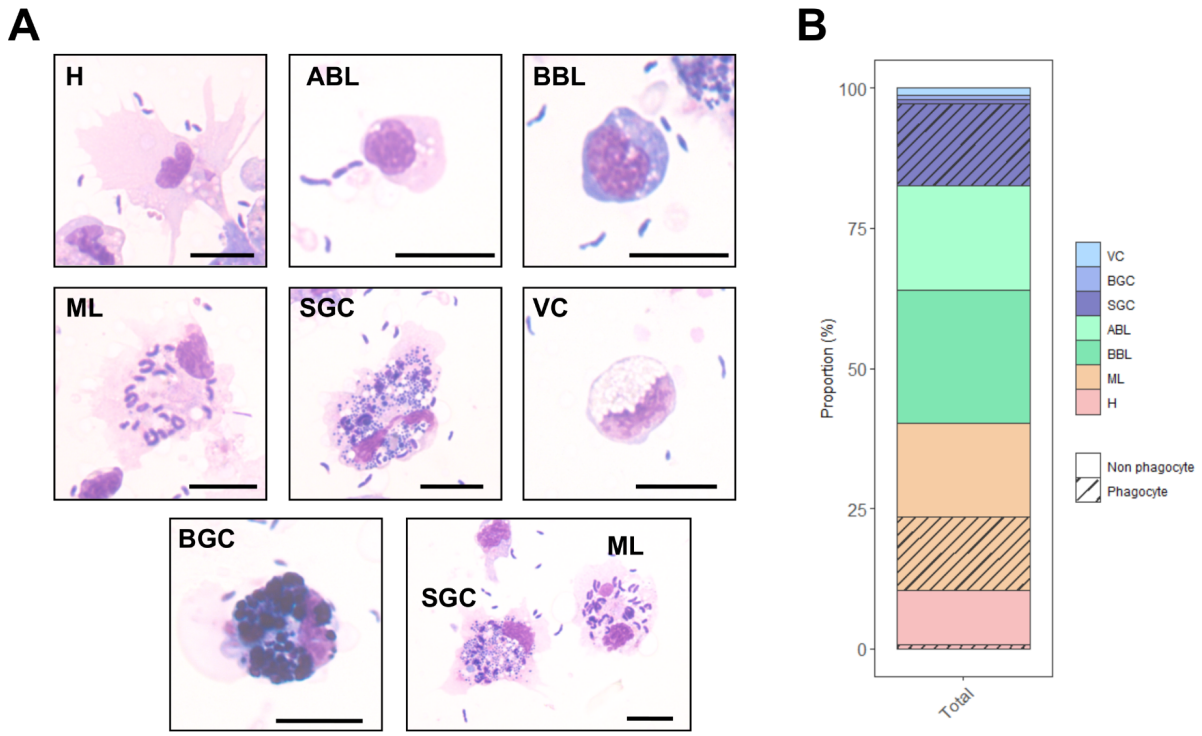

Figure S6. Measurement of the ability of *C.gigas* hemocytes to phagocytose *Vibrio tasmaniensis* LMG20012^{T}. Oyster hemocytes were challenged with non-pathogenic *Vibrio tasmaniensis* LMG20012^{T} and phagocytosis was measured by observing intracellular bacteria after MCDH staining. **(A)** MCDH staining of hemocytes after phagocytosis assay. Scale bar : 10µm. **(B)** Bar plot showing the proportion of each cell type and the proportion of phagocytic cells. **H** : Hyalinocytes, **ABL** : Acidophilic Blast-Like cells, **BBL** : Basophilic Blast-Like cells, **ML** : Macrophage-Like cells, **SGC** : Small Granule Cells, **VC** : Vesicular Cells and **BGC** : Big Granule Cells.

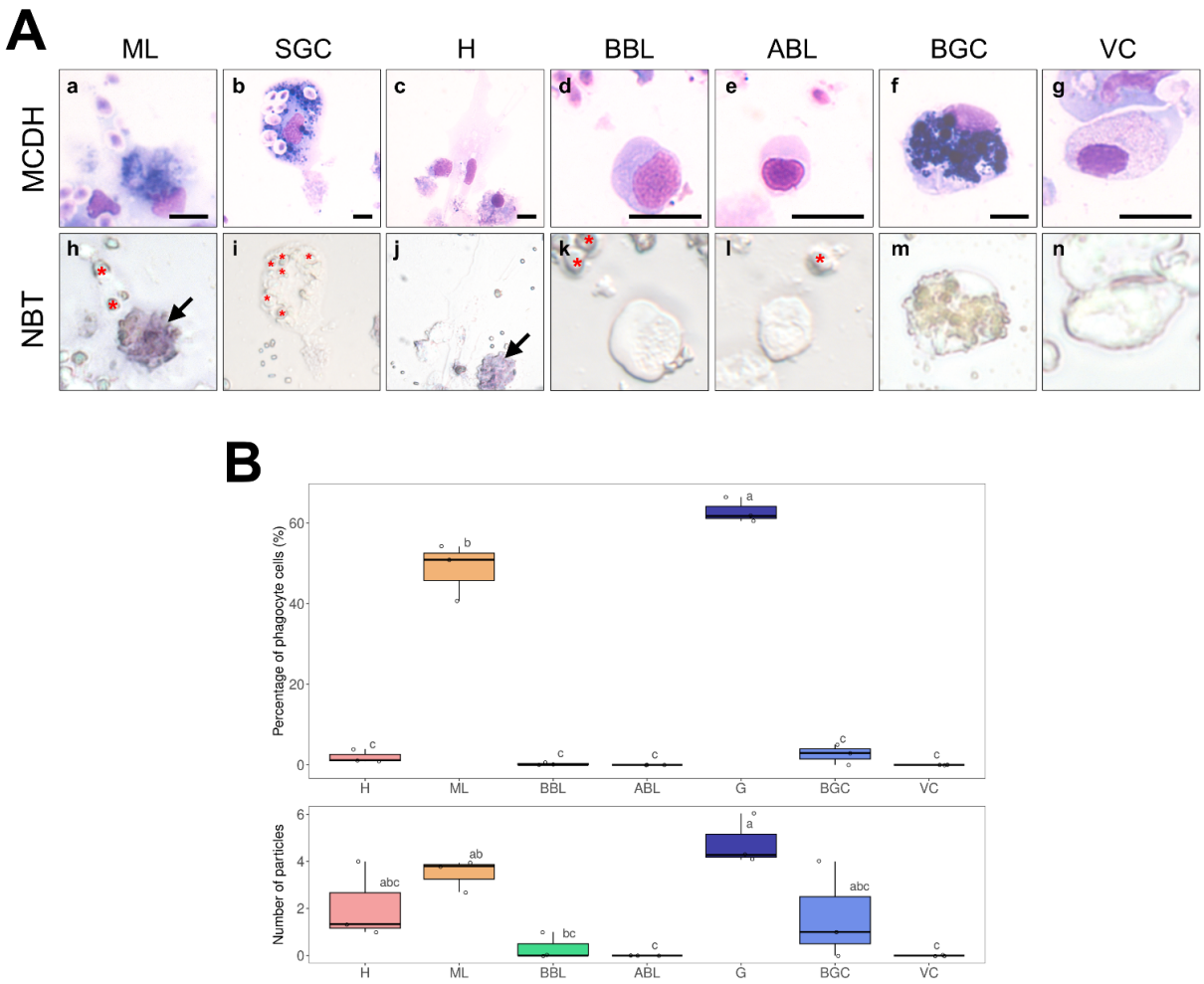

Figure S7. NBT (NitroBlueTetrazolium) staining of oyster hemolymph exposed to zymosan particles. (A) Hemocyte morphology after MCDH staining : Macrophage Like **(a)**, Small Granule Cells **(b)**, Hyalinocyte **(c)**, Basophilic **(d)** and Acidophilic **(e)** Blast cells, Big Granule Cells **(f)** and Vesicular Cells **(g)**. NBT staining of the different hemocyte types **(h-n)**. Red stars show zymosan and bacteria particles. Black arrows identify Macrophage-Like cells. Scale bar : 10 µm. **(B)** Quantification of the phagocytic activity of each cell type for zymosan particles from 3 independent experiments. Results of quantification of the phagocytic activity of each cell type and number of zymosan particles per cell type. The graph shows the result of 3 independent experiments.

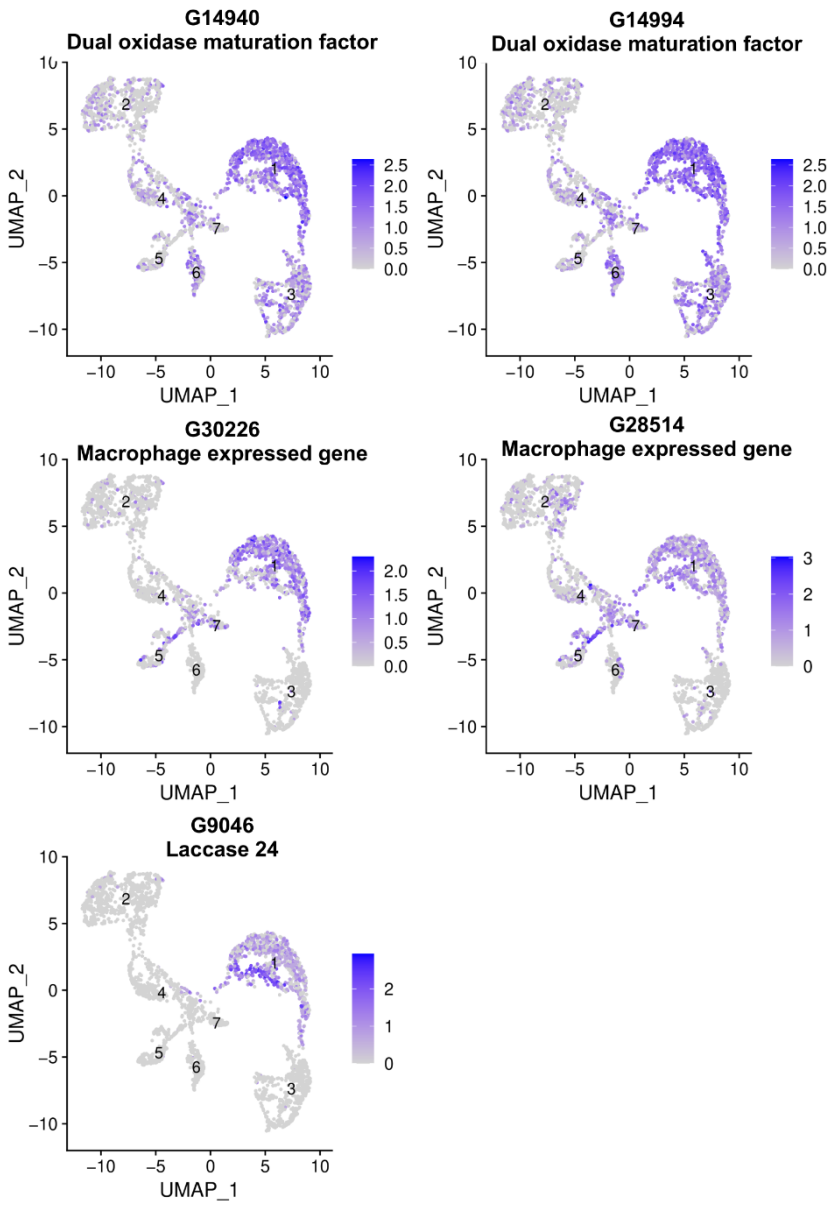

Figure S8. Uniform Manifold Approximation and Projection (UMAP) plots of cells expressing Macrophage-Like markers. Cluster numbers are indicated on each cluster. Each point in the UMAP plot represents a single hemocyte, and the clustering of these points reveals the distinct transcriptional profiles of macrophage-like specific markers within the hemocyte population.

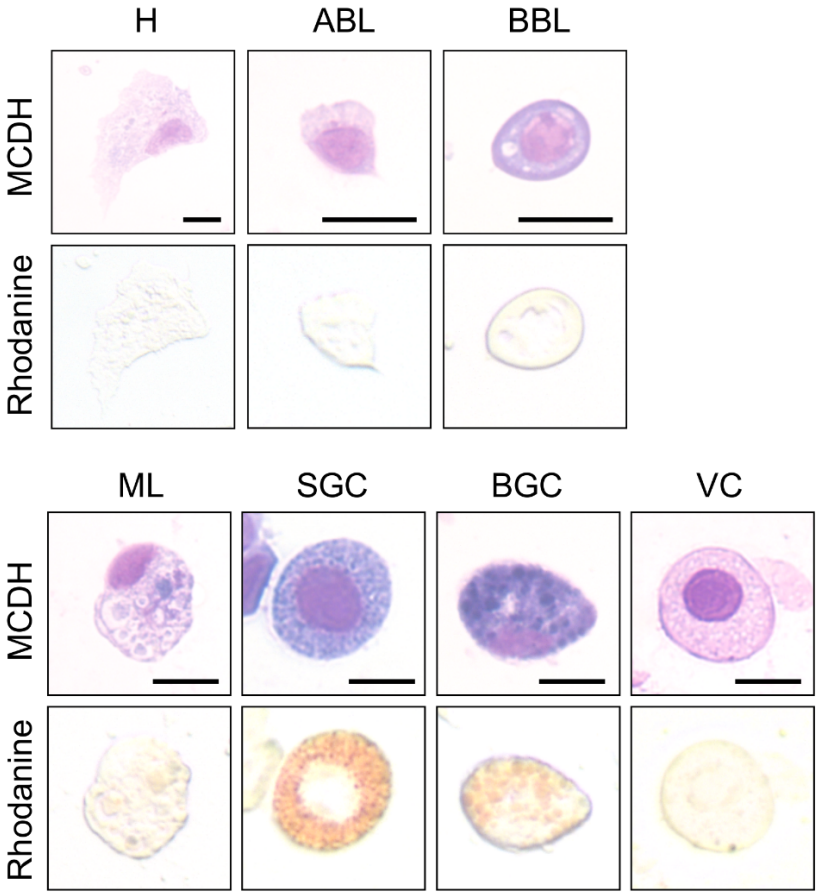

Figure S9. Labeling of intracellular copper stores in C.gigas hemocytes. MCDH (upper panels) and rhodanine (lower panels) staining of oyster hemocytes to reveal copper accumulation. Cells were first processed for copper staining and then stained according to MCDH protocol. **H** : Hyalinocytes, **ABL** : Acidophilic Blast-Like cells, **BBL** : Basophilic Blast-Like cells, **ML** : Macrophage-Like cells, **SGC** : Small Granule Cells, **VC** : Vesicular Cells and **BGC** : Big Granule Cells. Bar : 10µm.

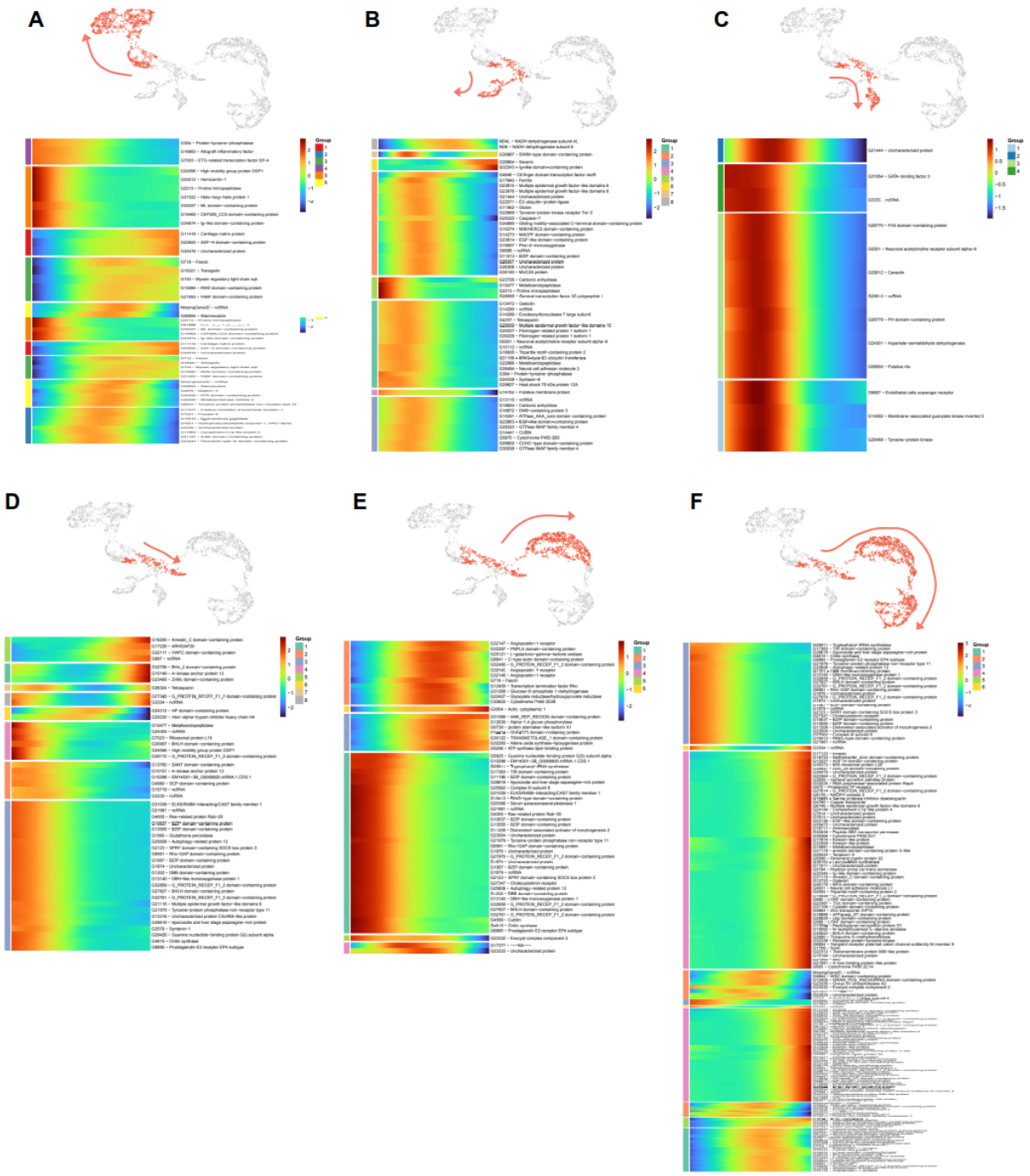

Figure S10. Results of scRNA-seq trajectory analysis using Monocle3. Analysis was performed using cluster 4 as the zero pseudotime. **(A)** Lineage from immature cells to hyalinocytes, **(B)** to cluster 5 cells, **(C)** to cluster 6 cells, **(D)** to vesicular cells, **(E)** to macrophage-like cells and **(F)** to small granule cells. For each lineage, cell trajectories are shown

in red and heat maps of pseudo time-dependent genes are shown. Blue indicates low expression, and red indicates high expression. Pseudotime flows from right to left.

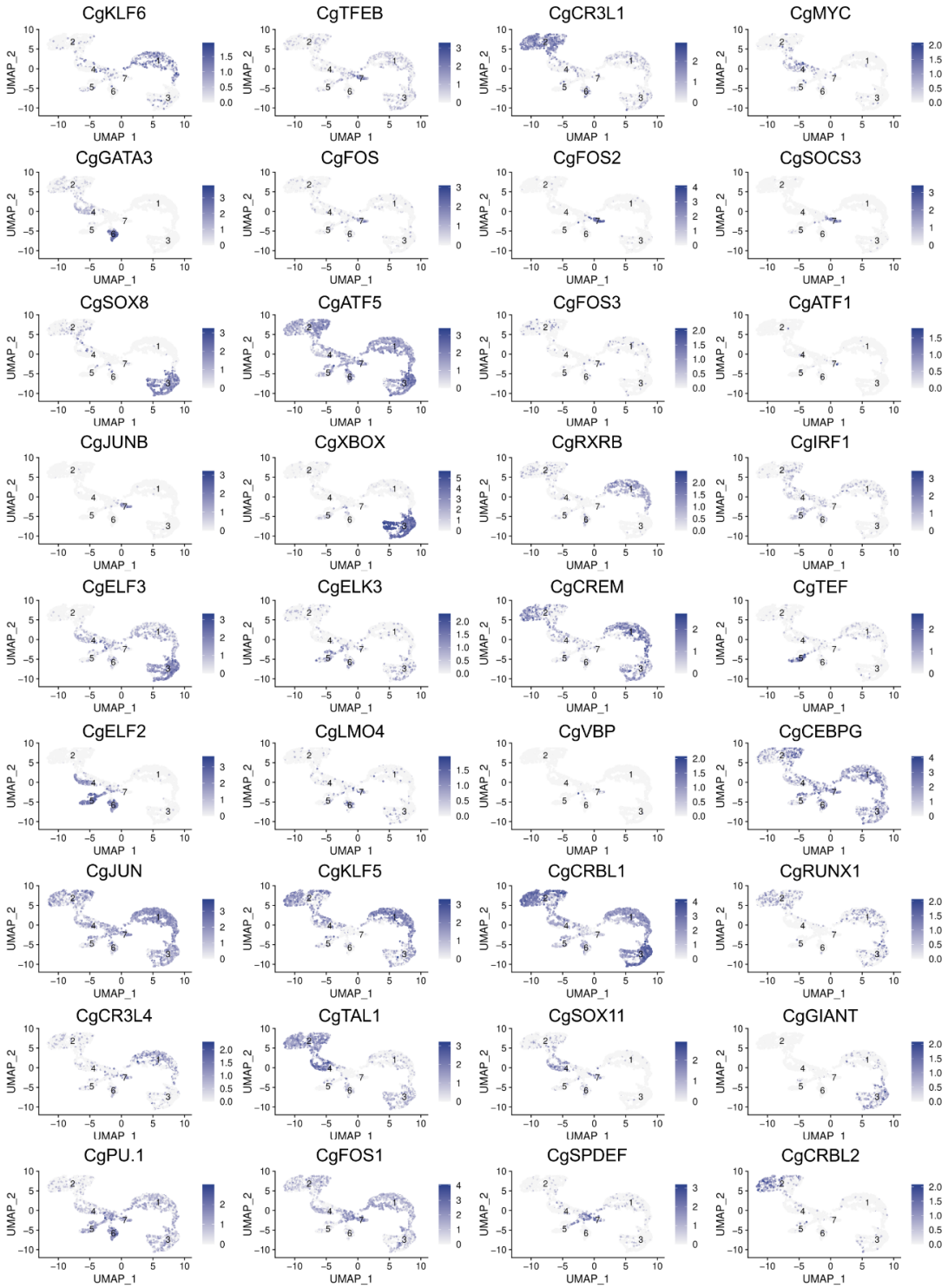

Figure S11. Uniform Manifold Approximation and Projection (UMAP) plots of cells expressing transcription factors. 28 UMAP representation for the transcription factors

identified in the scRNA-seq dataset. Each UMAP plot shows cells expressing the transcription factor in purple. Log2FC expression level is also reported.

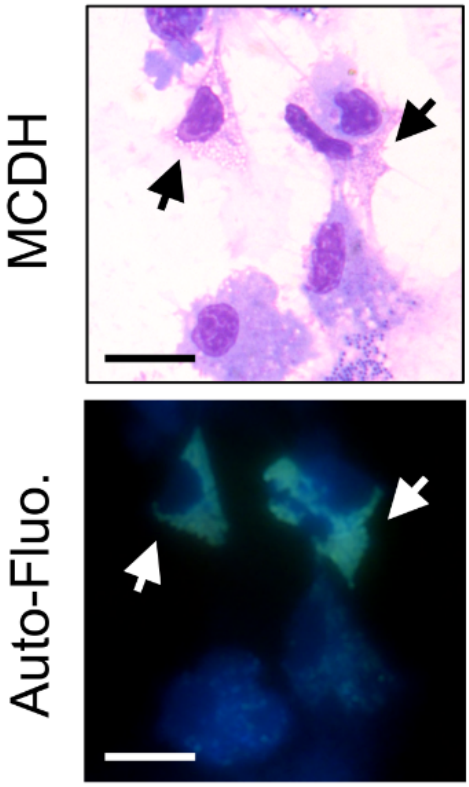

Figure S12. Observation of autofluorescence of vesicular cells in hemolymph. Freshly punctured total hemolymph was cytospun, directly observed under a microscope using a DAPI filter set (DAPI Blue ex : 350/50 nm, DC : 400 nm and em : 460/50 nm) and then processed for MCDH staining. Arrows indicate autofluorescent cells. Scale bar : 10 µm